U.S. copyright law (title 17 of U.S. code) governs the reproduction and redistribution of copyrighted material.

Ariel Transmission Coversheet

www.infotrieve.com/ariel

The Lifetime of the D^0 Meson

by

Ian Alexander Lovatt

A Thesis submitted in conformity with the requirements
for the Degree of Doctor of Philosophy in the
University of Toronto

© Ian Alexander Lovatt
1986

Abstract

In a hybrid emulsion spectrometer exposed to a wide–band neutrino beam at Fermi National Accelerator Laboratory, 2638 neutrino and anti–neutrino events were located in the second of two data samples. Thirty–nine events were consistent with a D^0 hypothesis. The mean lifetime was $(4.8^{+0.9}_{-0.7}) \times 10^{-13}$ s.

Original Material

As is common in modern experiments in High–Energy Physics, in E531 many people performed many jobs. I have participated in several phases of this project.

I helped to build the CPI in Toronto, and was part of a small group which tested the device in a muon beam at Fermilab. Before and after this, I extensively tested the CPI with an artificial source. At McGill University, I helped to analyze the results of these tests.

Before the second run of E531, I took an active part in preparing the spectrometer for the acquisition of data. During the six and a half months of running, I helped to collect the data, and to monitor and maintain the apparatus.

With the data safely recorded on tape, in Toronto I reconstructed the neutral events with an interactive track–fitting programme. I also modified an existing kinematic fitting programme. My analysis of the neutral decays, often performed in parallel with collaborators at The Ohio State University, is described in sections 4.2 through 4.5.

Ackowledgements

Now that this nearly Sisyphean task is drawing to an end, I wish to express my gratitude to the many people who have contributed to my education.

I am indebted to my fellow graduate students at the University of Toronto for their encouragement, their moral support and their advice. Those who gleefully vetted early versions of this thesis have my grudging thanks.

Modern experiments in High–Energy Physics are performed by increasingly large groups of people. To all the members of E531, whose names are listed in Appendix 1, I am grateful for help and knowledge and patience.

While working on E531, I spent 63 weeks at Fermilab and a year at McGill University. I am grateful to the friends I made at both institutions for making life enjoyable and for their contributions to whatever success I have had.

The Charged Particle Identifier, latterly known as the Canadian Propane Inferno, was assembled at the University of Toronto. My thanks go to all who built it, and especially to Roo Borson and Anthony Kiang.

The job of analysing the data amassed by this experiment was aided by many people. I wish to thank explicitly Brian Stacey, who always had time to help, and Anna Pezacki, who played Paian to the occaisionally ungodlike Atlas, Hermes and Apollo.

Many of the illustrations in this thesis were crafted by Mitchel Kovarik. For his celerity and for his dexterity, I am grateful.

Jim Prentice has been my supervisor for these seven long years. I wish to thank him, for he has supported me and prodded me and borne with a smile my

often palpable cynicism.

Finally, for all they have done, I offer my deepest thanks to my parents, whose first–born is finally leaving school.

Table of Contents

	Page
Abstract	i
Original Material	ii
Acknowledgements	iii
Table of Contents	v
List of Figures	vii
1. Introduction	1
2. Theory	7
2.1 Quarks	7
2.2 Colour	10
2.3 Weak Interactions	14
2.4 Decays	22
3. The Experiment	28
3.1 The Neutrino Beam	28
3.2 The Emulsion Target	31
3.3 The Time–of–Flight System	35
3.4 The Trigger	37
3.5 The Drift Chambers	38
3.6 The Charged Particle Identifier	41
3.7 The Electromagnetic Shower Detector	42
3.8 The Hadronic Calorimeter	45
3.9 The Muon Counters	48
4. Analysis	49
4.1 Scanning	50
4.2 Event Reconstruction	57

4.3 Kinematic Analysis 63

4.4 Lifetime Calculation 64

4.5 Discussion 66

4.6 Conclusion 80

Figures F–1

Appendix 1

Appendix 2

Appendix 3

References

List of Figures

		Page
1.1.	$K_L \longrightarrow \mu^+\mu^-$	F–1
1.2.	$K_L \longrightarrow \mu^+\mu^-$	F–1
1.3.	$K_L \longrightarrow \mu^+\mu^-$	F–2
2.1.	Meson And Baryon SU(3) Octets	F–3
2.2.	Meson And Baryon SU(4) Multiplets	F–3a
2.3a.	$e^+\bar{e}^- \longrightarrow \mu^+\mu^-$	F–4
2.3b.	$e^+e^- \longrightarrow$hadrons	F–4
2.4.	R *vs.* W	F–5
2.5.	Second Term in the S–Matrix	F–6
2.6.	Third Term in the S–Matrix	F–6
2.7.	Muon Decay	F–7
2.8.	Decay of a Charmed Quark	F–8
2.8a.	Decay of a Charmed Quark	F–9
2.9.	$F^+ \longrightarrow \tau^+\nu_\tau$	F–9
2.10.	Tau Decay	F–10
2.11.	The 'Penguin' Mechanism	F–11
2.12.	Pion Decay	F–11
3.1.	The Neutrino Beam Line	F–12
3.2.	The Neutrino Momentum Spectrum	F–12
3.3.	The Emulsion Target – Looking Upstream	F–13
3.4.	The Emulsion – Cut–away View	F–13
3.5.	Ionization *vs.* $P\beta$ in Emulsion	F–14
3.6.	Time–of–Flight I	F–15
3.7.	Time–of–Flight II	F–15

3.8.	Upstream Drift Chambers	F–16
3.9.	Tracks in the Magnetic Spectrometer	F–16
3.10.	The Charged Particle Identifier – Side View	F–17
3.11.	Proportional Cells of the CPI	F–17
3.12.	Lead Glass Array	F–18
3.13.	Pion Energy Loss Spectrum in Lead Glass	F–18a
3.14.	The E531 Spectrometer – Side View	F–19
3.15.	Muon Energy Loss Spectrum in the Calorimeter	F–20
3.16.	Masses Determined by Time–of–Flight	F–21
4.1.	Conversion Finding Efficiency	F–22
4.2.	Vertex Finding Efficiency	F–22
4.3a.	DC Slopes – Exit Slopes; dxdz	F–23
4.3b.	DC Slopes – Exit Slopes; dydz	F–23
4.3c.	DC Slopes – Decay Slopes; dxdz	F–24
4.3d.	DC Slopes – Decay Slopes; dydz	F–24
4.3e.	Exit Slopes – Decay Slopes; dxdz	F–25
4.3f.	Exit Slopes – Decay Slopes; dydz	F–25
4.4.	A Triple Coincidence in the EPIC Wires	F–26
4.5.	EPIC Wire Separations	F–27
4.6.	Two Spatially Separated Showers	F–27
4.7a.	Decay Rate *vs.* Time	F–28
4.7b.	Maximum Likelihood *vs.* Mean Decay Time	F–28
4.8.	Baryon Mass Ideogram	F–29
4.9.	A 0–C Solution	F–29
4.10a.	$D^0\pi^+, D^0$Mass Difference	F–30
4.10b.	$D^0\pi^+, D^0$ – Mixed Events	F–30
4.10c.	P_t of π^+relative to D^0	F–31

4.10d. P_t Distribution of Mixed Events F–31

4.11a. $D^0\gamma, D^0$ Mass Difference F–32

4.11b. $D^0\gamma, D^0$ less Background F–32

4.12. D^0 Mass Ideogram F–33

4.13. D^0 Lifetimes of Other Experiments F–33a

Introduction

To understand the nature of matter has long been the elusive goal of physics. One of the techniques used in the pursuit of this goal has been the study of the decays of sub–atomic particles. This has proved to be a fruitful approach, guiding the development of a theory of matter by suggesting the existence of new particles and new types of forces, by providing new insights into other areas of physics, and by revealing new properties of matter.

The first such new property revealed by the study of decays was the very fact that matter decayed. Becquerel[1] chanced upon the phenomenon of radioactivity in 1896. Seven years later, Rutherford and Soddy[2,3] had shown that radioactivity involved the metamorphosis of one element into another, accompanied by the emission of one of two types of radiation: β rays, which were just Thomson's electrons; and α rays, later identified as ionized helium atoms. Rutherford[4] later guessed that a third type of radiation associated with decays, γ radiation, which did not involve any change of element, was just emission of pulses of electromagnetic radiation, similar to X–rays.

Out of Rutherford's research emerged another new property of matter, the half–life[5], $t_{\frac{1}{2}}$. This is the time taken for a sample of an unstable species to decay to one half of its original size. It is generally affected by neither environment nor history[6], and it is unique to the decaying species. This is characteristic of a substance which decays at a rate proportional only to the size of the sample:

$$\frac{dn(t)}{dt} = -\frac{1}{\tau}n(t) \ . \tag{1.1}$$

The mean lifetime, τ, is the average decay time, and is equal to 1.44 $t_{\frac{1}{2}}$.

The results of the studies of decays can have implications that reach far beyond such specific details, into other areas of physics. For instance, another facet

of radioactivity uncovered by Rutherford and Soddy[7] was that the energy released in a decay was a much larger fraction of the unstable particle's mass than was released in chemical reactions. Seeing no evidence that the radioactive elements differed from their non–radioative isotopes in their chemical properties, Rutherford and Soddy concluded that "there is no reason to assume that this enormous store of energy is possessed by the radio elements alone." And they went on to suggest a solution to the puzzle of the source of stellar energy: "The maintenance of solar energy ... no longer represents any fundamental difficulty if the internal energy of the component elements is considered to be available, *i.e.*, if the processes of subatomic change are going on."

Consequences for other areas of physics, more profound than just a new entry in the Particle Data Handbook, are promised by further examinations of β–decays. These reactions involve the emission of electrons and very light, if not massless, neutrinos. If the neutrino is found to have a mass, and recent tritium decay experiments suggest that this is so[8], then the mass of the neutrinos created in the Big Bang may suffice to hold together the Universe itself.

β decay is just one of many types of interactions between particles. All are governed by four forces: gravity, electromagnetism, the weak force and the strong force. That there is a weak force at all was first revealed by the discovery of β decay. This force is responsible for both tritium decay and for the decay of the charmed particle D^0, to be discussed in this thesis.

There is a suggestion of still another force, a milli–weak force. This hint comes from experiments concerning the decays of the two neutral K mesons, K^0 and $\overline{K^0}$. Both K's can decay to two pions

$$K^\circ(\overline{K^\circ}) \rightarrow \pi^+\pi^- \ .$$

Consequently, there is an amplitude for the K° to change into a $\overline{K^\circ}$, and *vice versa.*

$$K^\circ \iff \overline{K^\circ}$$

The kaons form a quantum–mechanical two–state system, which can be described by specifying the amplitudes for the state to be either K° or $\overline{K^\circ}$. This system can equally well be described by the amplitudes to be any two orthogonal superpositions of K° and $\overline{K^\circ}$. One such pair comprises the combinations that have eigenvalues of CP equal to ± 1. CP is the combined operation of charge–conjugation, C, and parity–reversal P. C turns the wave–function of a particle into the that of its anti–particle and P changes the coordinates of the wave–function from $\vec{r}$ to $-\vec{r}$. Particles themselves have intrinsic parity quantum numbers, which take the values ± 1. The K's have negative parity.

If CP is a conserved quantity, and if the state's CP is 1, then it can decay to two pions, a state that also has $CP = +1$. The other combination ($CP = -1$) can decay to three pions, but since the phase space available for three pions is much smaller than for two, the lifetime of the odd state is much greater than that of its even partner. When a K^0 is produced, for instance in the reaction

$$\pi^- p \longrightarrow K^0 \Lambda^0 \ ,$$

it has equal amplitudes to have $CP = \pm 1$. As time passes, the amplitude for the state to have even CP decreases exponentially, while the amplitude to have odd CP, with its much larger decay time, changes very little. After many lifetimes, the state is overwhelmingly more likely to have odd CP. Yet, in 1964, Christenson, Cronin, Fitch and Turlay[9] observed the long-lived state decay to two pions, albeit rarely, but more frequently than was consistent with CP conservation.

This means that there is a term in the total Hamiltonian, $\mathcal{H}$, which does not commute with CP, so that eigenstates of CP are not eigenstates of $\mathcal{H}$, and that $\mathcal{H}$ permits transitions between states with different CP. The neutral kaon system remains the only one to exhibit CP violation. Further examination of weakly decaying hadrons may answer the question of whether or not the non-conservation of CP can be accommodated by the theory of the weak interaction. If it cannot, then the phenomenon is the harbinger of a new, fundamental force.

In some cases, the study of a decay has led to the prediction that new particles existed. For example, by 1914, Chadwick[10] had shown that the electrons from β–decay emerged not with a unique energy, but with energies that varied continuously from decay to decay. In 1927, Ellis and Wooster[11] measured the amount of heat released as a sample of ^{210}Bi decayed. They found that the energy produced per nucleus was equal to the average energy of the β rays, and not to the maximum energy. From this, Pauli[12] deduced that the energy released in the decay was shared by the electron and a very weakly interacting new particle – the neutrino.

Another type of particle predicted to exist at least partly on the basis of the study of decays is the charmed particle. In fact, there were many charmed particles predicted to exist, some of which have subsequently been discovered. The reaction that sparked the the prediction of charm was

$$K_L^0 \longrightarrow \mu^+\mu^- \ .$$

The rate calculated for this reaction, in the theory of three quarks (u, d and s) and two charged weak bosons (W^+ and W^-) in vogue at the time, was much larger than the experimentally observed rate. This discord was due to the fact that the prediction involved a divergent integral over all possible, unconstrained,

momenta of the W's in the intermediate loop (fig.1.1). The mechanism proposed[13] to avoid this discrepancy consisted of two pieces. The first introduced a neutral vector boson, the Z^0, which interacted with quarks of the same type (flavour) (fig. 1.2). The second piece involved a new quark, the charmed quark, which interacted weakly with the weak bosons and the other quarks. These two hypothetical particles provided new channels for $K_L^0 \rightarrow \mu^+\mu^-$ (fig. 1.3). The amplitudes for these indistinguishable reactions are assumed to combine coherently to suppress the decay rate.

The existence of a new flavour of quark led to the prediction of a spectrum of bound states, the charmed hadrons. Their lifetimes and branching ratios were estimated by Gaillard, Lee and Rosner[14]. The first new particle to be interpreted as direct evidence for the existence of charm was the J/ψ, discovered in 1974[15]. It is a bound state of a c and a $\bar{c}$ quark. Particles with open charm, that is, particles composed of a c quark and a quark of another flavour, were soon discovered in e^+e^- experiments[16].

The lifetimes of the charmed particles were estimated to be approximately 10^{-13} to 10^{-12}s. The apparatus needed to observe such short decays must have excellent spatial resolution. At the inception of the experiment whose results are the subject of this thesis, the only techniques available with resolution fine enough used bubble chambers and nuclear emulsions[17], and even bubble chambers could only resolve some of the decays.

Experiments which attempted to measure charmed particle lifetimes using conventional bubble chambers relied on seeing the distinctive decays of neutral strange particles that often come from charm decays; the charged strange particles are not easily identified. Moreover, there are relatively many strange particles originating from sources other than charm decays.

In principle, all charmed particles that decay to charged secondaries within an emulsion target may be seen. However, early emulsion experiments[18] lacked a satisfactory strategy for identifying the decay products and measuring their momenta. Without this information, neither the invariant mass nor the momentum of the parent could be calculated, and without the mass, the parent could not be identified. Since its proper decay time (τ) is related to its momentum (P) and its mass (m) by equation 1.2,

$$\tau = \frac{t_{Lab}}{\gamma} = \frac{L}{\beta\gamma c} = \frac{mL}{Pc}, \tag{1.2}$$

where L is the observed decay distance, the proper time could not be calculated.

This experiment[19] combined the attractive features of an emulsion target with the advantages of an electronic detector. The target afforded fine spatial resolution and a visible record, with very little background, of almost all types of charm decay. With the spectometer, interaction and decay vertices in the emulsion were located efficiently, and the secondary particles were identified and their momenta were measured. This experiment was thus able to find, reconstruct and identify short–lived particles with lifetimes between 10^{-15} and 10^{-11}s.

Chapter 2

Theory

Charm decay is not a simple phenomenon. The data collected to date show that the most elementary model of the process fails to explain it. For instance, contrary to simple predictions, the lifetimes of the lightest charmed hadrons are not the same. On the other hand, there is reason to believe that an understanding of charm decay may soon be at hand, as the union of the quark model and the Weinberg–Salam model of weak interactions adequately describes simpler processes related to charm decay. This chapter discusses features of these models which bear on the decay of the D^0. For example, an important charm–decay mechanism is 'free quark decay'; an analogous mechanism plays the dominant role in muon decay, a process that is well understood. 'Free fermion decay' and the 'colour' degree of freedom suffice to explain τ decay, a process more closely resembling charm decay. The mechanism of 'helicity supression', which explains why pions decay to muons more often than they decay to electrons, also explains why the leptonic decays of charmed mesons should be rare. Finally, consideration of the exchange and annihilation mechanisms, quantum interference and quantum chromodynamics (QCD), the theory of the strong interaction, may explain why the lifetimes of the charmed hadrons differ.

Quarks

In the subatomic zoo, the D^0 meson is a member of a species known as charmed hadrons. It, and its congeners (*e.g.* $D^{\pm}$, $F^{\pm}$, Λ_c^+), are distinguished from other hadrons by their masses (1865 $\rightarrow$ 2100 MeV/c^2) and lifetimes ($10^{-13} \rightarrow 10^{-12}$s)[20]. There are other families of particles with similar masses but they decay much more readily ($\sim 10^{-23}$s). Hadrons, as a group, differ from leptons in that the latter do not interact strongly. For example, although the τ lepton's

lifetime (3.5×10^{-13}s) is similar to that of the charmed particles, and although it has a comparable mass (1784 MeV/c^2)[20], so that it superficially resembles a charmed hadron, it is unaffected by the strong force, since it apparently does not decay to exclusively hadronic final states. Hadrons can be further distinguished from leptons since the leptons appear to be point-like, whereas hadronic radii are approximately 1 fm.

Compelling evidence suggests that hadrons are composed of quarks. One example of such evidence is provided by the deep inelastic scattering of electrons by protons. When the electron is scattered into a solid angle Ω with an energy E_f, the double–differential inclusive cross–section is related to the cross–section describing the scattering of electrons by point–like, 'spin–$\frac{1}{2}$' targets, (Mott scattering) by equation 2.1,

$$\frac{d^2\sigma}{d\Omega dE_f}/(\frac{d\sigma}{dE_f}) = F(q^2) \ , \tag{2.1}$$

where q^2 is the four–momentum lost by the electron. The 'form–factor' $F(q^2)$ is the Fourier transform of the charge distribution of the scattering centres. Briedenbach *et al.*[21] showed that, up to $|q|^2 \sim 6$ GeV/c^2, the ratio is approximately constant. A constant form–factor indicates that the scatterers are point–like. Hence, the same sort of evidence that Rutherford used to deduce the structure of the atom[22] also leads to the conclusion that hadrons are made of quarks.

The large number of hadrons also suggests that they are not fundamental. That there should be so many elementary particles is, if nothing else, aesthetically unsatisfying.

More evidence of the structure of hadrons can be seen in the patterns they form. Before the discovery of charmed particles, it had been noted that hadrons could be separated into groups characterized by the quantum numbers of spin (J),

parity (P), charge conjugation (C) and baryon number (B). For instance, there are eight particles with $J^{PC} = \frac{1}{2}^{++}$ and $B = 1$ (p, n, Σ^+, Σ^-, Σ^0, Ξ^-, Ξ^0, Λ^0). Another example is the group of eight mesons with $J^{PC} = 0^{-+}$ and $B = 0$: $\pi^\pm$, π^0, $K^\pm$, $\overline{K^0}$, K^0, η. A striking pattern is formed when the distribution of hadrons within a group is plotted on a graph whose axes represent isospin (I) and strangeness (s) (fig 2.1). The numbers of hadrons in these groups are also the numbers of basis states associated with the simplest representations of the Lie group SU(3). There is no hadronic group with only three members, the dimension of the fundamental representation. Gell–Mann and Zweig[23] postulated that the basis states of the fundamental representation of SU(3) were three new particles, the quarks. They were named 'up', down' and 'strange', u, d and s. The members of the hadronic multiplets could then be regarded as basis vectors for direct–product representations of SU(3). For example, the direct product of three fundamental representations can be expressed as

$$3 \otimes 3 \otimes 3 = 10 \oplus 8 \oplus 8 \oplus 1. \tag{2.2}$$

The result is a reducible representation composed of four irreducible representations with dimensions ten, eight, eight and one respectively. There are baryon groups corresponding to each representation. The patterns formed by the mesons are mirrored by the direct product of a fundamental representation and its conjugate.

$$3 \otimes \overline{3} = 8 \oplus 1 \tag{2.3}$$

This is a direct sum of the eight– and one–dimensional representations of SU(3), corresponding to the octets and singlets of mesons.

Since there are no hadron patterns corresponding to any direct products other than the two mentioned above, it was concluded that there are three quarks in

a baryon and a quark and an anti–quark in a meson. Several properties of the quarks may be deduced from this. For instance, the baryon number of a quark is $\frac{1}{3}$, $-\frac{1}{3}$ for an anti–quark. The quarks must be fermions with 'spin–$\frac{1}{2}$', so that they can form fermionic baryons and bosonic mesons. Lastly, the quarks have electric charges that are multiples of $\frac{1}{3}e$, where e is the charge of an proton.

$$\begin{aligned} q(u) &= \frac{2}{3}e \\ q(d) &= -\frac{1}{3}e \\ q(s) &= -\frac{1}{3}e \end{aligned} \tag{2.4}$$

The model has been extended to include charmed particles. Distributions of hadrons are plotted on three–dimensional spaces, whose axes are I, s and charm (c) (fig. 2.2). Manifestations of a fifth quark have been discovered (b)[24], and theoretical predjudice and some experimental evidence suggest the existence of a sixth (t)[25]. The additional quarks have properties similar to those of the first three. In particular,

$$\begin{aligned} q(c) &= \frac{2}{3}e \\ q(b) &= -\frac{1}{3}e \\ q(t) &= \frac{2}{3}e\ . \end{aligned} \tag{2.5}$$

Colour

High–energy physicists have given quarks the additional property of colour[26]. This concept was invented to resolve the apparent inconsistency between the nascent quark model and the quantum–statistical nature of the Δ^{++}. To do this, each quark was allowed to have one of three colours (r, b and g). Within a hadron, the colours must be distributed so that the composite particle has no net colour. Were this not the case, each hadron would have several duplicates,

testifying to the extra degree of freedom of the component quarks. Expressed in the language of group theory, hadrons are 'colour–singlet' combinations of quarks.

The interactions of the quarks are independent of the 'values' of the colours involved. Mathematically, the Lagrangian describing the quarks is locally invariant under the operations which change quark colours. From this it follows that there are 'gauge bosons' (gluons), which transform according to the adjoint representation of a Lie group, and that the gluons interact with the quarks[27]. The choice of three colours (evidence for which is discussed later in this section) suggests that the group is SU(3). (This is an application of the group SU(3) entirely different from that mentioned earlier.) Since the simplest adjoint representation of SU(3) is eight–dimensional, the model of coloured quarks has eight gauge bosons, the gluons. Data from νN scattering experiments indicates that roughly half of a nucleon's momentum is carried by something other than quarks[28] – presumably the gluons.

The presence of vector gluons in a hadron affects the angular–momentum configurations of the quarks in the hadron. The decay rates and branching ratios depend on these configurations, so that an understanding of the decay process must take into account the gluons. Since the quarks and gluons interact, gluons can dynamically affect decay rates and branching ratios, not only of hadrons, but also of leptons massive enough to decay into final states with hadrons.

It can be seen that there are three colour degrees of freedom by considering e^+e^- annihilation (fig. 2.3) and specifically the the ratio R (eq. 2.6).

$$R = \frac{\sigma(e^+e^- \rightarrow hadrons)}{\sigma(e^+e^- \rightarrow \mu^+\mu^-)} \tag{2.6}$$

The hadronic reaction can be viewed in two stages

$$e^+e^- \longrightarrow q\overline{q} \tag{2.7}$$

and

$$q\bar{q} \longrightarrow hadrons \ . \tag{2.8}$$

The amplitude for the latter is unity, since free quarks apparently do not exist, so that some hadrons must always be formed. Reaction (2.7) is formally identical to the production of $\mu^+\mu^-$.

If the centre–of–momentum energy is far from any bound–state masses, the dominant mechanism is the exchange of a single photon in the 's' channel (fig. 2.3), and the ratio R should be independent of the dynamic details of the reaction. For such a process, the amplitude is proportional to the charges of the two types of fermions involved;

$$A \propto e_f e_i \ , \tag{2.9}$$

where e_f is the charge of the final fermion pair, and e_i is the charge of the initial pair.

If quarks had no colour, the ratio would be simply

$$\begin{aligned} R &= \sum_q |e_q e_e|^2 / |e_\mu e_e|^2 \\ &= \sum_q e_q^2 \ , \end{aligned} \tag{2.10}$$

where $e_q(e_e)$ is the charge of the quark q (electron e). The sum extends over all quark pairs whose lightest bound state accessible through this reaction has a mass less than the centre–of–momentum energy. For instance, at energies between the Υ mass ($b\bar{b}$) and the mass of the $t\bar{t}$ combination, the sum extends over five flavours (u, d, s, c and b), and the result is $\frac{11}{9}$.

In a world with coloured quarks, the derivation of R is more subtle. Since the photon has no colour, the emerging quarks form a colour–singlet. The amplitude

for a quark pair to appear with flavour q and colour c is

$$A_{c,q} = \langle singlet|c\bar{c}\rangle\langle c\bar{c}|\gamma^*\rangle A_0 e_q \ . \tag{2.11}$$

The virtual photon state is represented by $|\gamma^*\rangle$, and A_0 contains the dynamic details of the reaction. Colour is an indistinguishable degree of freedom, so the rate must be calculated coherently.

$$\begin{aligned} A_q &= \sum_{colour} A_{c,q} \\ &= \sum_{colour} \langle singlet|c\bar{c}\rangle\langle c\bar{c}|\gamma^*\rangle A_0 e_q \\ &= A_0 e_q \sum_{colour} \langle singlet|c\bar{c}\rangle \\ &= N_c A_0 e_q \langle singlet|c\bar{c}\rangle \end{aligned} \tag{2.12}$$

The amplitude for the γ^* to materialize as a pair of quarks with colours c and $\bar{c}$ has been absorbed into A_0, which is the same for all colours. The number of colours is N_c.

Within the context of SU(3), the colour–singlet wave function for a quark and an anti–quark is

$$\begin{aligned} \langle singlet| &= \sqrt{\frac{1}{3}}\langle r\bar{r} + g\bar{g} + b\bar{b}| \\ \therefore \langle singlet|r\bar{r}\rangle &= \sqrt{\frac{1}{3}} = \sqrt{\frac{1}{N_c}} \ . \end{aligned} \tag{2.13}$$

Consequently, the total rate is

$$\begin{aligned} \Gamma_{tot} &= \sum_q |A_q|^2 \\ &= \sum_q |N_c\sqrt{\frac{1}{N_c}} A_0 e_q|^2 \\ &= N_c |A_0|^2 \sum_q e_q^2 \ . \end{aligned} \tag{2.14}$$

If five flavours are involved, then

$$\begin{aligned} R &= N_c \sum_{u,d,s,c,b} e_q^2 \\ &= \frac{11}{9} N_c \\ &= 3\frac{2}{3} \quad if \ N_c = 3 \ . \end{aligned} \tag{2.15}$$

Figure (2.4)[60] demonstrates that R is constant between the resonant masses. The experimental result is consistent with the prediction of a simple model of quarks with three colours.

The lightest charmed hadrons carry one charmed quark. Their valence–quark contents are listed below.

$$\begin{aligned} D^0 &\sim c\bar{u} \\ D^+ &\sim c\bar{d} \\ F^+ &\sim c\bar{s} \\ \Lambda_c^+ &\sim c(ud)_{I=0} \\ A^0 &\sim csd \\ A^+ &\sim csu \end{aligned} \tag{2.16}$$

The notation '$I = 0$' indicates that the u and d quarks in the ${\Lambda_c}^+$ are arranged in an antisymmetric configuration, with no net isospin. Since the electromagnetic and stong interactions conserve charm, these lightest charmed particles decay weakly.

Weak Interactions

The phenomena of the weak interaction are described in terms of the interactions amongst quarks, leptons and gauge bosons, all of which may be considered as elementary and point–like. Transitions between initial and final states are represented by a time–evolution operator acting on asymptotic basis states. The transition amplitude is given by

$$A(i \rightarrow f) =< final|S|initial > \ . \tag{2.17}$$

The operator S is expressed as a sum of terms involving time–ordered products of the Hamiltonian function ($\mathcal{H}$) associated with the interaction under consideration.

$$S = 1 + i \int \mathcal{H}(x) d^4x - \frac{1}{2!} \int \int T(\mathcal{H}(x)\mathcal{H}(y)) d^4x d^4y + \ldots \tag{2.18}$$

To calculate the energy of a state, or the rate of a reaction, one needs to know the form of the Hamiltonian operator. Both weak and electromagnetic processes can be described by a Hamiltonian density of the following form:

$$\mathcal{H}(x) = g J_\mu(x) W^\mu(x) \ . \tag{2.19}$$

The dimensionless constant g is peculiar to the type of interaction. For example, in electromagnetic processes g is proportional to the electric charge. The 4–vector operator $J_\mu(x)$ (called a current operator) contains all the information about the participating fermions, and $W^\mu(x)$ is associated with a vector boson such as the photon of electromagnetism or the intermediate vector bosons $W^\pm$ and Z^0 of the weak interaction.

Terms in the S–matrix may be associated with space–time graphs of particle interactions. No transitions are associated with the first term in S. The second term corresponds to reactions like the one in figure 2.5. The fermion line is heuristically associated with the current operator in eq(2.19), the W particle with the W^μ, and the amplitude is proportional to the 'coupling–constant' g. Such a reaction does not occur, however, since it is kinematically forbidden.

The simplest real reaction corresponds to the third term in S, and is represented by figure 2.6. A 'virtual' particle is exchanged between two fermion currents. Processes of this sort include e^+e^- annihilation (fig. 2.3), muon decay (fig. 2.7) and charmed quark decay (fig. 2.8).

In so–called charged–currents processes, such as charm decay and charm production, the current takes the form

$$J_\mu = \overline{f}_1 \gamma_\mu (1 - \gamma_5) f_2 \ . \tag{2.20}$$

This describes an incoming fermion of type '2', which changes charge by one unit and turns into a fermion of type '1'. The gamma matrices come from the Dirac equation. Two noteworthy features of the current operator are especially relevant to the discussion of charm decay to follow. The first is the quark content of the fermion operators, which will be treated later. The second is the 'left–handed' nature of J_μ. In the limiting case of massless fermions, the product $\frac{1}{2}(1 - \gamma_5)f$ is a left–handed operator; that is, it describes fermions with negative helicity (left–handed) and anti–fermions with positive helicity (right–handed). Weak reactions involving massless right–handed fermions or massless left–handed anti–fermions do not appear in the standard electro–weak theory. Massive fermions with the 'wrong' helicity participate in weak reactions, but the rates of these reactions are suppressed. This suppression is what is meant by the statement that the weak interaction is not invariant under a parity transformation, or that it does not conserve parity.

One consequence for charm decay is that the decays of the pseudo–scalar mesons to final states with only two fermions are suppressed (the aforementioned helicity suppression). An example is the decay depicted in figure 2.9.

$$F^+ \longrightarrow \tau^+ \nu_\tau \tag{2.21}$$

This is an 'annihilation' decay. The component c and $\overline{s}$ quarks annihilate to form a W^+, which turns into a τ^+ and a ν_τ. The decay of another pseudo–scalar meson, the D^0, is shown in figure 2.6. In the 'free quark' approximation, that is, neglecting the effects of gluons, the c and $\overline{u}$ quarks form a 'spin–0' system and,

through the exchange of an intermediate boson W, change into s and $\bar{d}$ quarks. Free quarks apparently do not exist, and single–body final states are kinematically forbidden, so that other quarks must be created from the vacuum to combine with the s and $\bar{d}$ as they move apart. Nevertheless, before the quarks separate, they are approximately free.

The magnitude of the effect of the $(1-\gamma_5)$ operator on charm decays may be estimated by examining the simpler and better understood decay of the charged pion (fig. 2.12).

$$\begin{aligned} \pi^+ &\longrightarrow \mu^+\nu_\mu \\ &\longrightarrow e^+\nu_e \end{aligned} \tag{2.22}$$

This operator causes the pion to decay to $\mu^+\nu_\mu$ far more often than it does to $e^+\nu_e$, despite the fact that the phase space available for the electronic mode is approximately 3.5 times larger.

$$\begin{aligned} \frac{\textit{phase space } (\pi \to e\nu)}{\textit{phase space } (\pi \to \mu\nu)} &= \frac{({m_\pi}^2 - {m_e}^2)^2({m_\pi}^2 + {m_e}^2)}{({m_\pi}^2 - {m_\mu}^2)^2({m_\pi}^2 + {m_\mu}^2)} \\ &= 3.5 \end{aligned} \tag{2.23}$$

Angular momentum conservation requires leptons in the final state to have identical helicities. Since the $(1-\gamma_5)$ operator requires the massless anti–neutrino to be right–handed, its leptonic partner must be right–handed. If the second lepton were also massless, the reaction would be forbidden. However, since there are inertial frames in which the massive, right–handed lepton appears to be left–handed, the $(1-\gamma_5)f$ operator must contain an admixture of left–handed lepton. The 'number density' of such frames is proportional to $(1-\beta)$, where β is the lepton's velocity in the pion's frame. Consequently, the rate of the reaction is also proportional to $(1-\beta)$. In a two–body decay, β is determined by the masses of the reactants.

$$1-\beta = \frac{2{m_\ell}^2}{{m_\pi}^2 + {m_\ell}^2} \tag{2.24}$$

Combining this with the ratio of phase spaces yields the following ratio:

$$\begin{aligned}\frac{rate(\pi \to e\nu)}{rate(\pi \to \mu\nu)} &= \frac{{m_e}^2({m_\pi}^2 - {m_e}^2)^2}{{m_\mu}^2({m_\pi}^2 - {m_\mu}^2)^2} \\ &= 1.23 \times 10^{-4},\end{aligned} \tag{2.25}$$

in agreement with the observed branching ratio[20] (neglecting a small factor stemming from radiative corrections).

This result may be used to estimate the leptonic decay rate of the F. It is proportional to the phase space and helicity factors derived above. In the simpler case of $F \to \mu\nu_\mu$, the rate can only depend on five other quantities; G_F, m_F, $\hbar$, c and F_F. The latter is the pseudo–scalar decay constant, which is related to the wave function at the origin of the component quarks. Since $m_\mu \ll m_F$, m_μ is negligible except as it affects the helicity and phase space factors already discussed. The expression for the rate has the form

$$\Gamma(F \to \mu\nu_\mu) \propto G_F^2 F_F^2 (m_F^2 - m_\mu^2)^2 m_\mu^2 \hbar^a c^b m_F^d, \tag{2.26}$$

where a, b and d are exponents to be determined. It will be shown later, in connection with muon decay, that G_F has the dimensions of m^{-2}. A dimensional analysis then shows that the rate is proportional to m_F^{-3}.

The expressions for $\Gamma(\pi \to \mu\nu_\mu)$ and $\Gamma(F \to \tau\nu_\tau)$ have the same form, so that[29]

$$\begin{aligned}\frac{\Gamma(F \to \tau\nu_\tau)}{\Gamma(\pi \to \mu\nu_\mu)} &= \left(\frac{F_F}{F_\pi}\frac{m_\tau}{m_\mu}\frac{({m_F}^2 - {m_\tau}^2)}{({m_\pi}^2 - {m_\mu}^2)}\right)^2 \left(\frac{m_\pi}{m_F}\right)^3 \\ &\sim 3050 \\ \Gamma(F \to \tau\nu_\tau) &\sim \frac{3050}{\tau(\pi)} \\ &\sim 1.2 \times 10^{11} s^{-1}\ .\end{aligned} \tag{2.27}$$

F_π is the constant of proportionality associated with π decay, and can be calculated from the measured pion lifetime. The value is 133 MeV[29]. F_F requires a more

subtle and uncertain calculation, based on QCD; the value is (275 ± 95) MeV[30]. Combined with the lifetime of the F[31,32], equation 2.27 yields a branching ratio of approximately 2.3% .

$$BR(F \to \tau\nu_\tau) = \tau_F \Gamma(F \to \tau\nu_\tau) \tag{2.27a}$$

The same arguments can be applied qualitatively to the 'exchange' mechanism of figure 2.6. The 'decay' $D^0 \to s\bar{d}$ suffers from the same helicity suppression. In a 'free quark decay' model of charm decay, this process contributes little to the D^0 decay rate.

The other noteworthy feature of the current (eq. 2.20) is the quark content of the fermion operators. It is noteworthy since the details of how the quarks interact determine the characteristics of charm decay. The expression for the current may be rewritten in a more economical form

$$\begin{aligned} J_\mu &= \overline{f}_1 \gamma_\mu (1 - \gamma_5) f_2 \\ &= \overline{f}_{1L} \gamma_\mu f_{2L} \end{aligned} \tag{2.28}$$

where the subscript L is a reminder that $(1 - \gamma_5)f$ is a left–handed operator. In equation 2.28, $\overline{f}_{1L}$ is a row vector and f_{2L} is a column vector whose elements define the quark weak eigenstates q'_L. The first set of quark fields comprises one member from each isospin doublet and the second set contains the other members of the doublets.

$$\overline{f}_{1L} = (\overline{u}_L, \overline{c}_L, \overline{t}_L) \qquad f_{2L} = \begin{pmatrix} \overline{d}'_L \\ \overline{s}'_L \\ \overline{b}'_L \end{pmatrix} \tag{2.29}$$

The quarks may also be described in terms of their mass eigenstates. These correspond to the wave functions of the physical particles, which have well–defined masses. The mass eigenstates q_L are defined by the so–called mass terms in the

Lagrangian

$$\mathcal{L}_{mass} \sim \sum_{i=1,2} m_{quark} \overline{\psi}_{iL} \psi_{iR} \tag{2.30}$$

where L and R stand for left– and right–handed, and $\overline{\psi}_{iL}$ and ψ_{iR} are given by

$$\overline{\psi}_{1L} = (\overline{u}_L, \overline{c}_L, \overline{t}_L) \qquad \psi_{2R} = \begin{pmatrix} d_R \\ s_R \\ b_R \end{pmatrix} \tag{2.31}$$

The weak eigenstates of equation 2.29 and the mass eigenstates of equation 2.31 need not be identical.

In general, the current can also be written in terms of the mass eigenstates.

$$J_\mu = \overline{\psi}_{1L} \gamma_\mu U \psi_{2L} \tag{2.32}$$

It can be shown that the mass eigenstates and the weak eigenstates are related by a unitary transformation, U.

As written in equation 2.28, the current links the weak eigenstates of set 1, u, c and t with the weak eigenstates of set 2, d', s' and b' respectively. In equation 2.32, the physical states of set 1 are linked with mixtures of the physical states of set 2. The mixtures are specified by the matrix U. In a model with six quarks, this is the Kobayashi–Maskawa matrix[33], which is characterized by four free parameters. The magnitudes of the elements are given in equation 2.33[61].

$$U = \begin{pmatrix} 0.9710 \; to \; 0.9748 & 0.218 \; to \; 0.224 & 0 \; to \; 0.01 \\ 0.192 \; to \; 0.288 & 0.66 \; to \; 0.98 & 0.037 \; to \; 0.053 \\ 0 \; to \; 0.14 & 0 \; to \; 0.72 & 0 \; to \; 0.999 \end{pmatrix} \tag{2.33}$$

The relative sizes of the matrix elements determine which final states are more likely to be produced in charmed–particle decays. It can be seen, by expanding equation 2.32,

$$J_\mu = U_{21} \overline{c}_L \gamma_\mu d_L + U_{22} \overline{c}_L \gamma_\mu s_L + U_{23} \overline{c}_L \gamma_\mu b_L \tag{2.33a}$$

that charm decays depend on U_{21} and U_{22}. Charmed hadrons cannot decay to the (heavier) mesons containing the b quark, so that charm decays don't depend on U_{23}. Since the amplitude of a simple reaction (fig. 2.8) is a quadratic function of the Hamiltonian, so that the rate is a quartic function, and since U_{21} is less than U_{22}, reactions which change strangeness by one unit ($s_f - s_i = -1$) will occur more often than reactions that don't change strangeness. In particular, it is to be expected that final states of D^0 decays frequently contain a K^- or a K^0.

Generally, the physical leptons are mixed in the same way as hadrons. As in the hadronic case, there are two sets of leptons:

$$\psi_{1L}^{lepton} = \begin{pmatrix} e_L \\ \mu_L \\ \tau_L \end{pmatrix} \qquad \psi_{2L}^{lepton} = \begin{pmatrix} \nu_{eL} \\ \nu_{\mu L} \\ \nu_{\tau L} \end{pmatrix} . \tag{2.34}$$

However, in contrast to the hadronic case, the elements of set 2, the neutrinos, may be massless. If they are massless, then the physical eigenstates and the weak eigenstates may be defined to be identical. The leptonic current is then

$$J_\mu^{leptonic} = \overline{e}_L \gamma_\mu \nu_e + \overline{\mu}_L \gamma_\mu \nu_\mu + \overline{\tau}_L \gamma_\mu \nu_\tau \ . \tag{2.35}$$

It will suffice for the study of charm decay to ignore the b and the t quarks. The simplified 2×2 matrix U then has only one parameter, the Cabibbo angle θ. The amplitude for a reaction involving

$$c \longrightarrow s \tag{2.36}$$

is proportional to $\cos\theta$; amplitudes involving

$$c \longrightarrow d \tag{2.37}$$

are proportional to $\sin\theta$. Since $\cos\theta$ is nearly unity ($\cos\theta = 0.9737 \pm .0025$)[20], reactions like 2.37, known as Cabibbo–suppressed reactions, are less probable than those like 2.36, Cabibbo–favoured reactions.

Decays

In the naïve model of charm decay, the dominant mechanism is W–radiation. This is shown in figure 2.8. An examination of the simpler, formally identical processes of muon and τ decays demonstrates that the rates of such reactions may be calculated reliably.

The amplitude for the muon decay is determined by the third term in the S–matrix. It may be rewritten such that

$$A \sim g^2 \int J^\mu(x) T_{\mu\nu}(x,y) J^\nu(y) d^4x d^4y \tag{2.38}$$

where $T_{\mu\nu}$ describes the exchange of a virtual W. Further revision yields

$$\begin{aligned} A &\sim g^2 \int d^4x J^\mu(x) V_\mu(x) \\ V_\mu &= \int T_{\mu\nu}(x,y) J^\nu(y) d^4y \ . \end{aligned} \tag{2.39}$$

This may be interpreted as the scattering of a current J^μ, associated with the $(\mu\nu_\mu)$ pair, from a vector potential V_μ associated with the $(e\nu_e)$ pair. In the analogous electromagnetic case, a virtual photon is associated with a potential that satisfies Maxwell's equations. In the case of weak interactions, the W is associated with a potential that satisfies Maxwell's equations in a form appropriate for a massive vector field:

$$(\partial_\nu \partial_\nu + M_W^2) V^\mu - \partial^\mu \partial^\nu V_\nu = j^\mu \tag{2.40}$$

where the current j^μ is associated with the e and the ν_e. The solution for the Fourier transform (or, equivalently, the plane–wave) is

$$\hat{V}^\mu = \Big(\frac{-g^{\mu\nu} + q^\mu q^\nu / M_W^2}{q^2 - M_W^2} \Big) j_\nu \tag{2.41}$$

where q is the 4–momentum carried by the W, M_W is its mass, and $g^{\mu\nu}$ is the metric tensor

$$g^{00} = 1 \ . \tag{2.42}$$

Since $|q|$ is never greater than the mass of the muon, and the W's mass[20] is 80 GeV/c^2, $\hat{V}$ can be well approximated by

$$\hat{V} \sim \frac{1}{M_W^2} h(q) \ . \tag{2.43}$$

The decay rate is then given by

$$\Gamma(\mu \to e\nu\nu) = \frac{g^4}{M_W^4} f(m_e, m_\mu, \hbar, c) \ . \tag{2.44}$$

Details of the dynamics and kinematics are contained in f, a function of the only relevant quantities. If it is assumed that the electron's mass is negligible, then the only remaining quantities are $\hbar$, m_μ and c. A dimensional analysis shows that

$$\begin{aligned} \Gamma &\sim \frac{g^4}{M_W^4} m_\mu^5 \frac{c^2}{\hbar} \\ &\sim \frac{G_F^2 m_\mu^5 c^2}{\hbar} \ . \end{aligned} \tag{2.45}$$

A more thorough treatment verifies this result, and determines the constant of proportionality.

$$\Gamma = \frac{G_F^2 m_\mu^5 c^2}{192\pi^3\hbar} \tag{2.46}$$

The salient feature, that the rate is proportional to m_μ^5, is modified only slightly by electromagnetic radiative corrections.

The significant differences between μ and τ decays are that the τ is heavier, and can therefore decay into several different final states, as shown in figure 2.10. The W^+ materializes as one of three pairs of weak eigenstates, $(u\overline{d}')$, $(e^+\nu_e)$, $(\mu^+\nu_\mu)$, which are mixtures of the physical states. For the purpose of calculating the τ decay rate, the leptonic mass eigenstates are the physical states, since the neutrinos are massless, or nearly so.

The decay of the τ illustrates the effect of colour on W–radiation decays. The weak boson is colourless, so that the $u\overline{d}'$ pair must form a colour singlet. As was

the case in e^+e^- annihilation, the amplitude for this is $\sqrt{1/N_c}$. After a summation of N_c indistinguishable amplitudes, the result for the hadronic decay is

$$A(\tau^+ \to \overline{\nu}_\tau u\overline{d}') = A_0\sqrt{N_c} \tag{2.47}$$

where A_0 is the muon–decay amplitude. The expression for the total rate is

$$\begin{aligned}\Gamma(\tau) &= \Gamma(\tau^+ \to \overline{\nu}_\tau u\overline{d}') + \Gamma(\tau^+ \to \overline{\nu}_\tau \nu_\mu \mu^+) + \Gamma(\tau^+ \to \overline{\nu}_\tau \nu_e e^+) \\ &= \Gamma_0(N_c + 2) \\ \Gamma_0 &= |A_0|^2 \ .\end{aligned} \tag{2.48}$$

The ratio of the τ and muon decay rates is then

$$\begin{aligned}\frac{\Gamma(\tau)}{\Gamma(\mu)} &= (N_c + 2)\left(\frac{m_\tau}{m_\mu}\right)^5 = 5\left(\frac{m_\tau}{m_\mu}\right)^5 \\ &= 6.9 \times 10^6 \ .\end{aligned} \tag{2.49}$$

This is consistent with the accepted value[20], $(6.5 \pm 1.0) \times 10^6$, if $N_c = 3$.

The conclusion is that the decay rate of a free fermion is given by

$$\Gamma(f) = \frac{G_F^2 c^2}{192\pi^3\hbar} m_f^5 \cdot C \tag{2.50}$$

where C is a colour factor, which also accounts for the two open, colourless, leptonic channels.

If W–radiation is the dominant mechanism of charmed hadron decay, then the lifetimes of the charmed hadrons depend primarily on the lifetime of the charmed quark and should be equal. Less restrictively, in a semi–leptonic decay the charmed quark is the only interacting quark, so that the semi–leptonic rates should be equal. A third prediction, the magnitude of the lifetime, depends upon the mass of the charmed quark. It has already been noted that isolated quarks probably do not exist. Consequently, m_c must be estimated indirectly. Since the ψ is a $c\overline{c}$ combination, one estimate of m_c is

$$m_c \sim \frac{m_\psi}{2} \sim 1.55 \text{ GeV/c}^2 \ . \tag{2.51}$$

More sophisticated estimates[35], taking account of hyperfine interactions, yield values such as 1.8 and 1.11 GeV/c^2. The uncertainty in m_c is reflected in a very large uncertainty in the predicted charmed lifetime. This makes difficult any attempt to judge the effects of the other mechanisms contributing to the decay.

To further complicate matters, the s quark is not approximately massless, as were the electron and neutrinos in the two previous examples. If the mass of the strange quark is roughly .5 GeV/c^2, which is half the mass of the $s\bar{s}$ state ϕ, then the phase space volume available for charm decay is smaller by a factor of two[36].

Using the simple approximations $m_c \sim 1.5$ and $m_s \sim .5$, the result is

$$\tau_c \sim 17 \times 10^{-13} s \ . \tag{2.52}$$

With the other two estimates of m_c,

$$\tau_c \sim 3.4 \times 10^{-13} s$$

or

$$\tau_c \sim 38 \times 10^{-13} s \ . \tag{2.53}$$

The Particle Data Group (ref. 20) lists the following values for the lightest charmed hadrons:

$$\begin{aligned} \tau(D^{\pm}) &= 9.2^{+1.7}_{-1.2} \times 10^{-13} s \\ \tau(D^0) &= 4.4^{+0.8}_{-0.6} \times 10^{-13} s \\ \tau(F^{\pm}) &= 1.9^{+1.3}_{-0.7} \times 10^{-13} s \\ \tau(\Lambda_c^+) &= 2.3^{+1.0}_{-0.6} \times 10^{-13} s \ . \end{aligned} \tag{2.54}$$

Clearly, the lifetimes are not identical. However, the predictions 2.52 and 2.53 have the correct magnitude.

The prediction of equal semi–leptonic rates can be tested using the measured semi–leptonic branching ratios[37] and lifetimes determined by this experiment[38].

It can be seen that the semi–leptonic rates of the $D^{\pm}$, the D^0 and the Λ_c^+ are roughly the same.

$$\begin{aligned} \Gamma_{SL}(D^+) &= 1.7 \pm 0.5 \times 10^{11} s \\ \Gamma_{SL}(D^0) &= 1.5^{+0.4}_{-0.5} \times 10^{11} s \\ \Gamma_{SL}(\Lambda_c^+) &= 2.3^{+1.0}_{-1.2} \times 10^{11} s \ . \end{aligned} \tag{2.55}$$

This is consistent with W–radiation being the only significant source of semi–leptonic decays of the $D^{\pm}$, the D^0 and the Λ_c^+. The differences amongst the lifetimes can be ascribed to other mechanisms which contribute to the hadronic decay rates.

Hadrons are superpositions of an infinite number of short–lived quark and gluon fluctuations, of which the simplest is the valence quark state. It was noted earlier that the gluons interact with the quarks and can modify the decay rates of hadrons. Considerable effort has been devoted to quantitatively describing these interactions using QCD. Qualitatively, since the gluons carry colour, they can alter the 'flow' of colour into the final states of reactions like the one in figure 2.8. In the absence of gluons, the initial c and $\overline{q}$ quarks form a colour singlet, and the final state colour singlets are $(s\overline{q})$ and $(u\overline{d})$. Gluon interactions can arrange the final state quarks into two different colour singlet pairs: $(s\overline{q})$ and $(u\overline{d})$; and $(s\overline{d})$ and $(u\overline{q})$. Since there are a great many different, indistinguishable quark–gluon reactions which can produce these two final states, and since these reactions are independent of quark flavours, an increase in the decay rates of all charmed hadrons might be expected.

In the case of the D^+, the two final states are the same. If the two $\overline{d}$'s share the same quantum numbers, the corresponding amplitudes will interfere destructively. Thus, in a qualitative sense at least, there is reason to expect the D^+ decay rate to differ from the decay rates of the other charmed hadrons.

Mechanisms involving the interactions of quarks with gluons can also provide more channels for reactions that otherwise might be expected to be rare, such as charm decays that produce final states without strangeness. W–radiation usually produces strangeness. An example of a process that does not is the so–called 'penguin[39] mechanism', shown in figure 2.11. This contributes to Cabibbo suppressed decays, in some cases coherently, so that the Cabibbo suppressed rates might be greater than would be expected from consideration of W–radiation alone.

In addition to colour, gluons also carry spin. A valence quark pair, in the presence of gluons, has an amplitude to be both a colour singlet and a vector. The two final state fermions also no longer must form a 'spin–0' combination, so that the 'helicity suppression' mechanism may not be as important as suggested earlier. Specifically, the semi–leptonic decay rates of the $F^{\pm}$ might increase, as might the non–leptonic rates of the D^0 and the Λ_c^+, whose exchange amplitudes are no longer suppressed. The annihilation amplitude of the D^+ is Cabibbo suppressed, so that the removal of helicity suppression may not be as significant for D^+ decays.

The 'free quark decay' model only approximately explains charm decay. Although the model does predict the correct order of magnitude of the lifetimes, and although it does predict the equality of the semi–leptonic rates of the D^+, the D^0 and the Λ_c^+, it fails to account for the differences amongst the lifetimes. A more sophisticated model, incorporating some or all of the mechanisms mentioned above, is required to adequately describe the decay process. Buttressing such a model must be new information concerning the properties of the heavier charmed hadrons[40] (*e.g.*, A^0, A^+, A_s^0) and more precise measurements of the branching ratios and lifetimes of the Λ_c^+, the F, the D^+ and the D^0.

Chapter 3

The Experiment

The objectives of this experiment, known as E531, were straightforward: to observe and identify charmed particles, and to measure their lifetimes. Fulfillment of these objectives required apparatus with spatial resolution fine enough to permit the measurement of short decay lengths – typically a few tens to a few thousands of microns – and with the ability to detect and identify all the decay products, and to measure their momenta. To accomplish the latter, and to predict the locations of the neutrino–interaction vertices, a multi–purpose detector[41] (fig. 3.14) was built downstream of the target. This detector was capable of measuring the momenta of charged particles with a magnetic spectrometer, and it could measure the energy deposited by photons in an array of lead glass blocks and by neutrons and long–lived K^0's in a segmented steel calorimeter. Muons were identified by their range in steel. Identification of charged hadrons was based on a combination of measurements of momenta and flight times, and measurements of ionization and scattering in the emulsion.

The necessary spatial resolution was afforded by a target of nuclear emulsion. Indeed, at the inception of E531, the use of nuclear emulsion was the only technique that could achieve such resolution. Target and spectrometer were exposed to the neutrino beam at Fermi National Accelerator Laboratory, in Batavia, Illinois.

The Neutrino Beam

Two considerations suggest the use of a neutrino beam as an instrument with which to produce charmed particles. The first is that charmed particles are produced in neutrino interactions more frequently than in reactions induced by other probes; experimental evidence available prior to the first run of E531

indicated that neutrino charged–current interactions produced charmed final states roughly 10% of the time[42]. An analysis of the data gathered in that run[43] showed that the ratio was $6.5^{+1.9}_{-1.8}\%$. In contrast, only one in a thousand pN interactions results in open charm[44].

A disadvantage of emulsion is that it records the tracks of all charged particles that traverse it between the time it is poured and the time it is developed. Neutrinos are electrically neutral, and thus do not produce the profuse background of confusing tracks that would result from using a charged beam. Those tracks associated with the decaying charmed particles become that much easier to find and follow.

The neutrinos in the beam came from the decays of charged pions and kaons. Charged pions almost invariably produce muons and neutrinos, while nearly 2/3 of all charged kaons produce μ's and ν_μ's. In turn, the mesons were created in collisions between the nucleons in a target of beryllium oxide one interaction length long, and protons that had been accelerated to an energy of 400 GeV/c. If no effort is made, in the focussing process, to minimize the variation amongst the energies of the charged secondaries, the resulting neutrino beam is called a wide–band beam, as opposed to a narrow–band beam, whose component neutrinos have momenta correlated to their positions in the beam.

The electrical neutrality mentioned above also prevents the focussing of a neutrino beam. Instead of focussing neutrinos, one focusses their charged precursors. This was accomplished with a 'horn', a water–cooled, horn–shaped aluminum conductor. During beam spills, a pulse of 140 kA of current flowed through the horn. Each pulse was 100 ms long, to match the beam extraction period. An azimuthal magnetic field, produced by current flowing through the horn in the beam direction, defocussed the negative pions and kaons, and focussed the positive particles,

directing them into an evacuated beam pipe. The less energetic, more divergent particles were more efficiently defocussed than were those moving along the axis of the horn. (Reversing the current focussed negative particles, to eventually create an anti–neutrino beam.)

Inside the pipe, 10% of the pions and 30% of the kaons decayed, producing neutrinos and positive muons. The remaining secondary hadrons, along with the protons that traversed the target, and most, but not all, of the muons, were absorbed in the concrete, the steel and the earth at the end of the decay pipe (fig. 3.1). The neutrinos which reached the site of the experiment had the momentum spectrum displayed in figure 3.2.

Muon–neutrino beams are contaminated principally by four other types of particle: negative and positive muons, electron neutrinos and muon anti–neutrinos. Negative muons are produced in collisions between the ν_μ's and the nucleons in the series of absorbers between the end of the decay pipe and the emulsion target. Some positive muons from π and K decays don't interact in the berm, and so contribute to the contamination. Electron neutrinos in the beam arise from the semi–electronic decay modes of both charged and neutral kaons.

$$\begin{aligned} K^{\pm} &\rightarrow \pi^{\circ} e^{\pm} \nu_e(\overline{\nu}_e) \;\; B.R. = 4.8\% \\ K_L &\rightarrow \pi^{\mp} e^{\pm} \nu_e(\overline{\nu}_e) \;\; B.R. = 38.8\% \end{aligned} \tag{3.1}$$

Neutrino beams are further polluted by $\overline{\nu}$'s (and *vice versa*). In the latter case, the neutrino flux is actually greater than the anti–neutrino flux at energies exceeding 60 – 80 GeV, an observation that finds an intuitive explanation in a simple quark model. Some of the beam neutrinos arise from the decay of strangeness, incarnated in the kaons produced in the pN collisions. This strangeness must come from the quark ocean in either the target or the projectile. If an s quark is

to form a meson, such as a K^-, the anti–quark partner must also be plucked from the ocean, because there are no valence anti–quarks in nucleons. Alternatively, if the final meson is to carry an $\bar{s}$ anti–quark, as does a K^+, it need only combine with one of the six valence quarks in the proton and the target nucleon. The K^+'s thus created have higher momenta than do K^-'s. This is because the valence u and d quarks in the projectile and target nucleons are more likely to carry larger fractions of the nucleon momenta than are the ocean quarks. Since the more energetic mesons tend to emerge from the BeO target at small angles to the beam axis, they are poorly defocussed. Energetic K^+'s, which decay to neutrinos, thus contribute significantly to a $\overline{\nu}$ beam. Furthermore, the s and $\bar{s}$ are more likely to materialize as a K^+ and a $\overline{K^\circ}$ than to materialize as a K^- and a K° because the charge of the initial particles is positive. A plug[62], inserted along the axis of the secondary beam, reduced the number of K^+'s and increased the ratio of high–energy $\overline{\nu}$ flux to high–energy ν flux at the target when the horn current was chosen to focus negative particles.

The Emulsion Target

Thirty litres of Fuji emulsion constituted the target (figures 3.3 and 3.4) for E531. Table 1 lists its chemical constituents.

Table 1.

Element	Percentage by weight
Silver	46.5
Bromine	33.7
Carbon	7.4
Oxygen	4.3
Nitrogen	2.7
Iodine	1.31
Hydrogen	0.92
Sulfur	0.4

Chemical Composition of Fuji ET–7B Emulsion

It was divided into two batches, and each batch was exposed to the neutrino beam in a different orientation, to fully exploit the advantages of using emulsion. The first batch was made of 'vertical' pellicles which were strips of polystyrene 12 cm by 9.5 cm by 70 μm, coated on either side with 330 μm of emulsion. The strips were mounted as modules in a plane perpendicular to the beam direction. Each module contained 98 pellicles, a total depth of 7 cm of emulsion. The vertical orientation had the advantage that, in the presence of a background of many charged tracks, the search for neutrino interactions and charm decays was more efficient than in the horizontal modules described below. Furthemore, it was easier to follow tracks from the spectrometer into the vertical emulsion than into the horizontal emulsion[51].

Horizontal pellicles were arranged so that the beam was incident parallel to the sheets. Horizontal modules consisted of 108 sheets of solid emulsion, 7 cm by 14 cm by 600 μm. This orientation had two attractive features. First, each event presented an easily recognizable topology. Secondly, the best spatial resolution near the neutrino interaction could be achieved by presenting the emulsion to the beam in this way.

Wrapped in polylaminated paper, the modules were mounted on a precisely–machined frame of solid aluminum and aluminum hexcell. The hexcell structure reduced to an acceptable level the amount of inactive material in which the neutrinos could interact, while providing adequate support strength for the target. One corner of the frame was fixed while the others were free to move in case of expansion or contraction. A system of linear variable differential transformers (LVDT's), with a spatial resolution of 15μm, monitored such motion.

A large sheet of emulsion was placed immediately downstream from the target. This fiducial (or 'changeable') sheet was constructed from a lucite base 91.5 cm by 70 cm by 800 μm, and was coated on both sides with 75 μm of emulsion. It acted as a detector with fine spatial resolution and little background, so that tracks reconstructed in the drift chambers could be found in the changeable sheet and then be followed into the emulsion.

Several design features made this process highly efficient. The positions of the modules with respect to the changeable sheet were marked on the sheet by ^{55}Fe X–ray sources embedded in the corners of each module. Sixteen more sources, mounted around the perimeter of the aluminum frame, were used to locate the fiducial sheet relative to the spectrometer. To reduce the movement of the emulsion with respect to the spectrometer, the support frames for the target and the drift chambers were placed on a 3.5 ton, optically flat, granite block. Residual motion was recorded by the LVDT's. Once a week during the data-taking period, the sheet was changed to keep the number of background tracks to a manageable level. Finally, an air–conditioner maintained the temperature of the emulsion at $(10 \pm 2)^\circ$C. Clouding and image fading were reduced in this manner.

The emulsion could also be used as a particle identifier, since it recorded the scattering behaviour of a particle and the ionization along its track. As a

charged particle passes through matter, it collides with the atomic nuclei. Most of the resulting deflection is due to multiple Coulomb scattering, although the strong interaction contributes to scattering of hadrons. The distribution of planar scattering angles may be approximated by a Gaussian distribution, with a standard deviation given by

$$\theta_0 = \frac{14.1}{p\beta} Z_{inc} \sqrt{\frac{L}{L_R}} \left(1 + \frac{1}{9} \log_{10}\left(\frac{L}{L_R}\right)\right) \tag{3.2}$$

where θ_0 is in radians, p (the momentum of the projectile) is in MeV/c, Z_{inc} is the charge of the incident particle, and L/L_R is the thickness of the material traversed, in units of radiation lengths. When the polystyrene was taken into account, the radiation lengths in the horizontal and vertical emulsion were 29.4 and 32.0 mm respectively. Using equation (3.2), it was sometimes possible to estimate $p\beta$ for particles with low momenta by estimating the extent to which a particle scattered and comparing that to the expected width of the distribution.

This scattering information could be combined with a measurement of the ionization along a particle's trajectory to identify the particle. The ionization caused by a charged particle is a record of the energy it lost in inelastic collisions with atomic electrons. The average energy lost in such collisions depends on the particle's velocity, and not on its momentum or its mass. Hence, for a given value of $p\beta$, different particles will, on the average, lose different amounts of energy. To estimate the average energy lost in emulsion, one measures the average grain density along a track. In practice, the ratio I/I_0 is determined, where I_0 is the average energy lost by a particle in the Fermi plateau region. Using figure 3.5, one could estimate the likelihood of a (slow) particle being one of the five (e, μ, π, K, p) expected to live long enough to leave visible tracks in the emulsion, and thus complement the particle identification capacity of the time–of–flight system.

The Time–of–Flight System (TOF)

The time–of–flight[45] system played two roles. It measured the time taken for a charged particle to transit the anterior part of the spectrometer, hence the system's name, and it constituted part of the electronic trigger which initiated the acquisition of data.

The first time–of–flight counter (TOF I) abutted the downstream face of the target. The counter was a rectangle of Pilot F scintillator, 1 cm thick and 74 cm by 92 cm, viewed from four sides by twelve phototubes (fig.3.6). Ideally, the ionization from a track was detected by at least one photomultiplier on each of the sides.

Situated 2.75 m downstream from the target was the second time–of–flight counter (TOF II) (figure 3.7). This vertically–oriented hodoscope comprised sixteen narrow counters (7.0 cm by 150.0 cm by 2.5 cm) and eighteen wide ones (10.2 cm by 150.0 cm by 2.5 cm). The narrow counters, with their superior time resolution, were placed in the centre of the experiment, along the beam axis, where most of the charged particles passed. All counters were fashioned from Pilot F scintillator and were viewed from both ends by photomultiplier tubes.

During the data–taking period, the TOF system was continuously monitored. The high voltage supplied to the phototubes was held constant to within 1 volt. The timing and gains of all the tubes were monitored using beam muons and pulses of laser light. Between beam spills, a nitrogen laser was fired, and the light was carried to all the counters along optical fibres.

Muons were also used to calibrate the system. Calibration tracks were chosen such that there was only one track reconstructed in the drift chambers and that

the pulse height in TOF I was consistent with only one minimum–ionizing particle. The data from 220,000 muons were collected, and this condition was satisfied in 44,000 cases. Both calibration and neutrino data were recorded by ADCs and TDCs.

The estimate of the 'start time' of a neutrino event could be made more precise than a TOF I measurement alone, by using particles in the event whose values of β could be calculated independently of TOF. This group comprised particles identified as muons or electrons, and particles so fast ($p > 10$ GeV/c) that their values of β differed negligibly from 1.0. For each of the particles of known β, start times were calculated using momenta and flight lengths measured in the drift chambers. These values were combined with the TOF I start time in a weighted average. Tracks irrupting from the target hit TOF I in different places; accordingly, the TOF I start time took into account the rms 'cluster size' of the tracks. With this more precise start time, more precise flight times could be calculated for the particles to be identified by TOF.

The resolution of the narrow counters was 75 ps, and for the wide counters it was 100 ps (when there was a single track in a paddle and both top and bottom tubes were on). The resolution of TOF I (with all four tubes on) was 100 ps. Given these resolutions, and the separation between TOF I and TOF II, the average flight times of 7 GeV/c pions and protons differred by one standard deviation. Pions and kaons could be similarly distinguished if the momenta were less than 3 or 4 GeV/c. The distribution of particle masses determined by the time–of–flight system is displayed in figure 3.16.

A particle was identified by comparing its value of β calculated from its flight time, and the value expected for the different possibilities (e, μ, π, K, p), given

the measured momentum.

$$\beta_{pred} = \sqrt{\frac{p^2}{m^2 + p^2}} \tag{3.3}$$

A value of chisquared and a confidence level were associated with each hypothesis to determine the best one.

$$\chi^2 = \left(\frac{\beta_{pred} - \beta_{meas}}{\sigma_{meas}} \right)^2 \tag{3.4}$$

The Trigger

The second function of the TOF system was as a component of the data–acquisition trigger. The spectrometer was capable of recording but one neutrino interaction per beam spill, so that care was required to distinguish authentic neutrino interactions from signals produced by charged particles in the beam. A minimally biased trigger allowed the recording of both muon tracks for calibration, and neutrino events.

The signature of the decay of a ν–produced charmed particle was simple: no charged particles entered the target and at least two left. The two particles were the muon from the charged–current production reaction and one particle from the decay. This signature was mirrored in a particular pattern of signals from the detectors: a total TOF I signal $2\frac{1}{2}$ times the average minimum-ionizing signal, a total TOF II pulse twice the minimum–ionizing value, and no signal at all from the veto array. In symbolic terms, the neutrino trigger, T_ν, was

$$T_\nu = G_\nu \bullet \overline{V} \bullet TOF\ I_{\geq 2\frac{1}{2}} \bullet TOF\ II_{\geq 2}. \tag{3.5}$$

Since some TOF II paddles overlapped, the condition $TOF\ II_{\geq 2}$ did not necessarily imply the presence of two particles. In equation (645), a '•' stands for a coincidence, 'G_ν' for the neutrino gate, and 'V' for a signal from the veto counters.

The veto counters, seven scintillators that were viewed from both ends by photomultipliers, were placed directly in front of the emulsion target. There they served to reject reactions initiated by charged particles in the beam. Occaisionally, charged particles were expelled backwards from the neutrino interaction, and their signals in the veto array would have caused the event to have been rejected as bogus. In order to avoid this, and thus in order to avoid losing potential charm decays, the signal delay times were carefully adjusted.

The neutrino gate, G_ν, was the time period during which neutrino triggers were accepted. Neutrinos passed through the experiment in 1ms bunches; a gate of 10ms duration was more than adequate to cover this. A signal from the accelerator started the gate pulse.

Calibration data, from beam muons, were recorded during the last 5% of each spill. Expressed symbolically, the trigger was

$$T_\mu = G_\mu \bullet TOFI_{\geq 1} \bullet TOFII_{=1} \tag{3.6}$$

where G_μ is the muon gate.

The Drift Chambers

After the system had been triggered, the drift chambers[46,47] recorded the passage of charged particles. These data were used for two purposes. The first was to reconstruct tracks in three spatial dimensions. The tracks could then be followed into the emulsion, where they led to neutrino interactions, charmed and strange particle decays, and photon conversions. The tracks could also be followed further into the spectrometer in order to associate signals in the calorimeters with charged particles, paving the way for the identification of neutral particles in the events. The second purpose of the drift chambers was to measure the momenta

of charged particles. These measurements were used to kinematically reconstruct the charmed and strange particle decays.

When a charged particle passed through the drift chambers, which were filled with equal volumes of argon and ethane gases, it left in its wake a trail of ion clusters. Pulled by an electric field, the ionization electrons drifted toward an anode. Since the electrons drifted with a nearly constant velocity, the time taken to reach the sense wire was also a measure of the distance of the original track from the wire. From this measurement alone it could not be determined from which direction the electrons drifted. This ambiguity was resolved with a technique described later in this section.

Each chamber determined two coordinates of a track: the position of the chamber itself along the beam direction was the z coordinate, and the position relative to the sense wire in a direction perpendicular to both the beam direction and the orientation of the wires was the other coordinate. For instance, a chamber with wires in the vertical (y) direction determined the horizontal (x) coordinate.

Twenty–four drift chambers, deployed at different angles relative to the vertical axis, and a vertical–dipole magnet formed the magnetic spectrometer. The field inside the magnet was not uniform, but it was well known from a map with approximately 45,000 measurements made at 2.5 cm intervals. Outside the mapped region, the field strength was estimated using a polynomial parameterization.

Fifteen drift chambers (figure 3.8) were placed between TOF I and the magnet. Those rotated $-60°$ ($60°$) around the beam axis were classified as 'U' ('V') chambers. Arranged in V–U–X triplets, alternate groups were displaced by one half–cell width, transverse to the wire direction, in the plane of the chambers, to remove the left–right ambiguity mentioned above.

Each upstream chamber presented to the beam a total active area of 128 cm by 128 cm. Neighbouring planes were separated by 4.7 cm. Thirty–two drift cells, 4 cm wide, each contained a gold–plated tungsten sense wire. A drift field of 700 V/cm was used in the outer regions of the cell. Near the sense wire, the field increased proportionally with the inverse of the radius to provide the necessary gas amplification.

Further downstream, between the magnet and TOF II, stood the remaining nine chambers. They were placed in the following order: V–X–U–X′–X–V′–X′–U′–X, the prime indicating a shift in position of half a cell. These chambers were larger and had longer wires than their upstream counterparts, so the angles of rotation with respect to the vertical had to be smaller ($\pm 11^\circ$ for U and V), to prevent the wires from sagging significantly under their own weight. With an active area of 203 cm by 118 cm, the X chambers comprised 40 cells, each 5.08 cm wide. Presenting the same cross-section, the U and V chambers contained 43 and 44 sense wires respectively. An drift field of 750 V/cm was maintained in the downstream chambers.

All drift chamber signals were amplified by a factor of 100 and were required to exceed a discriminator threshold before being transformed into standard NIM pulses. A multi-hit digitization system was the next stage in the signal-processing procedure. The unit of digitization was 1.5 ns, which corresponded to 75μm in space. Subject to a dead time of 36 ns, which prevented the resolution of hits closer than 1.8 mm, the system could register up to 15 hits per wire.

With this resolution, the drift chambers could record data from more than one event per beam spill (for instance, the track of a calibration muon, and the tracks from a neutrino interaction). Muons in the neutrino beam were employed

to calibrate the drift chambers. A tuning programme calculated track-fitting parameters (such as drift velocity, which was about 50 μm/ns), for use in subsequent reconstruction of tracks from neutrino interactions, and in the measurement of their momenta.

The momentum of a charged particle whose trajectory is bent by an angle θ is given by

$$P\theta \simeq 0.03 \int Bdl \tag{3.7}$$

where the average line integral in the E531 spectrometer is 6.2×10^3G-m. The average horizontal momentum given to a charged particle, Pθ, was approximately 186 MeV/c. Positive particles were deflected to the right of the magnet (facing downstream) (fig. 3.9).

For tracks that passed through the magnet and all 24 chambers, the (rms) momentum resolution was

$$\frac{\sigma(P)}{P} = \sqrt{.014^2 + (.004P)^2} \tag{3.8}$$

Multiple Coulomb scattering in the air, the drift chambers, and in the ionization chamber between the magnet poles contributed to the first term. The other term is due to the drift chamber spatial resolution. If a track did not pass through the magnet, its momentum could still be estimated, but with much less precision, from its curvature in the fringe field.

$$\frac{\sigma(P)}{P} \geq .08P \tag{3.9}$$

The Charged Particle Identifier (CPI)

A large proportional ionization chamber (CPI)[48] was placed inside the magnet gap. The purpose of this detector was to identify the relativistic particles that passed through it by sampling the ionization created along their tracks. As mentioned in the section dealing with the emulsion, the ionization (and hence the energy lost) is a function neither of mass nor of momentum, but of velocity. Consequently, different particles having identical momenta will lose, on average, different amounts of energy. Over a range of velocities between $\beta\gamma = 5$ and $\beta\gamma = 1000$, the energies lost by pions and protons, in the argon–cabon dioxide mixture we used, differ by about 26%, and the losses of pions and kaons differ by about 16%[49]. The goal of the CPI was to identify charged particles in this region.

The ionization along a track was sampled fifty times, in proportional cells 2 cm in the beam direction by 1 cm (figures 3.10 and 3.11). Ionization electrons drifted towards one of two planes of sense wires. The drift field was provided by three high–voltage planes, one each at the top and bottom, and one in the middle, and by field–shaping wires encircling the chamber. Each anode in the signal plane was surrounded by six cathodes.

The chamber was filled with a mixture of gases that was 80% argon, by volume, and 20% carbon dioxide. Temperature and pressure within were monitored with temperature and pressure transducers. Before entering the CPI, the gas passed through an oxygen trap and a water absorber.

The Electromagnetic Shower Detector

The purpose of the lead glass system was to detect photons, identify electrons, and measure their energies. This information was neccessary to infer the presence

of neutral pions, which decay to two photons. Electrons and photons produced electromagnetic showers in a lead converter and in blocks of lead glass. Extruded proportional ionization counters (EPIC's) detected the ionization caused by the showers in the converter, and the light produced by the electrons in the lead glass was collected by photomultipliers. The total amount of light was proportional to the energy deposited by the shower after the EPIC's.

Sixty-eight blocks of lead glass, 19 cm by 19 cm in cross-section, were arranged as shown in the figure 3.12. Blocks in the centre of the array, 35.6 cm (12.5 radiation lengths) in length, were composed of SF2 lead glass. The remaining blocks, 30.5 cm in length (10.5 radiation lengths), were fashioned from F2 lead glass.

Signals from the photomultipliers were amplified, split in the ratio of 20:1, and recorded by ADC's. This provided a range large enough to measure the energy lost by minimum–ionizing particles, and the energies of the electromagnetic showers. The maximum energy measureable by each block was approximately 35 GeV.

The resolution of lead glass improves with the energy measured. Since the longer blocks were more likely to fully absorb very energetic showers, and since most of these were expected to fall in the centre of the array, close to the beam axis, all of the long blocks were mounted in the centre of the lead glass system, except for one which was needed for the test beam calibration.

The blocks were calibrated using data from tests of one block of each type in the M5 test beam at Fermilab. Data for electrons and minimum–ionizing particles were recorded for beam energies extending from 5 to 30 GeV. Taking into account the non–uniform response of the blocks across their faces, it was established that a minimum–ionizing particle deposited, on average, 397 $\pm$ 13 MeV in a long block,

and 333 $\pm$ 13 MeV in a short block.

During data-taking, the blocks were calibrated using beam muons. Relative gains and ADC calibrations were monitored using light from a neon flash tube, fired between beam spills. Optical fibres carried the light to the front of each block.

Since the blocks were approximately .7 hadronic interaction lengths long, some hadrons deposited considerably more energy than muons of the same momenta. Consider the case of 30–GeV pions. The energy–loss spectrum is shown in figure 3.13. The abscissa is graduated in pulse height units, and the peak correponding to the 30–GeV electrons in the test beam is clearly visible. The pion interaction spectrum has an exponential form, with a coefficient equal to -.0095 (channel)$^{-1}$. The probability that a 30–GeV pion will lose an energy equivalent to a pulse heght of Z or greater is the ratio of the area under the spectrum from Z to infinity, divided by the total area.

$$P = \frac{1}{2} \frac{\int_Z^\infty e^{-\alpha E} dE}{\int_0^\infty e^{-\alpha E} dE} \tag{3.10}$$

The factor 2 accounts for the energy lost in inelastic electromagnetic collisions, reflected in the area under the minimum-ionizing peak, which is just visible at the low–energy end of figure 3.13. For example, a 30–GeV pion will lose roughly one third or more of its energy ten percent of the time.

The EPIC's formed the other active element in the electromagnetic calorimeter. Filled with equal amounts of argon and ethane, three planes of EPIC's were placed immediately in front of the lead glass array, sandwiched between the blocks and a lead converter (2.8 radiation lengths). Each EPIC cell was 2.54 cm deep, 2.54 cm wide, and contained a stainless steel anode wire, .38μm in diameter. Wires

in the 'Y' plane were strung horizontally, while the wires in the 'U' and 'V' planes were rotated from the horizontal by $\pm 60°$ (fig. 4.5). The uncertainty in position measurements made with the EPIC's was 0.75 cm in the 'Y' direction, and was slightly worse in the 'X' direction. Since the EPIC system was approximately 312 cm downstream from the target, the uncertainty associated with the slopes of reconstructed photons was close to three milliradians. The EPIC signals were calibrated in terms of the equivalent number of minimum ionizing muons.

The energy resolution of the lead glass alone was

$$\frac{\sigma(E)}{E} = \frac{.15}{\sqrt{E}}. \tag{3.11}$$

Including the energy lost in the EPIC's, the resolution was

$$\frac{\sigma(E)}{E} = \sqrt{\left(\frac{.15}{\sqrt{E}}\right)^2 + \left(\frac{E_{epic}}{\sqrt{MIPE}}\right)^2 + .05^2} \tag{3.12}$$

where MIPE is the number of minimum–ionizing –particle–equivalents in the EPIC's, averaged over three views. Since minimum–ionizing particles lost .02 GeV as they passed through the EPIC's, this can be rewritten as follows:

$$\frac{\sigma(E)}{E} = \sqrt{\left(\frac{.15}{\sqrt{E}}\right)^2 + \left(.02\sqrt{MIPE}\right)^2 + .05^2}\ . \tag{3.13}$$

The Hadron Calorimeter

The segmented hadron calorimeter measured the energies of hadrons produced in neutrino interactions, including neutrons and long–lived neutral kaons, which were not detected in the other spectrometer elements. Each segment consisted of 10 cm of steel, followed by an active element. The first three active elements were EPIC's, which could also determine the position of the hadronic showers. The last three active elements were scintillators. Some of these were fashioned from

NE110 scintillator, and the rest were made of NE114 scintillator. Each paddle, 1.3 cm thick, 76.2 cm (30 inches) wide and 2.44 m tall, was viewed from the top by a photomultiplier. All signals were recorded by ADC's.

The three anterior active elements were EPIC's. Each aluminum extrusion, filled with the same argon–ethane mixture that filled the drift chambers and the lead glass EPIC's, contained a wire 0.38 μm in diameter. Each plane of wires comprised eight channels. Strung horizontally, so that the y position of the wire gave the y position of a hit, the wires were arranged in groups of four. An ADC recorded a logical **OR** of the signals from each quartet. If it is known that a pulse is from one of the four neighboring cells, each 2.54 cm (1.0 in) wide, it is equally likely that the signal comes from any one of the four. Consequently, the uncertainty in the y position is given by

$$\sigma(y) = \frac{10.0}{\sqrt{12}}\ cm \tag{3.14}$$

where the factor of 12 is due to a uniform probability distribution within boundaries.

One can estimate the x position of a track using the calorimeter, because the EPIC wires were resistive. The difference between the pulse heights at either end of the wire reflect the position of the track. To correct for different amplifier gains, one makes a histogram of the quantity

$$PHW - PHE \times R. \tag{3.15}$$

PHE (PHW) is the pulse height at the east (west) end of the wire. The parameter R was adjusted so that the histograms were centred at zero. The position is proportional to the difference between the adjusted pulse heights. To calibrate

the calorimeter, one uses drift chamber predictions of the positions of muons and charged hadrons, and fits the pulse heights to the following expression.

$$x = m \frac{\left(PHW - PHE \times R\right)}{\left(PHW + PHE \times R\right)} \tag{3.16}$$

The standard error in x(pred) is 6.35 cm for muons, 6.1 cm for hadrons with energies above 2 GeV and 8.9 cm for hadrons with energies below 2 GeV.

The function of the calorimeter was to measure the energies of hadrons. In the steel, hadrons collided with the nuclei, creating showers of charged particles. These, in turn, were detected in the scintillator and in the EPIC's. The resulting pulse height N, in units of the most probable pulse height for a muon passing through the calorimeter, is related to the kinetic energy, T, of the incident hadron by

$$N = \frac{5.428T^2}{T + 0.721} , \tag{3.17}$$

when T is expressed in GeV. The parameterization was established for another calorimeter of similar design[50]. It assumes the hadronic showers to be completely contained. To estimate the kinetic energy of a hadron, reverse equation 3.17.

$$T = \frac{N}{2(5.428)}\left(1 + \sqrt{1 + \frac{4(5.428)(.721)}{N}}\right) \tag{3.18}$$

The resolution is given by

$$\sigma(T) = 1.1\sqrt{T} . \tag{3.19}$$

Figure 3.15 illustrates the response of the calorimeter to muons. The position of the most probable pulse height corresponds to six minimum–ionizing signals (for six calorimeter segments). According to equation 3.18, this is also the total pulse height for a hadron whose momentum is 1.6 GeV/c.

The Muon Counters

Muon identification is a special step in assembling the pieces of the charm decay puzzle. If it can be established that one of the particles leaving the primary vertex is a muon, then the event can be classified as a charged–current interaction. Once the track is tagged as that of a muon, its charge (μ^- or μ^+) reveals the incoming projectile as a neutrino or an anti–neutrino. Any muon coming from the charm–decay vertex brands the decay as semi–leptonic; the accompanying neutrino escapes detection, carrying with it information about the momentum and mass of the charmed parent particle.

As is common in high–energy physics, muons in this experiment were identified by their range in steel. Two scintillator hodoscopes punctuated an expanse of battleship–hull steel at depths (in the beam direction) of 1.2 m and 2.3 m. (These figures include the contribution of the hadron calorimeter and the lead glass.) Muons with momenta less than 1.9 GeV/c didn't reach the first bank of counters (Muon Front, or MF); muons whose momenta exceeded 3.6 GeV/c crossed the second plane (Muon Back, or MB). No other charged particles could penetrate the steel to reach MB.

If the position of a track in the muon counters, as predicted by the drift chambers, agreed with the estimate based on the muon counter data to within 2.5 standard deviations (the resolution of the muon counters was 13 cm), then the track was identifed as belonging to a muon. The front muon counters were 93% efficient; the back counters were 97% efficient.

Chapter 4

Analysis

The spectrometer described in the previous chapter was operated in the wide–band neutrino beam at Fermilab for six and a half months, from mid–November of 1980 until the end of May, 1981. The data gathered by the electronic detectors were recorded on magnetic tapes using an Eclipse 2000 computer. Neutrino interactions were located in the fiducial volume of the emulsion using the 'follow–back' technique, which is described below; the 'scan–back' and 'volume–scan' techniques, also described below, were employed to find the D^0 decay vertices. In this manner, the decay candidates were found independently of their positions in the emulsion along the beam direction, and independently of their decay lengths.

There followed an exhaustive examination of each decay candidate. The emulsion scanners measured the slopes of the decaying particles, and the slopes of the tracks coming from primary and secondary vertices. Tracks in the target were matched with those reconstructed in the drift chambers. Whenever possible, particles were identified using the TOF system, the calorimeters, the muon counters, or ionization measurements in the emulsion. Neutral hadrons were detected using the calorimeters.

For each decay candidate, there were several hypotheses consistent with momentum and baryon conservation. All were examined using an hypothesis–testing programme, and in each case the one with the smallest χ^2 was chosen.

From these choices, as pure a sample of D^0's as possible was established, using the strategies described in this section. The final sample comprised 39 D^0's, including 26 two–pronged decays (V's) and 13 four–pronged decays. It further

included three semi–leptonic decays, and four examples of the $D^{*+} \rightarrow D^0\pi^+$ reaction. Also described in this chapter are the techniques used to determine the effects of features of the analysis algorithm which could distort the final result, and of reactions which could contaminate the sample. The final result, the most probable mean lifetime, was estimated using the Maximum Likelihood method.

Scanning

The first stage of the analysis was a search for the neutrino interactions and for the charmed–particle decays. The emulsion scanners first followed back, into the emulsion, tracks that had been reconstructed in the drift chambers and which were predicted to have emerged from vertices within the target. The track reconstruction programme, written and implemented at The Ohio State University, typically yielded a few (one or two) high–momentum tracks; one of these was usually the muon from the neutrino interaction and the remaining tracks were produced either by other particles leaving the primary vertex, or by the products of a secondary interaction or a decay. The so–called 'follow–back' (FB) technique was very effective; of 420 tracks found on the fiducial sheet, which were expected to point to vertices, 412 were in fact followed to vertices, an efficiency (η_{FB}) of $.981 \pm .007$. The associated uncertainty is simply the standard deviation of a binomial distribution.

$$\sigma = \sqrt{\frac{\eta(1-\eta)}{N}} = .007 \tag{4.1}$$

Once a vertex had been found, the search for charm decays was begun. Both neutral– and charged–particle decays were sought using the scan–back (SB) approach (described below). Two additional techniques were employed to augment this approach; volume–scan (VS) in the case of neutral–particle decays and follow–down (FD) in the case of charged–particle decays. Since this thesis is con-

cerned only with neutral decays, the FD process will not be discussed here. Details can be found in references 46, 47 and 51.

Volume–scanning was used near the decay vertices. The group at Nagoya University scanned a cylindrical region 1000 μm long with a radius of 200 μm. Other groups scanned a conical volume. The efficiency of the VS technique was estimated from knowledge of the number of photons expected to convert within the scanning region, and the number of conversions observed.

$$\eta_{VS} = \frac{pairs\ found}{pairs\ expected} \tag{4.2}$$

As an example, with the VS approach, the Nagoya group found 47 pairs. The expected number was calculated as follows. There are approximately two π^0's, and hence four γ's produced in each charged–current neutrino interaction[47]. The number of photons expected to convert over the scanning distance of 1.00 mm is thus

$$npairs = 4 \times evt \times (1 - e^{-1.06/41.5}) = 160 \pm 4\ . \tag{4.3}$$

The conversion length (41.5 mm) is 9/7 of a radiation length, and there were 1583 events examined for conversions (evt). The volume–scanning efficiency for the Nagoya group is then

$$\eta_{VS} = 47/npairs = .29 \pm .04\ . \tag{4.4}$$

The efficiency thus estimated is an over–estimate of the efficiency for finding neutral decays. This is because the tracks from a conversion initially lie one on top of the other, and appear to be darker, approximately twice–minimum–ionizing tracks. They are consequently easier to see than are the more divergent tracks from decays, which are mainly minimum–ionizing tracks.

Those decays very close to primary vertices present a special problem. In this region, tracks from a decay may become confused with primary tracks, so that it is difficult even to establish that there is a decay. The diameter of the region is a function of the number of heavily ionizing tracks (NH) from nuclear breakup, and of the number of 'shower', or minimum–ionizing tracks (NS). The form of the relation was estimated by measuring the diameters of 320 neutrino interaction regions, taken at random from the data of the first run of E531.

$$D(\mu m) = (NH + \frac{NS}{2})/4 + 1.8 \tag{4.5}$$

The shortest decay length amongst the second–run neutral decay candidates was 15.3 μm, outside the 'region of confusion'.

Scan–back was the principal strategy used to find the charm–decay vertices. After the primary vertices had been found using FB, the tracks emerging from it were matched with tracks reconstructed in the drift chambers. The SB technique involved following back into the emulsion the remaining tracks in the chambers whose momenta exceeded 400 MeV/c and whose slopes with respect to the beam axis were less than 300 mr. These tracks led to nuclear interactions, photon conversions, strange–particle decays and charmed–particle decays.

Scan–back comprised three separate operations: reconstructing a track in the drift chambers, finding that track on the fiducial sheet and following the track from the sheet to a vertex. The latter is simply the follow–back process described earlier. To estimate how readily tracks in the chambers were located on the changeable sheet is straightforward. Of 148 good tracks reconstructed in the chambers which were also identified with tracks in the emulsion modules, 142 were found on the sheet; the efficiency (η_{CS}) is $.959 \pm .016$. Both η_{CS} and η_{FB} were estimated directly by the scanning group at Nagoya University. The corresponding efficiencies

of the other groups were calculated using equation 4.6,

$$(\eta_{CS}\eta_{FB})_G = (\eta_{CS}\eta_{FB})_{NGY}\left(\frac{\text{np found}}{\text{np searched}}\right)_G\left(\frac{\text{np searched}}{\text{np found}}\right)_{NGY} \tag{4.6}$$

where 'NGY' refers to the Nagoya group, 'G' refers to any other scanning group, 'np found' is the number of photon conversions found using SB and 'np searched' is the number of conversions sought.

The efficiency of reconstructing a track in the drift chambers (η_{DC}) was calculated after the charmed decay search had been completed. Each event was examined to determine which decay tracks satisfied the scan–back criteria. In some events, none of the tracks met the criteria, in others, all of them did. Those events in the former category were found using volume–scanning. If one were to use SB exclusively, one would not know how many such events (N_0) there were. Thus, the first 'unknown' was N_0. Also unknown was η_{DC}. Finally, the total number (N) of charm decays was 'unknown', but was constrained to be the sum of the the N_m's, where N_m is the number of charm decays with m tracks meeting the SB criteria. The equations to be solved were

$$N_m = N({}_nC_m){\eta_{DC}}^m(1-\eta_{DC})^{n-m} \tag{4.7}$$

where n is the number of prongs and ${}_nC_m$ is the binomial coefficient. For each n, the equation of constraint is

$$N = \sum_{m=0}^{n} N_m \ . \tag{4.8}$$

In the simple case of a V, where n is 2, equations 4.7 and 4.8 reduce to

$$\begin{aligned} N_0^V &= N^V(1-\eta_{DC}^V)^2 \\ N_1^V &= 2N^V\eta_{DC}^V(1-\eta_{DC}^V) \\ N_2^V &= N^V\eta_{DC}^2 \\ N^V &= N_0^V + N_1^V + N_2^V \ . \end{aligned} \tag{4.9}$$

There were a total of 40 V's in the second run sample; 5 events, found with volume–scanning, had no tracks satisfying the criteria, 13 events each had one acceptable track, and in 22 events both tracks were acceptable.

$$N_1 = 13$$
$$N_2 = 22 \tag{4.10}$$

Substitution of equation 4.10 into equation 4.9 produced this result:

$$\eta_{DC}^{V} = 0.77 \pm 0.06$$
$$N_0^V = 2 \pm 1 \tag{4.11}$$
$$N^V = 37 \pm 1 \ .$$

The values calculated for N_0^V and N^V are consistent with the values obtained by using both SB and VS.

The results of a graphical analysis of the equations associated with four–pronged decays in the second run are listed in equation 4.12.

$$\eta_{DC}^{4p} = 0.51 \pm 0.09$$
$$N_0^{4p} = 1.0 \pm 2.0 \tag{4.12}$$
$$N^{4p} = 17.5 \pm 2.0$$

Each of the 14 observed four–pronged events had at least one track that satisfied the SB criteria; this agrees with equation 4.12.

In addition to the V's and straightforward four–pronged decays, there was one event in which one of the tracks interacted in the emulsion and produced two forward–moving tracks. All five of the tracks met the scanning criteria, yet only two were found in the chambers; the efficiency in this case was 0.4±.2. The net efficiency for reconstructing tracks from four–pronged decays is the average of these two values, weighted with the number of events of each type:

$$\eta_{net}^{4p} = \left(\frac{14\eta_{DC}^{4p} + \eta_{DC}^{5p}}{14+1} \right) = .50 \pm .08 \ . \tag{4.13}$$

To recapitulate, any track from a V was reconstructed in the drift chambers with an efficiency of (77±9)%, and any track from a four–pronged decay was reconstructed with an efficiency of (50±10)%.

The efficiency with which the scan–back technique, applied to a single track, led to a vertex is the product of the efficiencies of its sub–processes. Thus, when η_{FB} represents the follow–back efficiency and η_{CS} the efficiency for finding tracks on the changeable sheet,

$$\begin{aligned} \eta_{SB}^{V} &= \eta_{DC}^{V}\eta_{CS}\eta_{FB} \ = 0.72 \pm .09 \\ \eta_{SB}^{4p} &= \eta_{DC}^{4p}\eta_{CS}\eta_{FB} = 0.47 \pm .08 \ . \end{aligned} \tag{4.14}$$

Since each V (four–pronged event) has two (four) tracks, V's (four–pronged events) are found by SB with an efficiency given by equation 4.15.

$$\begin{aligned} \eta_V &= 1 - (1 - \eta_{SB}^{V})^2 = 0.92 \pm .05 \\ \eta_{4p} &= 1 - (1 - \eta_{SB}^{4p})^4 = 0.92 \pm .05 \end{aligned} \tag{4.15}$$

The probability of finding a neutral decay with SB is the average of η_V and η_{4p} weighted with the relative production rates of V's and four–pronged events in neutrino interactions. The MARK II collaboration[52] found that V's are produced (63.0±5.4)% of the time, and that four–pronged events are produced (22.2±4.7)% of the time. Consequently, neutral decays were found by the scan–back strategy with an efficiency of .92±.04.

The net efficiency for finding neutral decays in a region in which both scanning methods were used is given by

$$\eta_{net} = 1 - (1 - \eta_{SB})(1 - \eta_{VS}) \ . \tag{4.16}$$

For example, the Nagoya group's VS efficiency was .29 ±.04; the net efficiency was .95 ±.03. The net efficiencies of the other groups are listed in Table 2.

Table 2.

Group Code	From (μm)	To (μm)	Efficiency
KH	0.0	3.0	0.0
	3.0	10.0	0.50
	10.0	300.0	0.67
	300.0	50000.0	0.62
NV	0.0	15.0	0.0
	15.0	30.0	0.71
	30.0	1000.0	0.95
	1000.0	50000.0	0.92
O3	0.0	3.0	0.0
	3.0	10.0	0.63
	10.0	300.0	0.84
	300.0	50000.0	0.81
ON	0.0	15.0	0.0
	15.0	30.0	0.74
	30.0	1000.0	0.98
	1000.0	50000.0	0.97

Scanning Efficiencies

The important features of the scan–back technique are that it is independent of decay length and that it is independent of the position of the interaction, along the beam direction, in the target. The first point is illustrated by figure 4.1. This is a graph of the ratio of the number of conversions found to the number expected, as a function of conversion length. That η_{SB} is independent of the vertex position

is shown by figure 4.2; it depicts the efficiency with which neutrino interactions are found using FB, as a function of vertex position. This efficiency is essentially uniform.

Event Reconstruction

Two programmes were used to reconstruct the tracks of charged particles in the drift chambers. One was written and implemented at The Ohio State University. The other, a complementary programme, developed at the the University of Toronto and at McGill University, used both automatic and interactive track–fitting techniques. In its interactive mode, the latter programme displayed a schematic picture of the spectrometer on a terminal screen (fig. 3.9), so that it was possible to view the apparatus from different angles. The programme indicated on the display the locations of the drift chamber wires that had been hit by charged particles, and it also showed the positions of TOF counters, calorimeter EPIC's, and muon counters that had been struck. Using the automatic mode of the Toronto programme, first the tracks in the downstream chambers were reconstructed, and then the upstream tracks were reconstructed using the interactive mode. The downstream chambers tended to have significantly fewer signals, so that there were fewer combinations of hits that constituted reasonable candidates for tracks. Consequently, the programme could quickly find and display these combinations.

To guide the interactive search for an upstream track, the programme drew a 'road' on the terminal screen. A road was a projection, through the spectrometer, of a track already found in the emulsion. The curvature of the projection was determined by the momentum estimated by the OSU programme, and the slopes of the projection were those measured in the emulsion. In the case of a spectrom-

eter track not associated with an emulsion track, the projection used the slopes determined by the OSU programme.

Two techniques were employed to fit an upstream track. In the first case, using manually–selected hits closest to the projection in two stereo views, the programme projected the resulting segment into the third view, added hits from that view closest to the projection and attempted to fit a track composed of hits from all three views. This was repeated for each of three pairs of views. The second technique entailed the fitting of hits that had been manually selected from all three views. In both cases, the programme was allowed to drop hits from the initial list, and to add hits, in order to decrease the χ^2 per degree of freedom. An acceptable upstream fit had a χ^2 per degree of freedom less than 5.0, and had no less than ten hits (out of fifteen upstream chambers).

To complete the process of reconstuction, each upstream segment was joined to all downstream segments that appeared to be continuations of it. The segments were joined using a quintic spline; the five parameters were the slopes and x and y co–ordinates at the origin of the co–ordinate system, and the inverse of the momentum. Tracks retained by the programme had at least fifteen hits (out of 24 chambers) and a χ^2 per degree of freedom less than 5.0. Generally, there were several similar candidates for each track. The candidates selected were those which had the most hits, the lowest χ^2 per degree of freedom, and whose slopes best matched the slopes of the emulsion tracks.

If the slopes of a track reconstructed in the drift chambers and the slopes of a track found in the emulsion differed by amounts which could be explained by multiple Coulomb scattering in the emulsion, then the tracks were defined to be matched. In some cases both the exit slopes, measured at the downstream face of the target, and the decay vertex slopes were measured. In others, only the decay

vertex slopes were measured. The first case had the benefit that the two sets of slopes – drift chamber and emulsion – were measured at points in close proximity. Consequently, the effects of multiple scattering in the emulsion had little bearing on the matches. In practice, the exit slopes were measured less precisely than were the decay slopes, by about a factor of two (figures 4.3a through 4.3f).

After the drift chamber data had been condensed into a list of tracks and momenta, the work of identifying the charged particles began. Some particles could be identified in the emulsion. A converting photon produces an e^+e^- pair whose tracks, before separating, are indistinguishable from a single twice–minimum–ionizing particle – a distinctive signature. Ten pairs were found in the neutral–decay sample. The momenta of the leptons, measured in the drift chambers, were corrected for the effects of bremßtrahlung (see later).

Six charged tracks (other than those of e^+e^- pairs) stopped in the emulsion, and 26 more were not matched to tracks in the drift chambers, out of a total of 242 tracks in the neutral sample. It was sometimes possible to identify the particles using measurements of $p\beta$ and ionization. The former were derived from the rms scattering angles, the latter from the tracks' grain densities.

In the sample of 39 decay candidates, there were 104 decay tracks in the emulsion that were matched with drift chamber tracks. There were 37 primary muons identified with the muon counters; 35 muons hit both the front and back counters, and 2, with momenta less than 3.6 GeV/c, hit only the front counters. The two events without identified muons could have been neutral–current reactions, and so need not be interpreted as evidence of muon–counter inefficiency. Three events were semi–muonic decays. In one case, the secondary muon hit the front and back counters. In the other two instances, the secondary muons, whose momenta were less than 3.6 GeV/c, struck only the front counters.

Each reconstructed track was projected from the chambers into the plane of the TOF II hodoscope, and was associated with a paddle that had been hit. To be of use, the TOF II data were required to satisfy three criteria. First, the prediction of the y position of a track in the TOF paddle had to agree with the estimate derived from an extrapolation of the track from the chambers. (Hodoscope position measurements had a precision of approximately 2.0 cm.) The second condition was that the total energy deposited in the scintillator be consistent with the average energy lost by one minimum–ionizing particle. This criterion was necessary since it was not possible to calibrate the TOF system *in situ* well enough to reliably separate the effects of two particles hitting the same paddle. The final criterion was that there be no other track segment in the downstream chambers pointing to the paddle in question. (This could have been the downstream segment of a track that had not been fully reconstructed, or it could have been the track of a particle emitted in the upstream direction from a shower in the electromagnetic calorimeter, which abutted the TOF hodoscope.) If a particle had been identified as a muon with the muon counters, or as an electron coming from a conversion in the emulsion, or if it had a momentum greater than 10 GeV/c, then it was used to improve the estimate of the event's start time, as described in the section dealing with the calibration of the TOF system. Protons, kaons and pions were distinguished as previously described. Hypotheses whose TOF confidence levels were less than five per cent were not considered any further. Twenty–five of the 101 non–muonic decay tracks were identified by TOF and in 23 more cases one hypothesis could be rejected.

When as many charged particles as possible had been identified as hadrons, muons or electrons, it remained to associate with them the energy deposited in the calorimeters; extra energy implied the presence of neutral particles. In the lead glass system, a muon signal was typified by a triple coincidence of EPIC wires (fig.

4.4) and an energy of 400 MeV in the lead glass block behind the intersection. The system responded similarly to hadrons, but, since hadrons could initiate showers in the .7 interaction lengths of lead glass, the energy that they deposited was sometimes significantly greater than 400 MeV. In practice, a value of not greater than 1/3 of the particle's momentum was held to be consistent with the energy lost by a single hadron.

In contrast to hadrons, electrons almost always lost all their energy in the lead glass. Any charged track which exhibited this behaviour was probably that of an electron. Electrons also radiate bremßtrahlung photons. For purposes of shower reconstruction, it was assumed that all such radiation was emitted as a single photon while the electron was in the emulsion, which had a much shorter radiation length (X_0) than the drift chambers. A Monte Carlo programme was used to estimate the uncertainty associated with this assumption. The energy of the electron before radiating, E_i, was calculated from

$$E_i = pe^{X/X_0} \tag{4.17}$$

where p is the momentum of the electron after travelling a distance along the beam direction X in the emulsion. The energy radiated, E_B, is then

$$\begin{aligned} E_B &= E_i - E_f \\ &= E_f(e^{X/X_0} - 1) \ . \end{aligned} \tag{4.18}$$

The associated uncertainty is given by

$$\sigma(E_i) = \sqrt{\left(e^{X/X_0}\right)^2\sigma(p)^2 + \left((p/X_0)e^{X/X_0}\right)^2\sigma(X)^2 + c^2} \ . \tag{4.19}$$

The value of 'c' was determined by the Monte Carlo programme.

After account had been taken of all the energy in the lead glass system associated with the charged tracks, what remained was used to reconstruct showers.

If there was only one triple coincidence of EPIC wires, or if there were several in close proximity, only one photon was reconstructed. In these cases, the total energy in the shower was the sum of the energies recorded by the three EPIC wires and the lead glass block behind them. If there were two clearly separated shower candidates in the same block (fig.4.6), the energy in that block was apportioned in ratio evinced by the EPIC pulse heights. For example, if E_i is the energy of the ith shower in the block,

$$\begin{aligned} \frac{E_1}{E_2} &= \frac{E_{1(EPIC)}}{E_{2(EPIC)}} \\ E_1 + E_2 &= E_{block} \\ E_2 &= \frac{E_{block}}{1 + E_{1(EPIC)}/E_{2(EPIC)}} \ . \end{aligned} \tag{4.20}$$

In the case of a shower candidate not accompanied by a triple coincidence of EPIC wires (a 'block–only' shower), the photon was assumed to be in the centre of the block. Any shower in a block not contiguous with other blocks that contained showers, and whose energy was less than 100 MeV, was discarded.

Invariant masses of photon pairs were calculated to establish neutral pion candidates. If any of the masses differred from the pion mass by more than three standard deviations, the candidate was discarded.

After the data from the electromagnetic calorimeter had been scrutinized, data from the hadron calorimeter were examined for indications of the presence of neutrons and K_L^0's. Charged tracks were associated with signals in the calorimeter EPIC's, and to a less precise degree with those in the scintillators. The total energy in the calorimeter was compared to the energy expected from all the charged tracks, as estimated from the momenta measured in the drift chambers, and the energy associated with each track was compared to the value expected for that track. A surfeit of energy associated with a track, or a significant signal that

was clearly separated spatially from the charged tracks, constituted evidence for a neutral hadron.

Kinematic Analysis

At this point, the raw ingredients of pulse heights and grain counts had been distilled into a mixture of momenta, slopes and particle identities. The next step was to ascertain which of the events could reasonably be ascribed to the decay of a D^0. In other words, how likely is it that a set of particles emerging from a vertex were the products of a D^0 decay? An hypothesis testing programme, based on an algorithm using Lagrange multipliers[53] for constrained kinematic fitting, selected a set of momenta and slopes that minimized χ^2 and ensured that the four equations of energy and momentum conservation were satisfied at each decay vertex. If there were fewer unknowns than equations, then the system was over–determined and the equations were solved iteratively. The iteration process ended when the x and y constraints were satisfied to within 1.0 MeV/c, the z constraint to within 10.0 MeV/c, the energy constraint to within 10.0 MeV, and the reduced χ^2 had changed by less than 0.1 from the previous iteration. The probability of a given hypothesis was then estimated.

Initially, the programme was executed in a mode that determined the mass of the weakly–decaying parent. If the fitted mass was sufficiently close to the accepted D^0 mass, then the programme was re–executed in a mode which constrained the parent mass to be 1.8647 GeV/c^2. All expected decay hypotheses consistent with the TOF data and baryon conservation were examined.

The salient results of the fitting procedure were the lifetime and momentum of the parent, and a confidence level associated with each hypothesis. At times, no acceptable (CL$>$ .01) hypotheses were to be found. In such instances, the zero

constraint (0–C) solutions were examined. In general, if it is assumed that there is a single undetected neutral particle in an event, then the mass of the parent is a quadratic function of the parent momentum. (The quadratic coefficients are functions of the masses of the parent and the missing neutral, and of the masses and measured slopes and momenta of the secondaries.) For a given choice of neutral and parent mass, there are two solutions for the parent momentum and lifetime. Each solution yields a prediction of the missing neutral particle's trajectory. When the path lay outside the acceptance of the spectrometer, the 0–C solution was retained. When the path lay inside the acceptance, and no evidence for the neutral's passage was extant, the solution was discarded, unless the assumed missing neutral was a neutrino.

Lifetime calculation

The maximum likelihood method[54] was used to reduce the individual measurements of proper times to the best estimate of the D^0 lifetime. The likelihood function, $\mathcal{L}(x)$, is given in equation 4.21. It represents the probability of making n measurements of a quantity, with values y_i which are distributed according to a probability distribution function (*pdf*) dependent upon a single parameter x.

$$\mathcal{L}(x) = \prod_{i=1}^{n} pdf(y_i, x) \tag{4.21}$$

In particular, if the measured quantities are proper decay times, then $\mathcal{L}(\tau)$ will have its maximum value when τ is the most likely estimate of the mean lifetime.

Assuming that all decay time measurements are equally likely, the distribution function is

$$pdf(t_i, \tau) = \frac{1}{\tau} e^{-t_i/\tau} \ . \tag{4.22}$$

If the detection efficiency, ϵ_i, is a function of the observed decay length l_i, then the distribution function is

$$\begin{aligned} pdf(t_i,\tau) &= \frac{1}{\tau}\frac{\epsilon(l_i)e^{-t_i/\tau}}{A(p_i,\tau)} \\ A(P_i,\tau) &= \int_0^T \frac{1}{\tau}\epsilon(l_i)e^{-t'/\tau}dt' \\ l_i &= \gamma_i\beta_i c t_i \\ &= (\frac{p}{m})_i c t_i \ . \end{aligned} \tag{4.23}$$

The normalization factor $A(p_i,\tau)$ ensures that the probability of observing any t_i with values between 0 and the longest measureable time T is unity.

The logarithm of $\mathcal{L}$ also has its maximum value, $ln(\mathcal{L}_{max})$, when τ is the most probable lifetime of the sample (fig. 4.7b). The standard error ('1 σ') in τ may be estimated from the values of τ for which

$$ln(\mathcal{L}) = ln(\mathcal{L}_{max}) \pm 0.5 \ . \tag{4.24}$$

The 95.4% confidence ('2 σ') limits were calulated by determining the values of τ such that

$$ln(\mathcal{L}) = ln(\mathcal{L}_{max}) \pm 2.0 \ . \tag{4.25}$$

The lifetime was deduced from a parabolic interpolation of the likelihood curve near the maximum $ln(\mathcal{L}_{max})$. The standard error was calculated using a linear interpolation near $ln(\mathcal{L}_{max}) \pm 0.5$.

Within the fiducial volume of the target, there were 39 D^0 candidates. Figure 4.7a displays a graph of dN/dt as a function of time. The slope of the line was determined with the maximum likelihood method, and the numbers of decaying particles were weighted with the scanning efficiencies. The most probable mean lifetime is

$$\tau(D^0) = (4.8^{+0.9}_{-0.7}) \times 10^{-13}\mathrm{s} \ , \tag{4.25a}$$

and the '2 σ' intervals are $+2.0$ and -1.3×10^{-13} sec.

Discussion

Since these data were collected in the second run of E531, it is permissible to combine the two sets of data to yield a single estimate of $\tau(D^0)$. The result is[55]

$$\tau(D^0) = 4.3^{+0.7+0.1}_{-0.5-0.2} \times 10^{-13}\text{sec.} \tag{4.25b}$$

This value, and the values obtained by other groups[59,60], are displayed in figure 4.13. The estimates are consistent, and have an average value of $(4.35 \pm 0.32) \times 10^{-13}$ s.

The uncertainty of equation 4.25a reflects the indeterminacy associated with the fact that a small number of decay times were drawn from an exponential distribution. This error can be alternatively estimated by simulating with a computer programme the process of choosing samples of decay times from an exponential distribution. One hundred samples, of 39 proper times each, were selected from a population whose mean lifetime was 4.9×10^{-13}s. The most likely lifetime was calculated using the same programme used to analyze the experimental data; the result was $(4.90 \pm .08) \times 10^{-13}$s, and the rms width of the distribution was $(0.78 \pm .06) \times 10^{-13}$s. From this exercise two conclusions can be drawn: first, that the maximum likelihood technique neither over– nor under–estimates significantly the most probable lifetime; and second, that the uncertainty is dominated by statistical fluctuations in the small samples. The latter is supported by the similarity of the uncertainties derived from the Monte Carlo and Maximum Likelihood approaches.

In what follows, it is argued that each event in the sample is a decay of a D^0 meson, and not one of the reactions which might mimic this process. The first

such reaction is the decay of a strange particle (either a K_s^0 or a Λ^0 baryon). In the emulsion, their decays look like the two–charged–body decay modes of the D^0. The charmed and strange particles can be distinguished by their masses. One can, in addition, estimate the number of K_s^0 and Λ^0 decays expected to be observed in the emulsion, and compare it with the number actually observed. In this experiment, there were 12 strange–particle decays found with the 'scan–back' method (see the previous section). In only one case did both tracks meet the 'scan–back' criteria. Using the method described in the previous section, we estimated the efficiency with which the tracks from strange V's were reconstructed in the drift chambers.

$$\begin{aligned} N_0 &= N(1-\eta_{DC})^2 \\ N_1 &= 2N\eta_{DC}(1-\eta_{DC}) = 11 \\ N_2 &= N\eta_{DC}^2 = 1 \end{aligned} \tag{4.26}$$

The solution is that there were probably 44 strange V's in the emulsion; their tracks were reconstructed with an efficiency of 0.15. Accordingly, the efficiency for finding a strange V is

$$\begin{aligned} \eta_V &= 1-(1-\eta_{DC}\eta_{CS}\eta_{FB})^2 \\ &= .27\ . \end{aligned} \tag{4.27}$$

This is a crude estimate, because N_2 is so small and because η_{DC} is so sensitive to it. However, because N_2 is so small, it is apparent that strange V's are not found efficiently. A Monte Carlo calculation[55] yielded an efficiency of .3. Thus, approximately 40–44 K_s^0's and Λ^0's decayed to charged particles in the target.

This estimate is consistent with what one would expect based on the results in reference 56. The authors determined the ratio of the visible V cross–section to the total charged–current cross–section as a function of the invariant mass, W, of the hadrons in the final state. In the first run of E531[45], when the energy of

the protons in the main ring was 350 GeV, the average value of W was about 5.0 GeV/c^2. Hence

$$\frac{\sigma_V}{\sigma_{cc}} \approx .1 \ . \tag{4.28}$$

The momentum spectrum of the observed K^0's and Λ^0's in this experiment was such that

$$\begin{aligned} \langle \gamma\beta c\tau_K \rangle_K &= 14.9 \text{ cm} \\ \langle \gamma\beta c\tau_\Lambda \rangle_\Lambda &= 19.2 \text{ cm} \ . \end{aligned} \tag{4.29}$$

Since there were nearly as many K's as Λ's (4 K's, 6 Λ's and 2 indistinguishable cases)

$$\langle \gamma\beta c\tau \rangle \approx 17 \text{ cm} \ . \tag{4.30}$$

This value was determined using only those K's and Λ's which decayed in the emulsion; the average for all strange particles should be higher. Consequently, an upper limit on the fraction expected to decay in the target is

$$f \leq 1 - e^{-2.5/17} \approx .14 \ . \tag{4.31}$$

(The average distance travelled by a particle before leaving the target is half the depth of the emulsion.) The expected number of visible V's (N_V) is then

$$\begin{aligned} N_V &< N_{int}\frac{\sigma_V}{\sigma_{cc}} f \\ N_{int} &= 2638 \\ N_V &< (2638)(.1)(.14) \approx 37 \end{aligned} \tag{4.32}$$

where N_{int} is the number of charged–current interactions (2638). This is consistent with the previous estimate.

If, despite the above arguments, there were strange particles in the sample of decay candidates, then a mean lifetime calculated without any V's (except those which come from D^{*+} decays – see later) might differ significantly from the original

estimate. In the sample, there were 13 4–pronged decays and two V's from D^{*+} decays; their mean lifetime is $5.2\ ^{+1.7}_{-1.2} \times 10^{-13}$s.

The conclusion is that, since the number of visible strange V's is consistent with expectations, and since the mean lifetime of a sample of events which excludes any possible strange particles is not significantly different from the lifetime of the complete sample, there is no good reason to suspect that any of the V's in the D^0 sample are really strange–particle decays.

Another reaction which can masquerade as the decay of a D^0 is the decay of a massive, long–lived neutral baryon other than the Λ^0. For instance, the A^+ has a mass[20] of 2460 MeV/c^2, and the neutral member of the isospin doublet is expected to have a similar mass. Whenever a charged decay product is consistent with the proton hypothesis, the baryon decay *ansatz* must be considered. Of the 26 constrained events in our data set that were consistent with the D^0 hypothesis, 13 were also consistent with baryon decay hypotheses. The mean lifetime was calculated without these events; the result was $5.2^{+1.9}_{-1.4} \times 10^{-13}$s.

A weakly–decaying neutral baryon might produce, as one of its decay products, a Σ^+ or a Σ^-. Each of these particles decays to one charged particle and one neutral particle.

$$\begin{aligned} \Sigma^+ &\longrightarrow p\pi^0 \\ \Sigma^+ &\longrightarrow n\pi^+ \\ \Sigma^- &\longrightarrow n\pi^- \end{aligned} \tag{4.34}$$

The transverse momentum of the charged tertiary particle (p or $\pi^\pm$) with respect to the direction of the Σ is approximately 190 MeV/c, so that if the Σ decays in the emulsion, the final particle will leave the target with an angle significantly different from the angle of the Σ at the charm decay vertex. No instances of this were found. In each case in which an emulsion track from a decay was matched

with a drift chamber track, the difference between the angle measured at the vertex by the emulsion scanners and the angle of the reconstructed track was consistent with multiple Coulomb scattering.

Neutral baryons in the sample of D^0 candidates might be revealed by a clustering of fitted masses about the baryon mass. To investigate this possibility, a Gaussian ideogram was generated.

$$F_B(m_0) = \sqrt{\frac{1}{2\pi}} \sum_{j=1}^{13} \frac{1}{n_j} \sum_{i=1}^{n_j} \frac{1}{\sigma_{ij}} e^{-.5(m_{ij}-m_0/\sigma_{ij})^2} \tag{4.33}$$

The double sum extended over the 13 events which were consistent with the baryon–decay hypothesis, and over all such hypotheses. The quantities m_{ij}, σ_{ij} and n_j are, respectively, the fitted mass and uncertainty of the ith hypothesis, and the number of hypotheses in the jth event. It can be seen from figure 4.8 that there is no clustering of fitted masses. The 13 baryon candidates thus evince neither a mean lifetime significantly different from the D^0 lifetime, nor a clustering of fitted masses, nor is there any evidence of Σ decay. There is therefore no suggestion of baryon decays in the sample of D^0 candidates.

In addition to the decays of strange particles and long–lived baryons, there is another reaction which might be mistaken for the decay of a D^0: the nuclear interaction of a neutral hadron in the emulsion. The number of such interactions expected to appear amongst the decays in the ith scanning region is the product of four factors:

- the average number of neutral hadrons produced in charged–current neutrino interactions (N_{had});

- the probability that such hadrons will interact and produce even numbers of charged secondaries without evidence of nuclear recoil – that is, no short, dark tracks near the vertices ($P_{NH=0}$);

- the probability of interaction in the ith region ($P_{int}(Z_i)$).

- the scanning efficiency in the ith region ($\epsilon(Z_i)$);

$$N_{int} = N_{had} P_{NH=0} \sum_i \epsilon(Z_i) P_{int}(Z_i) \tag{4.35}$$

On average, there are 0.7 proton and 4.3 charged meson tracks, 0.15 K^0's and 0.05 Λ^0's produced per charged–current interaction[47,57]. One would expect, conservatively, there to be as many neutrons produced as protons, so that there are 0.9 'stable' neutral hadrons per charged–current interaction. Neutral hadronic interactions have the topology of a neutral decay 4.7% of the time[58]. The probability of interaction at a distance Z_i from the neutrino vertex ($Z_i^{Low} < Z_i < Z_i^{High}$) is given by

$$P_{int}(Z_i) = e^{-Z_i^{Low}/\lambda} - e^{-Z_i^{High}/\lambda} \tag{4.36}$$

where λ is the interaction length, and Z_i^{High} and Z_i^{Low} are the boundaries of ith region. The interaction length is used instead of the absorption length, which is twice as large, to take account of elastic scattering which can also mimic neutral decays. Finally, the scanning efficiencies are listed in Table 2 (p. 54).

In the 2638 interactions recorded, approximately .6 hadronic interactions would present the topology of a D^0 decay. Since the nuclear interaction length of the emulsion was 351 mm, there is only a 4% chance that one of these interactions would occur within 5 mm of the primary vertex. All of the D^0 candidates appeared in this region, so that it is very unlikely that any of them were nuclear interactions.

In addition to being influenced by background events, the most probable lifetime can also be affected by artifices of the analysis. The first example is the

manner in which the 13 0–C events (Appendix 3) were treated. In each of those cases, it was assumed that only one neutral particle escaped detection, and its momentum was calculated using the constraints of energy and momentum conservation. The mass of the parent is a quadratic function of 'missing momentum', and there were in general two solutions for the momentum for each parent mass (fig. 4.9). The average of the solutions, when the parent mass was equal to the D^0 mass, was used in the calculation of the mean lifetime. (Once, one of the two solutions was discarded because the neutral particle posited should have been, but was not, detected by either the electromagnetic or the hadronic calorimeter.) A mean lifetime was calculated using the 26 constrained decay hypotheses; the result was $4.4\ ^{+1.0}_{-.8} \times 10^{-13}$s. Extreme estimates of the mean lifetime were obtained from the sample of 39 events using all the high '0–C' solutions, and then using all the solutions with low lifetimes. Less insouciant techniques would produce estimates of the mean lifetime closer to the naïve original estimate. Since the two extreme values, $5.0^{+.9}_{-.7} \times 10^{-13}$s and $4.7^{+.9}_{-.7} \times 10^{-13}$s, differ insignificantly from the first estimate of 4.8×10^{-13}s, a more sophisticated approach is unwarranted.

Another uncertainty in the estimate of the mean lifetime is the uncertainty associated with the scanning efficiencies. As indicated above, D^0 candidates were located independently of their decay lengths, l. If, for some reason, this were not true, then the estimate of τ would be wrong. This matter was addressed by noting the effect on τ of using efficiencies strongly dependent on decay length. The efficiencies in Table 2 were replaced by the functions

$$\epsilon(l) = \begin{cases} -.0001 \cdot l(\mu m) + 1.0 & l \leq 5mm \\ 0.5 & l > 5mm \end{cases}$$

and

$$\epsilon(l) = \begin{cases} .0001 \cdot l(\mu m) + 0.5 & l \leq 5mm \\ 1.0 & l > 5mm\ . \end{cases} \tag{4.37}$$

The parameters in equation 4.37 were chosen because they represent large, and unlikely, deviations from a uniform scanning efficiency.

With the efficiency functions in equation 4.37, the most probable lifetimes are $5.4^{+1.1}_{-0.9} \times 10^{-13}$s and $4.2^{+0.7}_{-0.6} \times 10^{-13}$s. Both of these are consistent with the original estimate of 4.8×10^{-13}s. Since it is unlikely that the scanning efficiency is less uniform than postulated here, any real bias would not significantly affect the estimate of the mean lifetime.

The estimate of the mean lifetime can also be affected by the method used for choosing the decay hypotheses. In each constrained event, the hypothesis with the highest confidence level was chosen. When there are other acceptable hypotheses (C.L. $>$ .01), this procedure is expected to select the wrong hypothesis occaisionally. One consequence of this is that the number of Cabibbo–suppressed reactions might appear to be too high. Of the 26 constrained decays in this experiment (Appendix 2), 15 were Cabibbo–favoured, 7 were Cabibbo–suppressed and 4 were ambiguous. (Three of these involved K_L^0's. In the fourth event no primary muon was identified, so that it wasn't clear whether the parent was a D^0 or a $\overline{D}^0$.) This result is inconsistent with the naïve view that Cabibbo–favoured decays should outnumber Cabibbo–suppressed decays by a factor of about 20.

However, 4 of the 7 Cabibbo–suppressed decays also had acceptable Cabibbo favoured solutions. If these events, and the 4 ambiguous cases, are really Cabibbo favoured, then there are 23 favoured and 3 suppressed decays. This is consistent with the naïve expectation; if Cabibbo–suppressed decays appear 5% of the time on average, then 14% of the time there will be 3 or more in a sample of 26.

This 'mis–selection' of hypotheses can, in principle, affect the mean lifetime. Nevertheless, when the 4 Cabibbo–suppressed decays were replaced with the ac-

ceptable Cabibbo–favoured solutions, the most probable lifetime did not change significantly.

A third feature of the analysis algorithm which could have led to an erroneous result is the manner in which reconstructed π^0's were combined with the charged decay products to ensure momentum conservation. Since π^0's and the resulting photons left no tracks, there was usually no way to decide whether the π^0 came from the neutrino interaction vertex or the decay vertex. (This decision could be made if a photon converted in the emulsion, and if the e^+e^- pair clearly pointed to one of the vertices.) The cited lack of tracks leads one to question the conjoining of signals in the lead glass with the decay vertices: how likely is it, in fact, that photons unassociated with the decay could be used to reconstruct π^0's and to yield acceptable D^0 hypotheses?

This question was addressed by selecting, from two separate events, two showers whose invariant mass differed from the π^0's mass by less than three standard deviations, and by combining them with the charged particles from a charm–decay candidate from a third event. Events with four prongs and those with two prongs were treated separately; photons from 4–pronged events were combined with other 4–pronged events, and photons from V's were combined with other V's. Only showers which were distinct and unambiguous were used.

From the 4–pronged events, 218 $\gamma\gamma$ combinations were formed, of which 87 had acceptable masses. When these were combined with the charged particles from one of the 4–pronged events, 18 of the ersatz pions yielded acceptable hypotheses (CL $>$ .01). Of those, 5 hypotheses had confidence levels higher than did the combination formed entirely within one event. Consequently, in the two 4–pronged events involving a single π^0, it is justifiable to choose the hypotheses with the highest confidence levels, since there was only an 11% chance that pairs of photons

unrelated to the charged particles could produce decay hypotheses with higher confidence levels.

The V's yielded 508 $\gamma\gamma$ combinations; 143 of them had acceptable invariant masses. Substitution of these bogus π^0's for the secondary π^0 in a V event yielded 15 acceptable hypotheses. None was better than that event's original hypothesis. As in the previous case, it is therefore justifiable to choose the hypotheses with the highest confidence levels; here there was less than a 6% chance that pairs of unrelated γ's could yield higher confidence levels.

Having now considered what the events were not, the remainder of this section discusses the evidence that they were D^0's. Sometimes D^0's come from the decays of D^{*+}'s.

$$\begin{array}{c} D^{*+} \longrightarrow D^0\pi^+ \\ \Big\downarrow \\ X \end{array} \tag{4.38}$$

The difference between the masses of the two charmed particles can be measured much more precisely than can the masses of either the D^0 or the D^{*+}. The uncertainty is determined largely by the uncertainty in the momentum of the pion, which is usually not very energetic, and whose trajectory consequently bends significantly in a magnetic field. In such instances, the momentum can be measured very precisely. The mass difference ($145.41 \pm .16$ MeV/c^2)[20] is only 6 MeV/c^2 greater than the pion's mass, so that unrelated $D^0\pi^+$ pairs are unlikely to yield such a small value.

Three pairs with small mass differences were found (fig. 4.10a). The values, in MeV/c^2, were 148 ± 2, 150 ± 3 and 143 ± 4. All three proved to be kinematically consistent with the D^{*+} hypothesis. To investigate how frequently unrelated D^0's and π^+'s produce small differences, given the momentum distributions peculiar to

this experiment, mass differences were calculated for D's and π's from different events. Of the 1262 combinations formed, four had masses less than or equal to 150 MeV/c^2 (fig. 4.10b). One would thus expect to observe, amongst the 30 combinations formed from D's and π's from the same event, 0.1 examples with masses less than 150 MeV/c^2. Since the probability of observing one or more such cases in a sample of 30 is 9%, the 3 candidates that were found probably came from D^{*+} decays, and were therefore probably D^0's.

Even if a mass difference could not be calculated, the decay chain could still be identified. This situation arose when the momentum of a decay product was not measured. Since the mass difference is so nearly equal to the π^+ mass, the D^0 and the π^+ are released almost at rest in the D^{*+} frame, and they have very little momentum perpendicular to the direction of the D^{*+}. Consequently, in the lab frame, the pion has little momentum transverse to the D^0 direction. In the three D^{*+} cases cited above, the perpendicular momenta were less than 50 MeV/c. This was also true in the four 'mixed-event' combinations, but none of them proved consistent with the D^{*+} hypothesis when analyzed with the kinematical hypothesis–testing programme.

With the criterion that π's from D^{*+}'s have perpendicular momenta less than 50 MeV/c, we examined for evidence of D^{*+}'s those events with incompletely–specified secondary decay products, which also had primary pions whose momenta had been measured. Among the 2584 'mixed-event' pairs formed, 93 satisfied the condition. Moreover, of the 1262 cases already mentioned which allowed a mass difference measurement, 46 had perpendicular momenta less than 50 MeV/c (fig. 4.10d), and none was consistent with the D^{*+} decay chain. Since the fraction of 'mixed-event' pairs with perpendicular momenta less than 50 MeV/c is the same in both samples, we were able to use the restricted sample to conclude that the

probability of an unrelated pair having a p_t of 50 MeV/c or less, and which fit the D^* hypothesis, is less than 2.1% (1/47).

In the sample of 68 'same-event' pairs which included D^0's with undetermined momenta, six cases met the transverse momentum condition (fig. 4.10c). All six were kinematically consistent with the D^{*+} hypothesis. Since the probability of observing by chance one or more examples in a set of 68 is less than 12% , all six candidates were probably D^{*+}'s. (Two of these were outside the fiducial volume, and were not included in the collection of 39 decays for which a mean lifetime was calculated. They have been discussed here to illustrate the characteristics of the $D^{*+} \rightarrow D^0\pi^+$ decay chain.)

In the full sample of 39 D^0 candidates, there were four primary tracks which stopped in the emulsion, and 22 more which were not matched in the drift chambers. The momenta of these tracks could not be measured, but the events could still yield evidence of D^{*+}s. In the six previously–identified D^{*+} events, the angles between the π^+ tracks and the directions of the D^0s were less than 70 mr. Of the 1262 'mixed-event' pairs which had both mass difference and p_t measurements, 90 had angles less than 70 mr. None was consistent with the D^{*+} hypothesis. This corresponds to a limit of 1.1% (1/91). Among the 'same-event' pairs in which all momenta were measured, there were ten cases with opening angles less than 70 mr, six of which fit the D^{*+} hypothesis. These are the D^{*+} candidates already identified. The probability of having one or more acceptable fits, by chance, in a sample of 10 is less than 10%. Thus if the angle between a π^+ and a D^0 is less than 70 mr, and the kinematic fit to a D^{*+} decay is acceptable, the event is probably the decay of a D^{*+}. When the events with primary pions with unmeasured momenta were examined, no cases were found that were consistent with the D^{*+} hypothesis.

To summarize, four decay candidates were identified as D^0's because it was established that they came from D^* decays.

There are two other decay chains involving D^*'s and D^0's,

$$D^{*0} \rightarrow D^0\pi^0$$

and

$$D^{*0} \rightarrow D^0\gamma. \tag{4.39}$$

In principle, the first has characteristics similar to those of the $D^{*+} \rightarrow D^0\pi^+$ chain, since the pions have similar masses, as do the D^*'s. Specifically, the mass difference is very nearly equal to m_{π^0}, so that unrelated $D\pi$ pairs are most likely to have mass differences much larger than 145 MeV/c^2. Moreover, the momentum of the π^0 perpendicular to the D^0 direction is small.

Practical considerations altered these expectations. The π^0 candidates were reconstructed from pairs of photons. Measurements of the photon energies, made with the lead glass system, are less precise than are measurements made with the drift chambers of the momenta of charged particles. Furthermore, there are two photons to dominate the uncertainty in the mass difference, whereas in the charged case there was only one π^+. Accordingly, the uncertainty is greater than in the charged case.

Pairs of γ's were selected using the following criteria: the invariant mass was greater than 70 MeV/c^2, less than 200 MeV/c^2, and differed from m_{π^0} by less than 2.5 standard deviations; neither photon had an energy more than five times greater than the energy of the other; the net momentum of the two γ's perpendicular to the D direction was less than 50 MeV/c; and finally the momentum of the π^0 was less than 2.0 GeV/c. The last condition was introduced because the momenta of the primary pions in the D^{*+} decays were less than 1.6 GeV/c.

Three triplets satisfied these conditions. One involved a D^0 already identified as part of a D^{*+} chain. The other two had mass differences that were too large and imprecise (222±54 GeV/c^2 and 215±55 GeV/c^2). Thus, no examples of the $D^{*0} \rightarrow D^0\pi^0$ chain were identified.

The third decay chain is $D^{*0} \rightarrow D^0\gamma$. Unfortunately, the kinematic restrictions are less exigent than in the $D\pi$ cases. The photon is massless, so that relatively many unrelated D's and γ's might be expected to yield mass difference values between the canonical mass difference[20], 142.5 MeV/c^2, and the kinematic limit, 0.0 MeV/c^2. Moreover, the perpendicular momenta of the γ's with respect to the D directions need not be small. There was no evidence to indicate the presence of the $D^{*0} \rightarrow D^0\gamma$ chain in the D^0 sample (fig. 4.11).

Most of the decays in the full sample were consistent with one or more hypotheses, since not all of the secondary particles could be identified. The proper lifetime for each event was calculated assuming that each reaction was the decay of a D^0. To test this assumption, a Gaussian ideogram of fitted parent masses was generated. The fitted masses and uncertainties, m_{ij} and σ_{ij}, were calculated using the hypothesis–testing programme, requiring only that energy and momentum be conserved at each vertex. In cases involving the decay of a π^0, the pion's mass was constrained to be 134.96 MeV/c^2. The Gaussian function $F(m_0)$ was then calculated.

$$F(m_0) = \sqrt{\frac{1}{2\pi}} \sum_{j=1}^{25} \frac{1}{n_j} \sum_{i=1}^{n_j} \frac{1}{\sigma_{ij}} e^{-.5(m_{ij}-m_0/\sigma_{ij})^2} \tag{4.40}$$

The double sum extended over all acceptable (C.L.> 0.01) meson–decay hypotheses, and over the 25 events for which a mass could be calculated. Each event had n_j hypotheses. The result, shown in figure 4.12, is that there is a very clear clustering of fitted masses about a central value (1865 MeV/c^2) consistent with the

accepted mass of the D^0 (1864.7 MeV/c^2). This supports the assumption, explicit in the lifetime calculations, that all the events in the sample were D^0 decays.

Conclusion

In this chapter, it has been shown that decay candidates were found independently of their positions along the beam direction in the emulsion, and of their decay lengths (except for very short lengths, and for decays outside the target). There is no evidence that the events were anything but the decays of D^0 mesons; in particular, they were neither strange decays, baryon decays, nor nuclear interactions. In some cases, events were identified as D^0's because they came from D^{*+} decays. The most likely average invariant mass of all the events is 1865, consistent with the accepted D^0 mass. Finally, the most probable mean lifetime of the sample is $4.8^{+0.9}_{-0.7} \times 10^{-13}$ seconds.

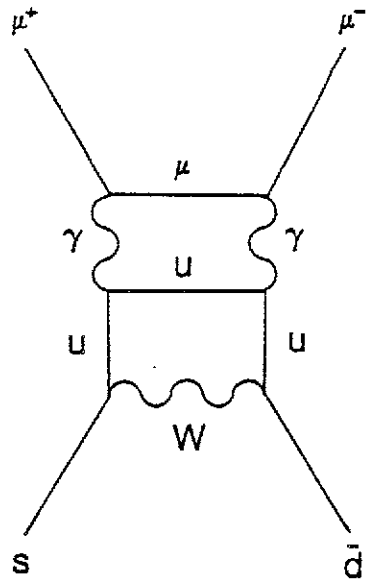

Figure 1.1. $K_L^0 \longrightarrow \mu^+\mu^-$

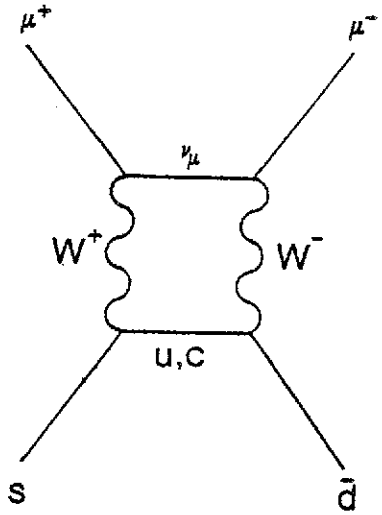

Figure 1.2. $K_L^0 \longrightarrow \mu^+\mu^-$

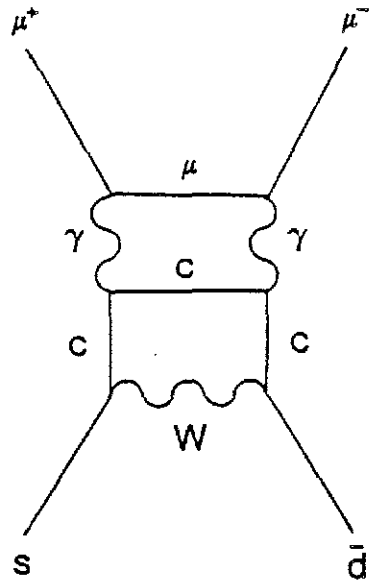

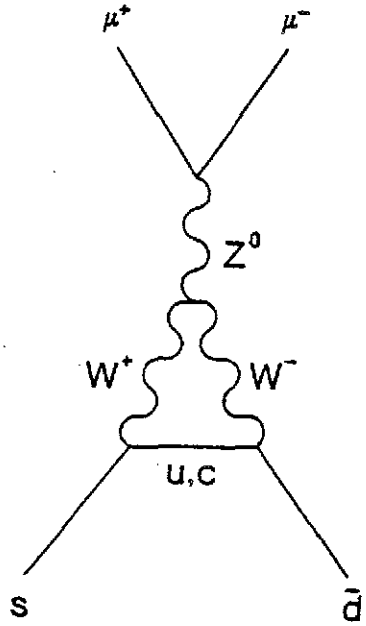

Figure 1.3. $K_L^0 \longrightarrow \mu^+\mu^-$

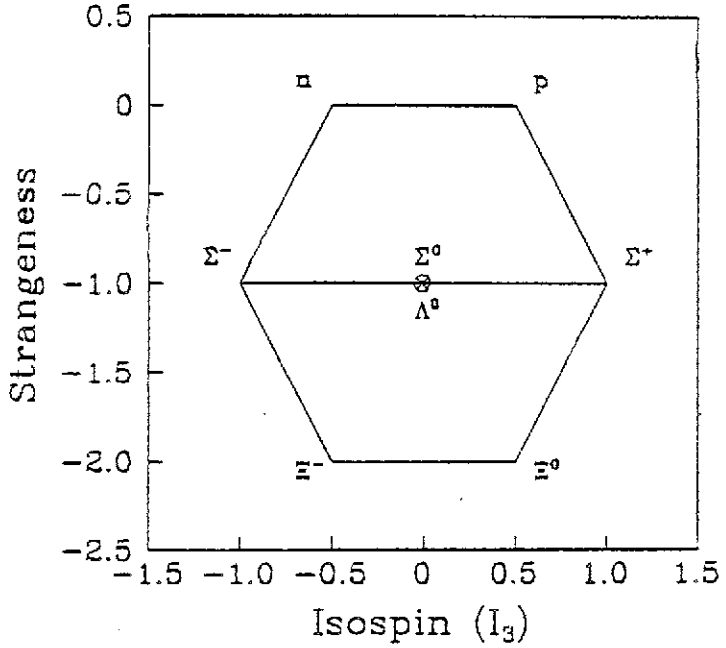

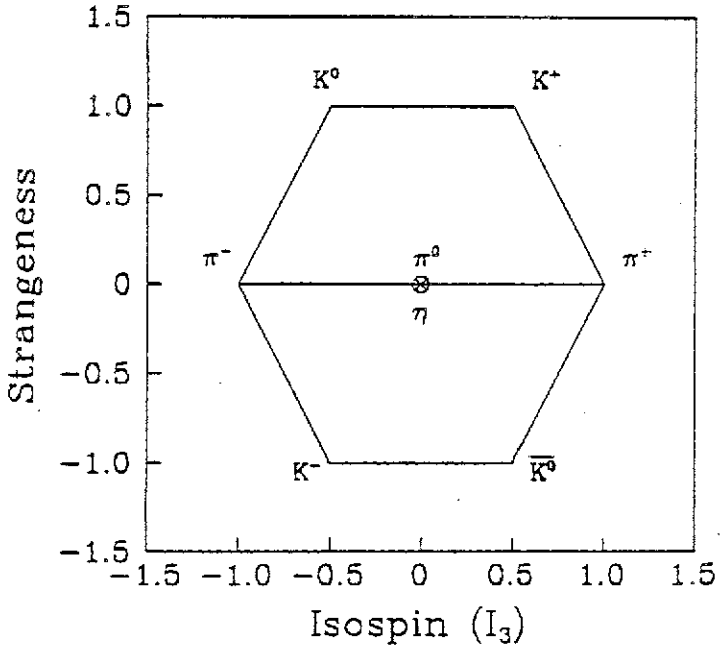

Figure 2.1. Meson and Baryon SU(3) Octets

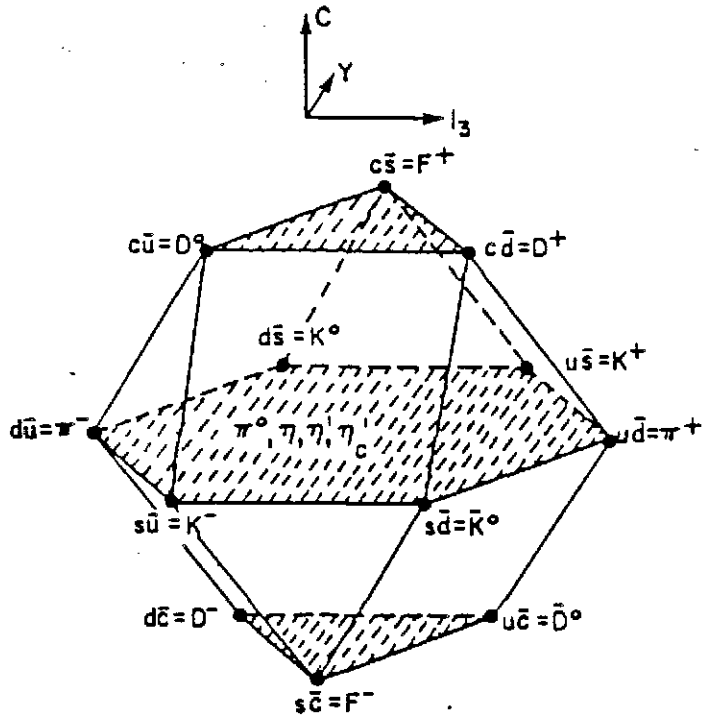

$J^P = 0^-$ MESONS

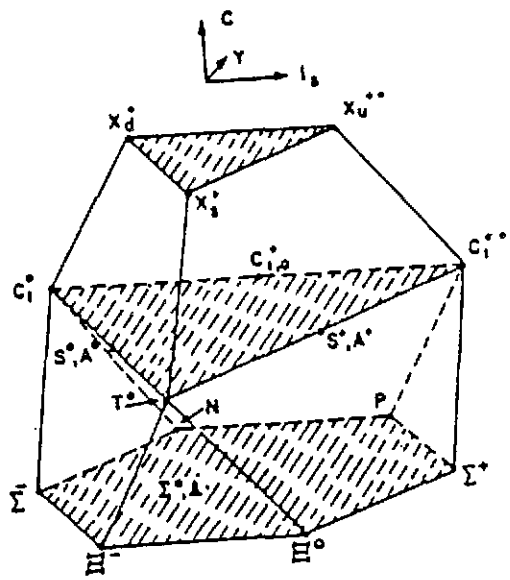

$J^P = \frac{1}{2}^+$ BARYONS

Figure 2.2. Meson and Baryon SU(4) Multiplets

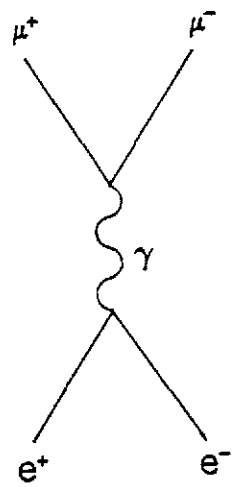

Figure 2.3a. $e^+e^- \longrightarrow \mu^+\mu^-$

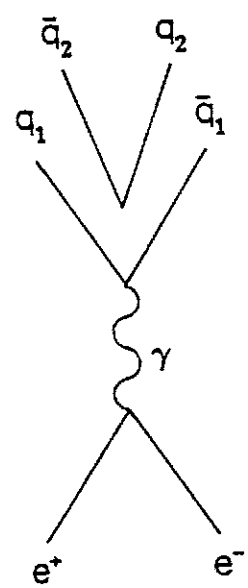

Figure 2.3b. $e^+e^- \longrightarrow$hadrons

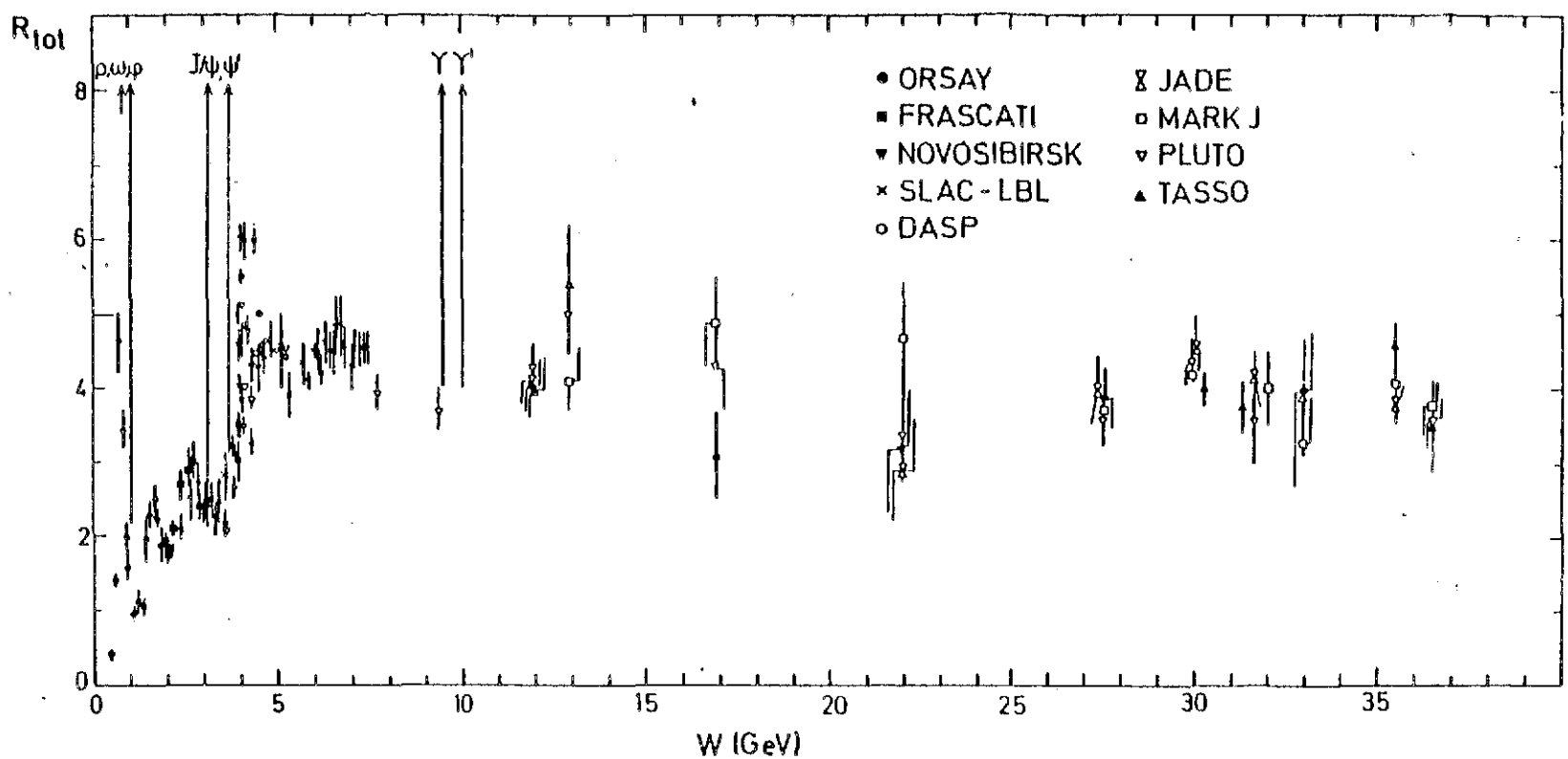

Figure 2.4: R *vs.* W

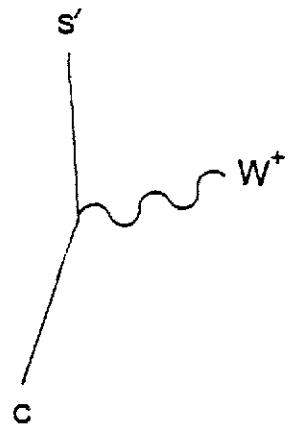

Figure 2.5. Second Term in S–Matrix

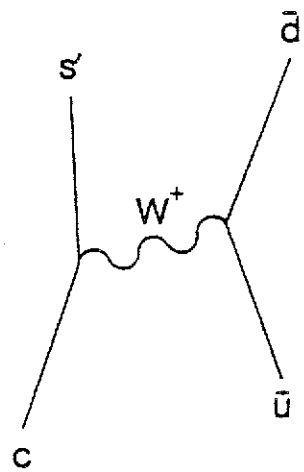

Figure 2.6. Third Term in S–Matrix

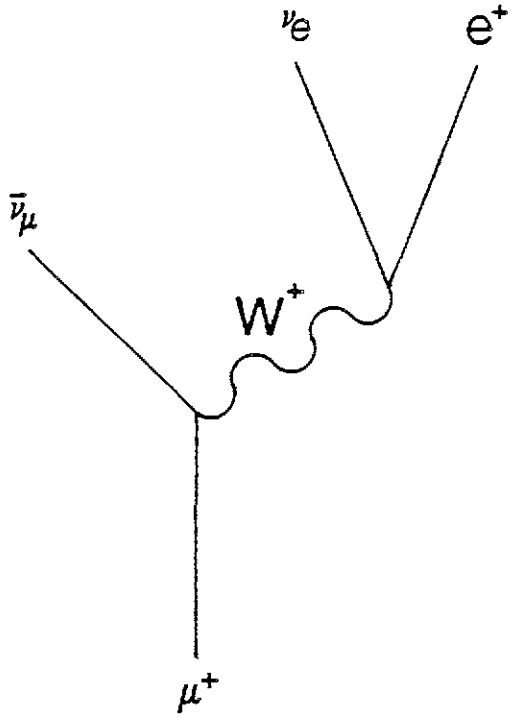

Figure 2.7. Muon Decay

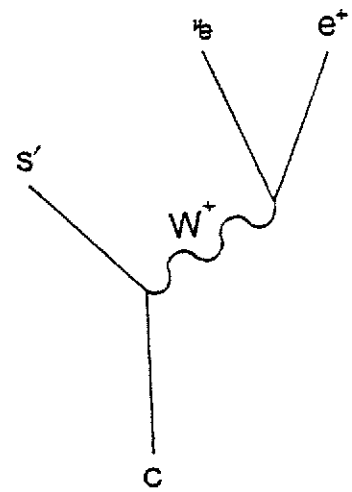

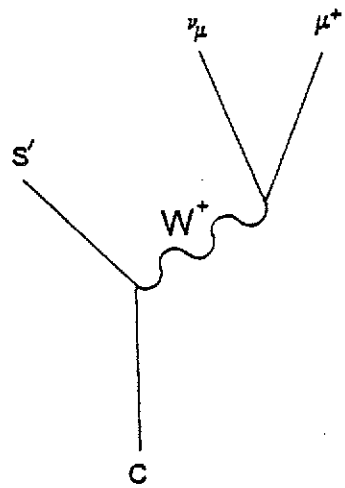

Figure 2.8. Decay of a Charmed Quark

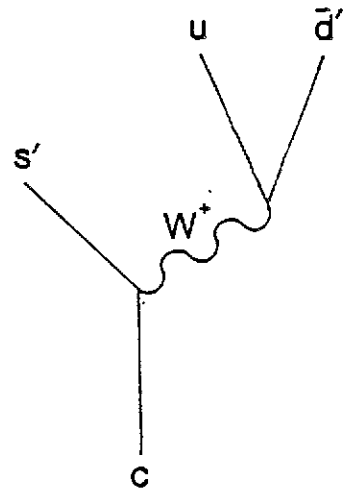

Figure 2.8a. Decay of a Charmed Quark

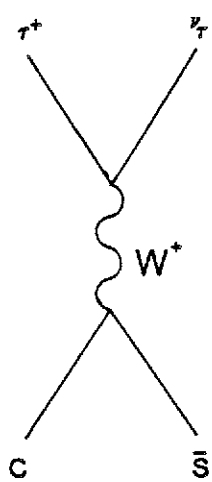

Figure 2.9. $F^+ \longrightarrow \tau^+ \nu_{tau}$

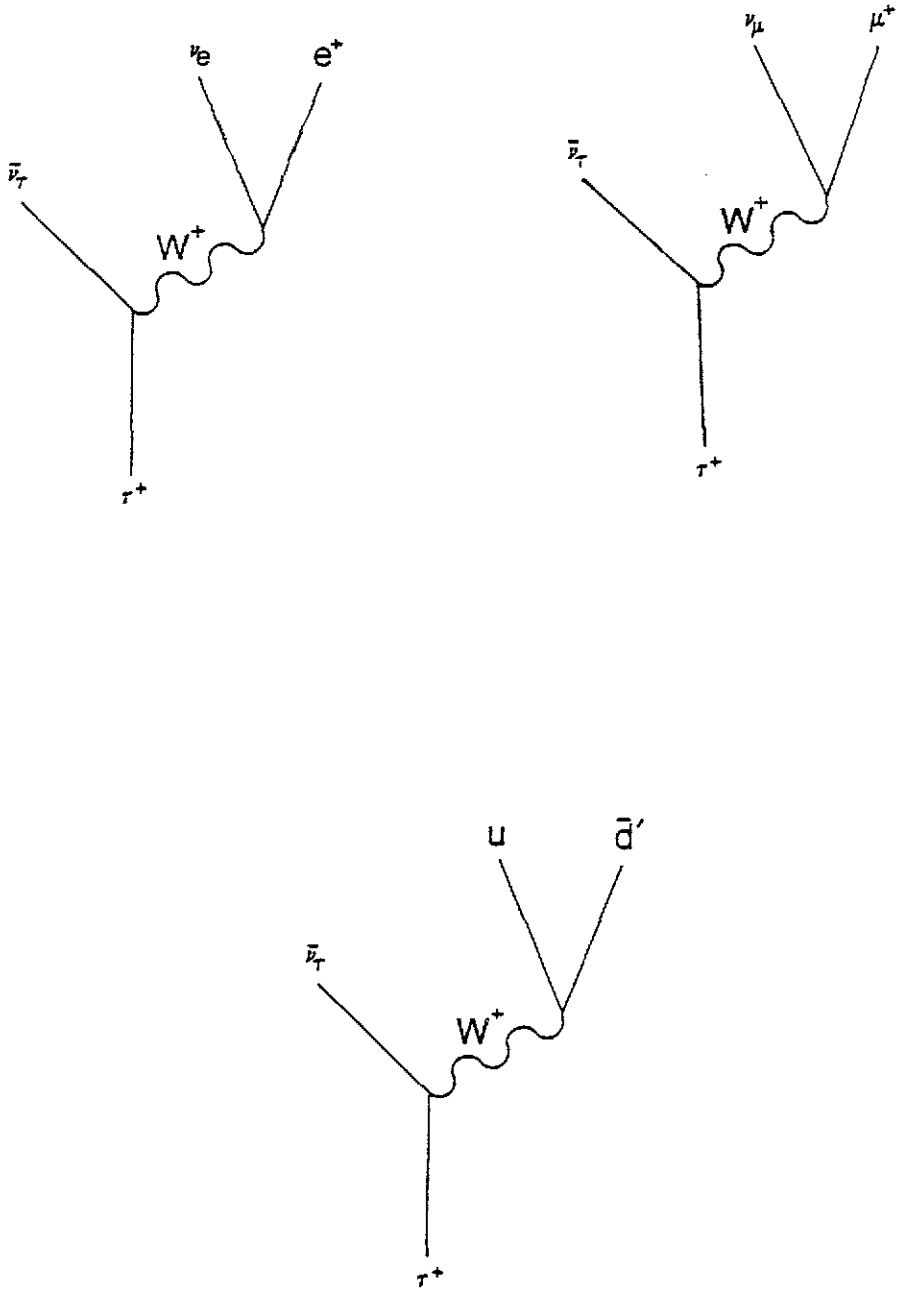

Figure 2.10. Tau Decay

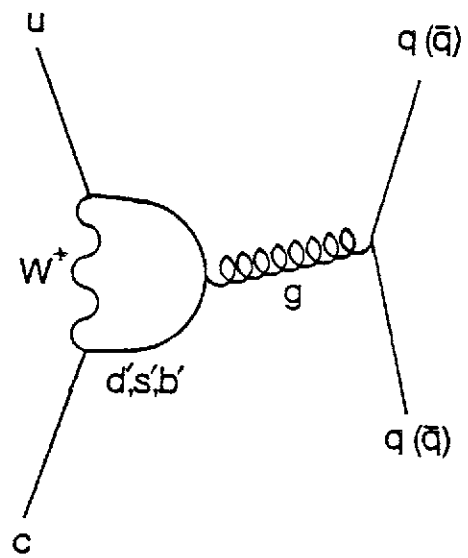

Figure 2.11. The 'Penguin' Mechanism

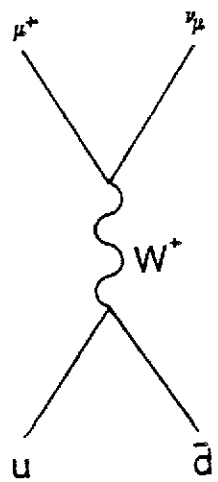

Figure 2.12. Pion Decay

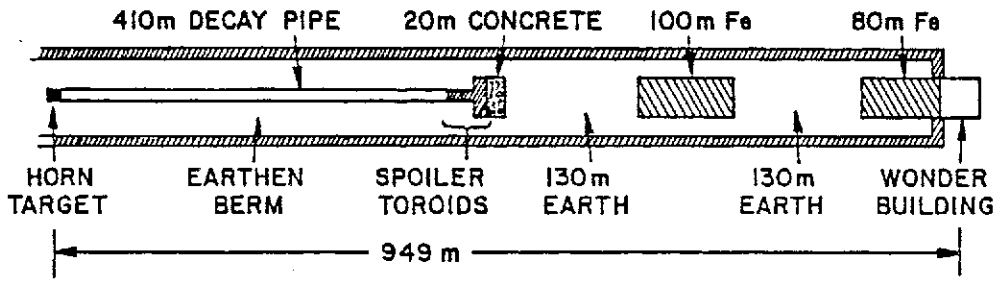

Figure 3.1. The Neutrino Beam Line

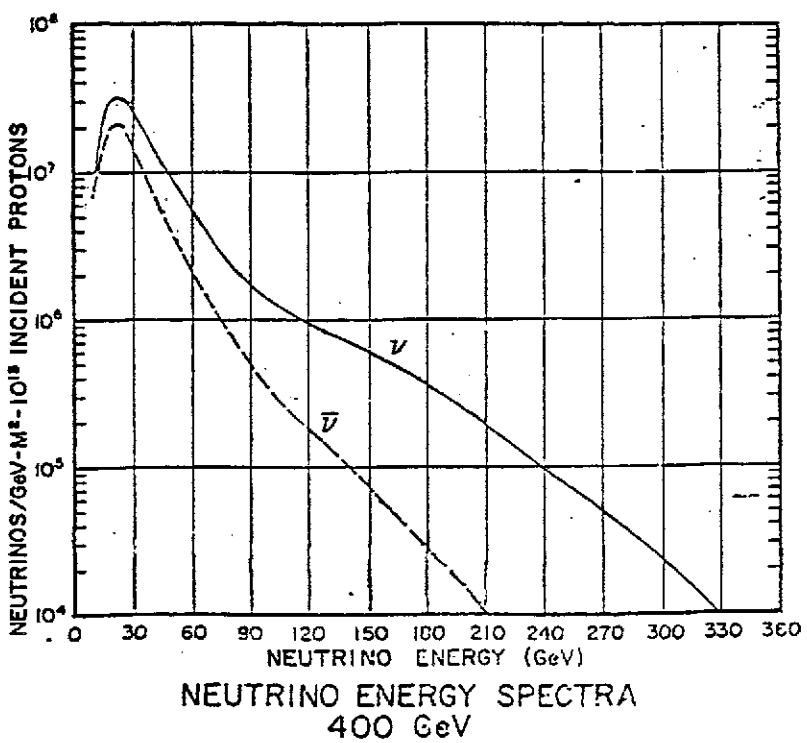

Figure 3.2. The Neutrino Momentum Spectrum

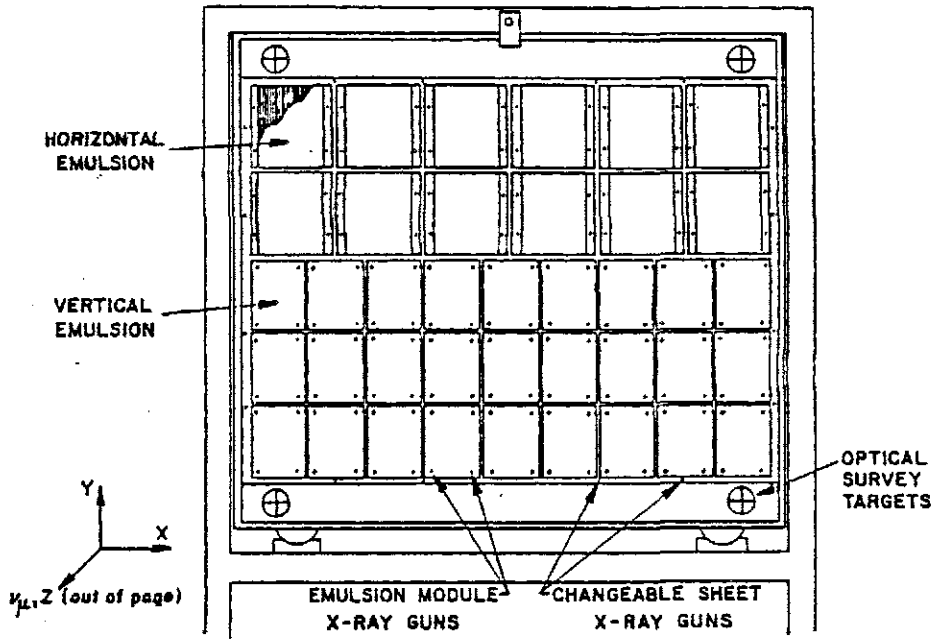

Figure 3.3. The Emulsion Target – Looking Upstream

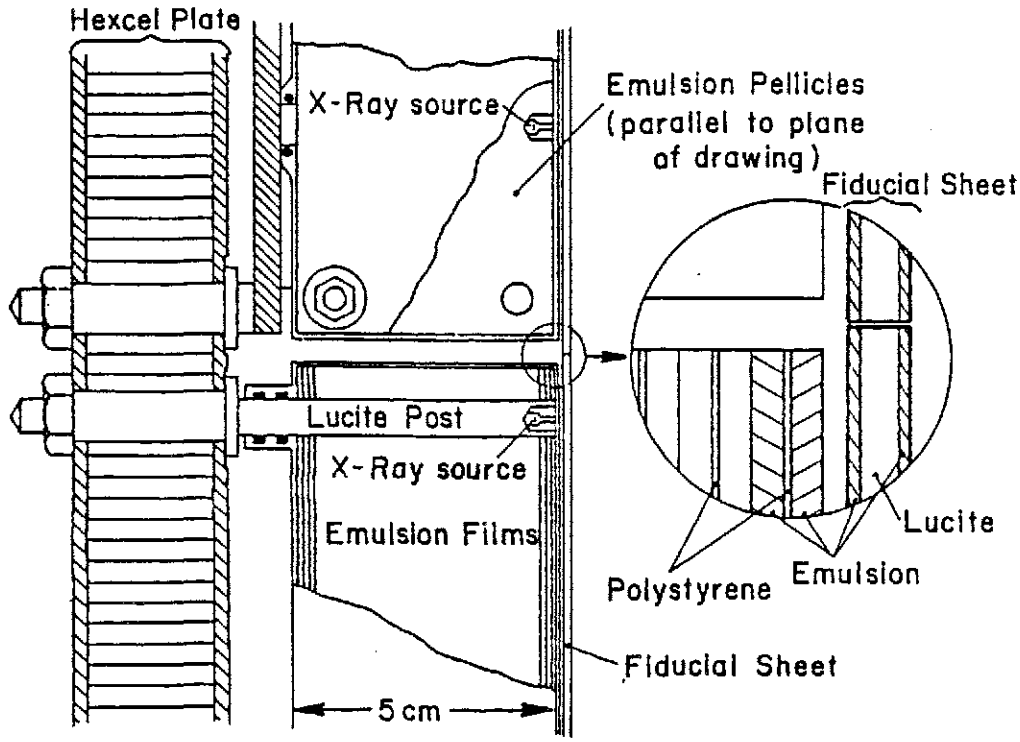

Figure 3.4. The Emulsion – Cut-away View

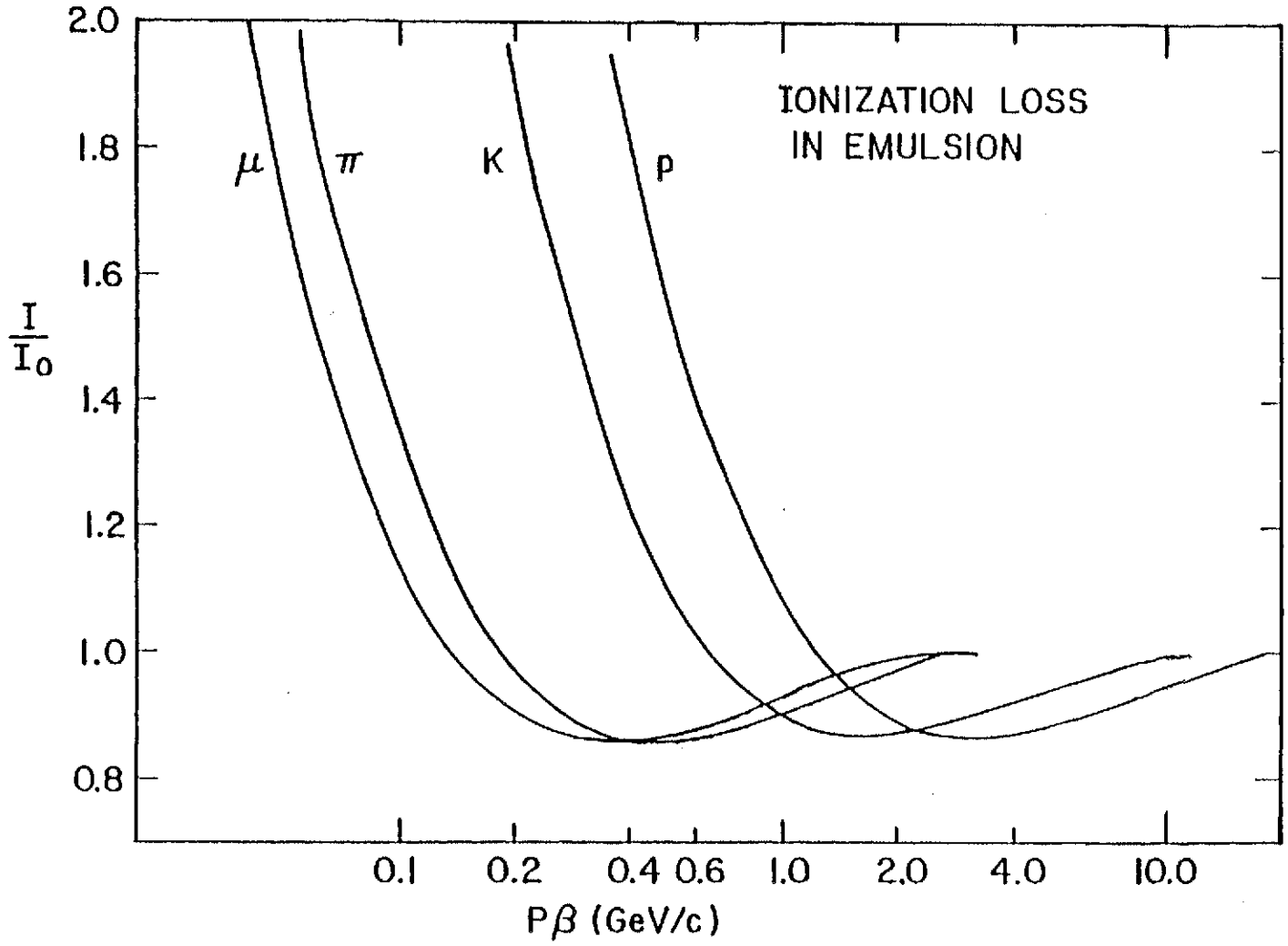

Figure 3.5. Ionization *vs.* $P\beta$ in Emulsion

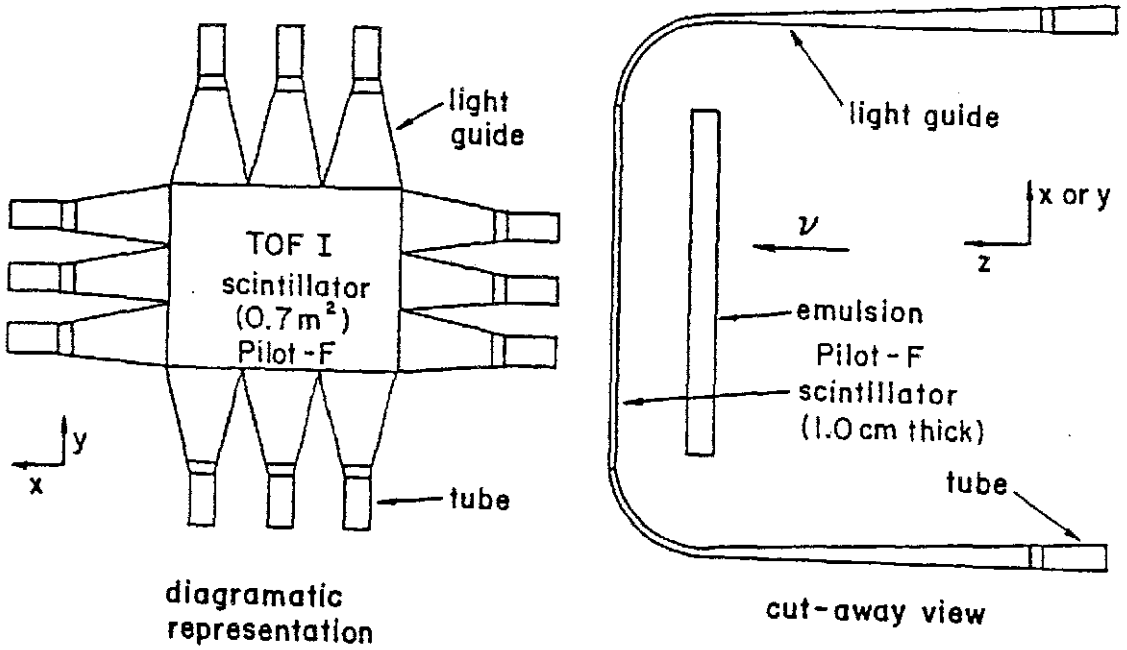

Figure 3.6 Time–of–Flight I

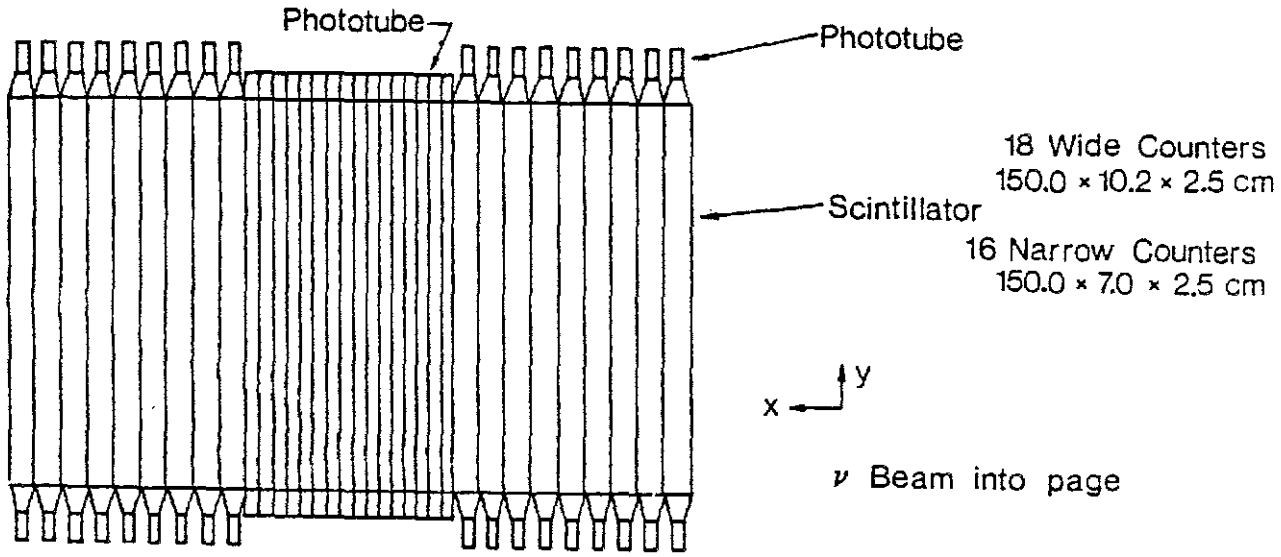

Figure 3.7. Time–of–Flight II

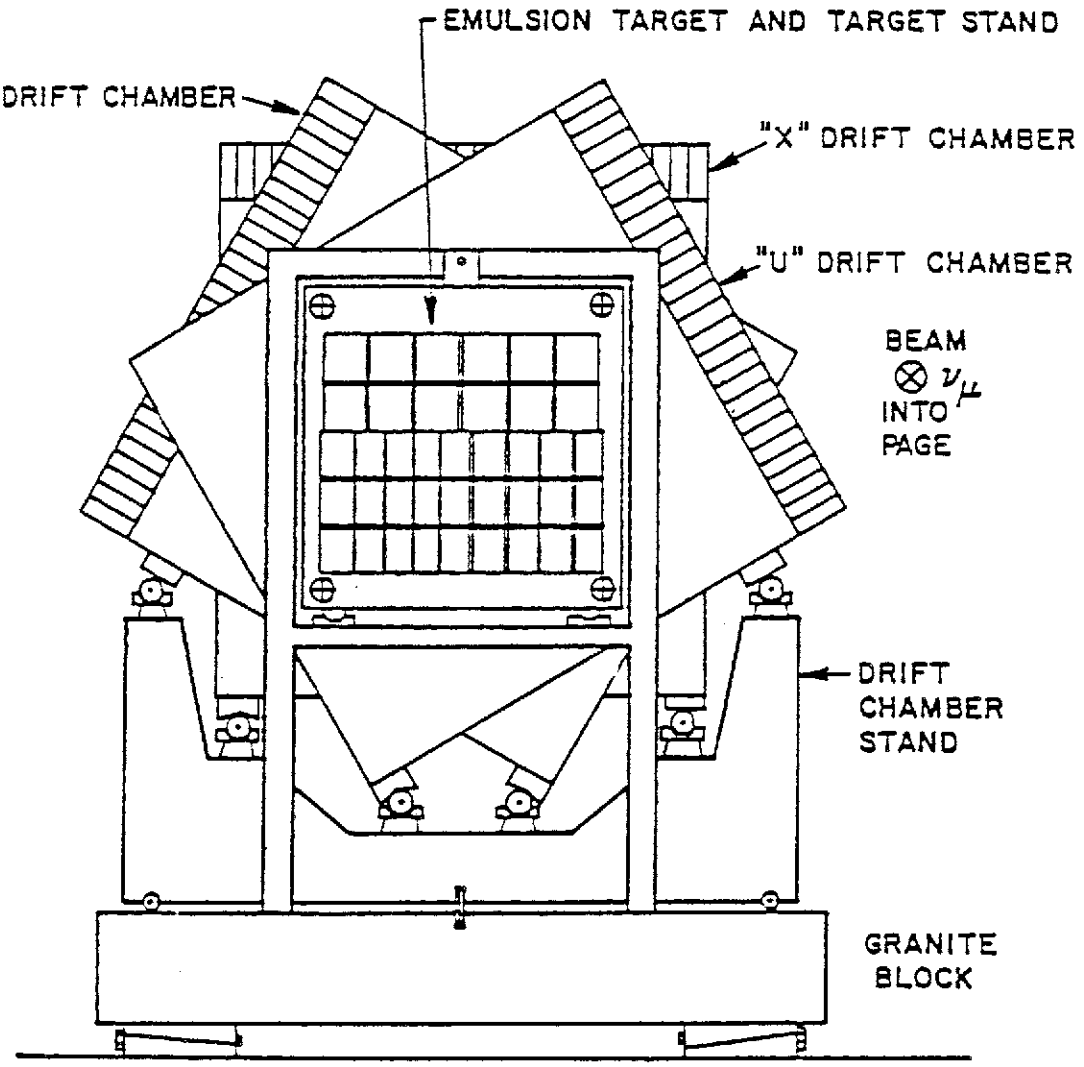

Figure 3.8. Upstream Drift Chambers

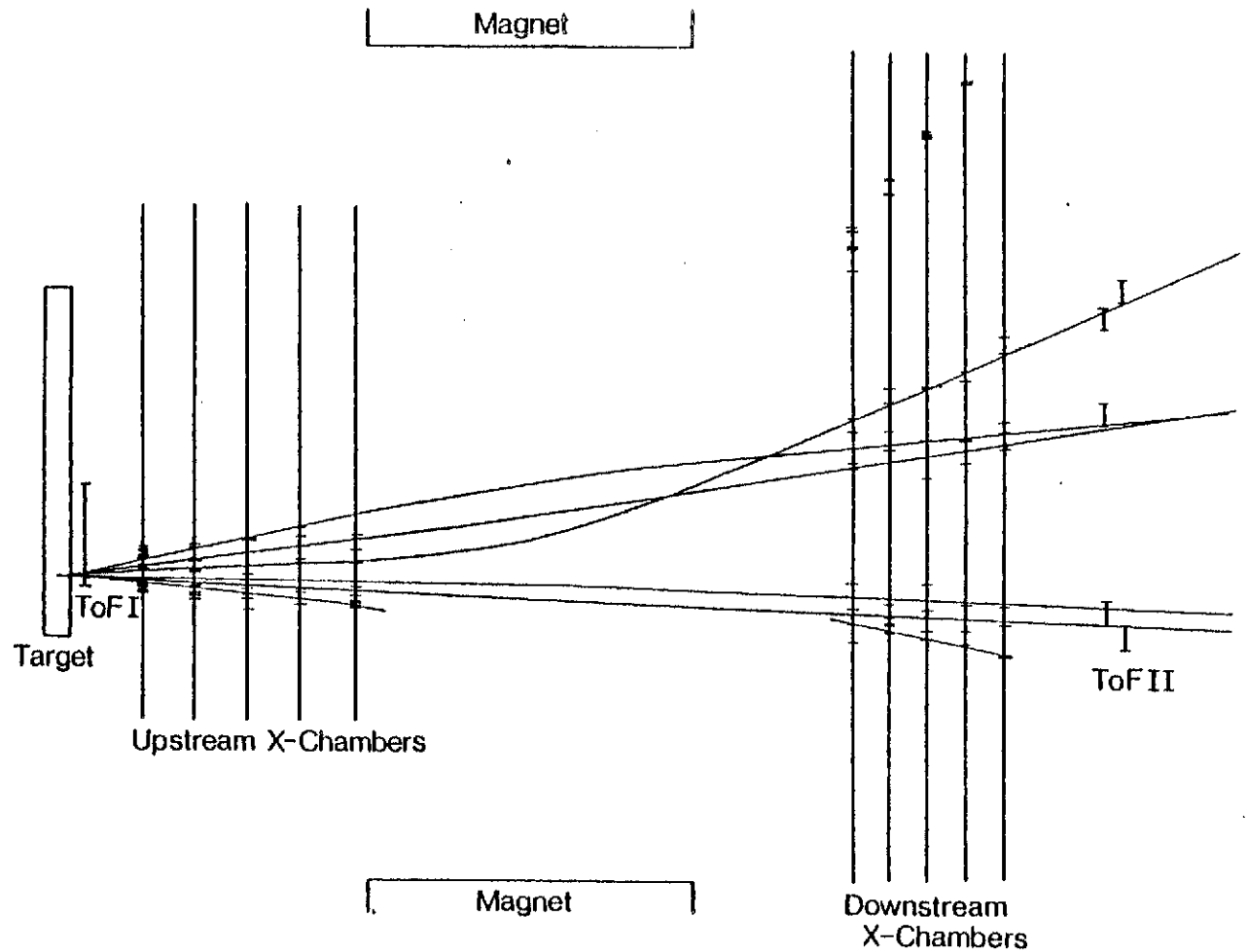

Figure 3.9. Tracks in the Magnetic Spectrometer

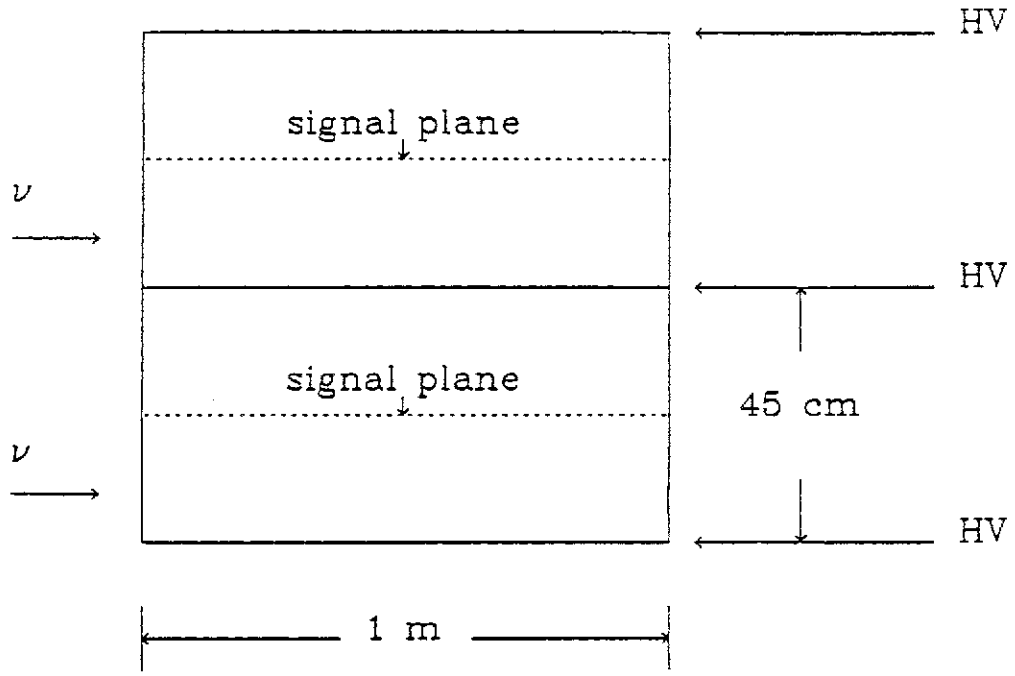

Figure 3.10. Charged Particle Identifier – Side View

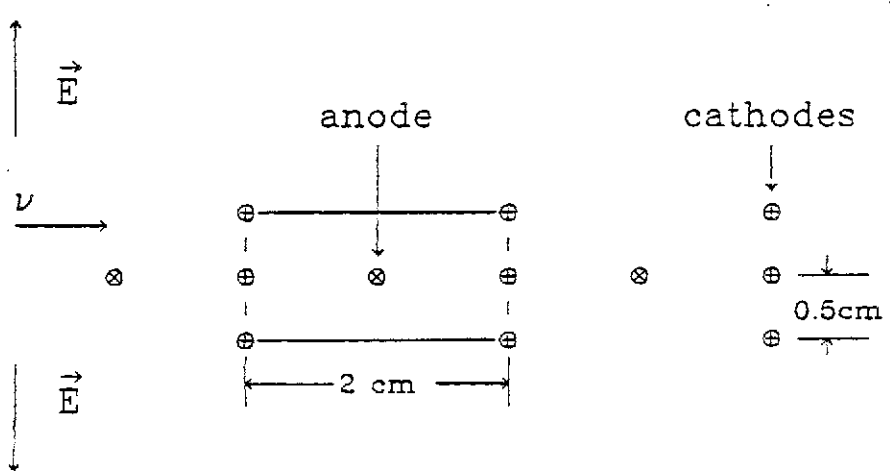

Figure 3.11. Proportional Cells of the CPI

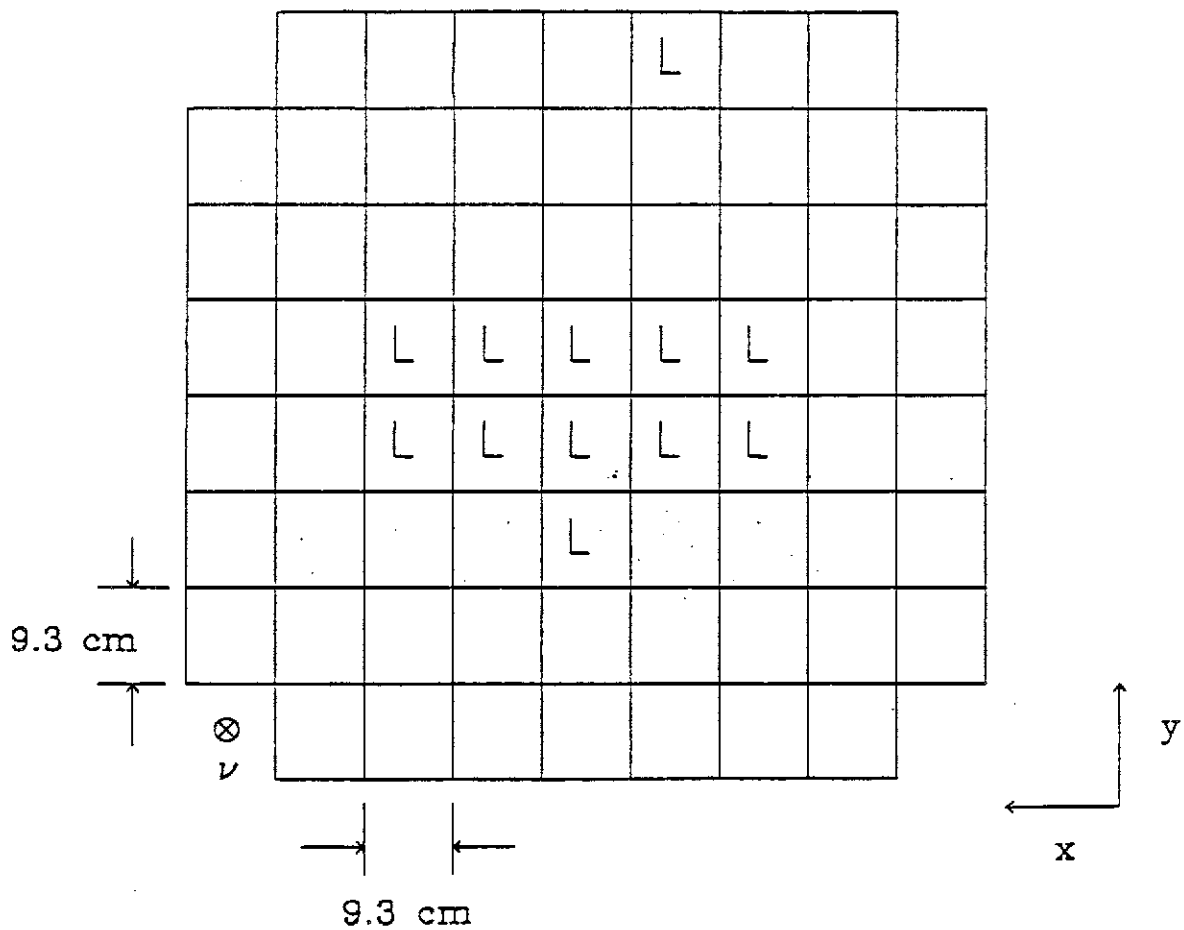

Figure 3.12. Lead Glass Array

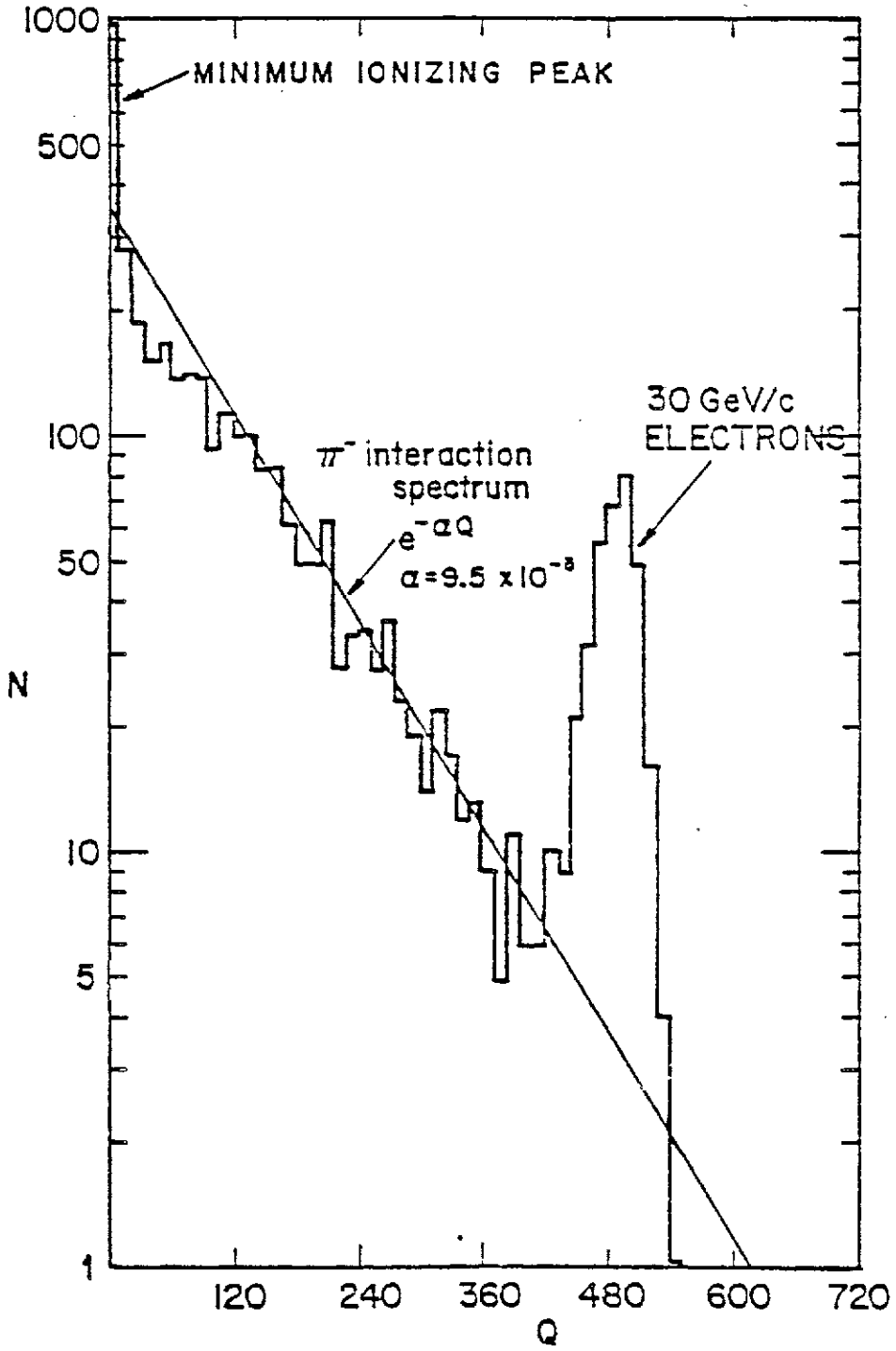

Figure 3.13. Pion Energy Loss Spectrum in Lead Glass

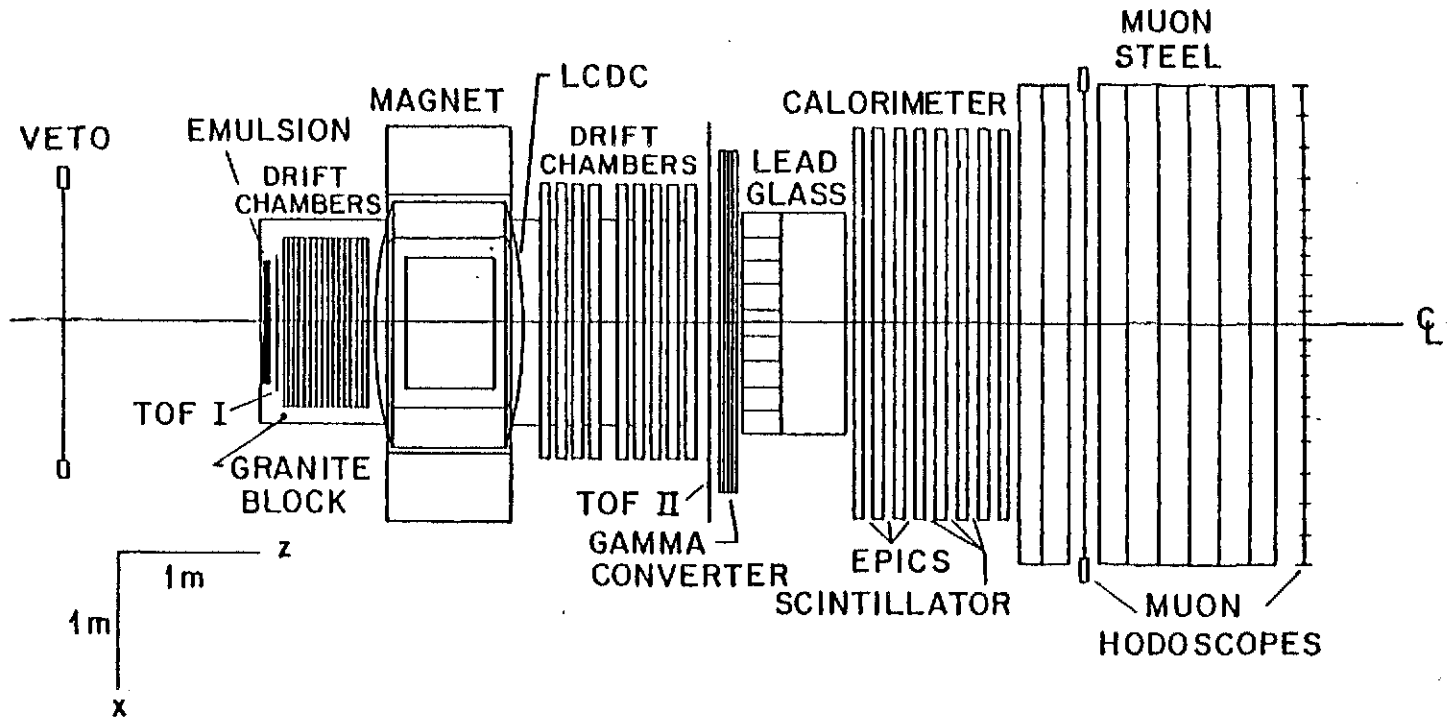

Figure 3.14. The E531 Spectrometer–Side View

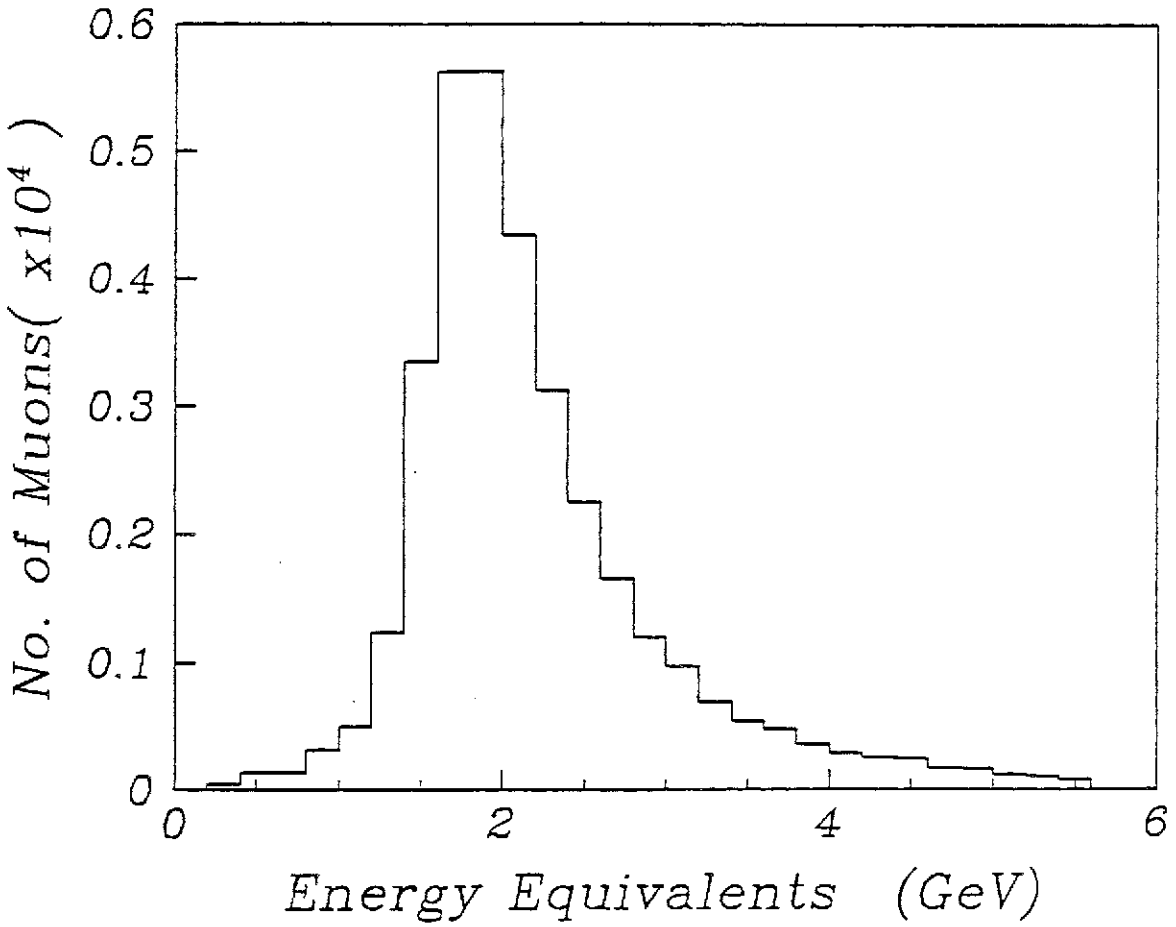

Figure 3.15. Muon Energy Loss Spectrum in the Calorimeter

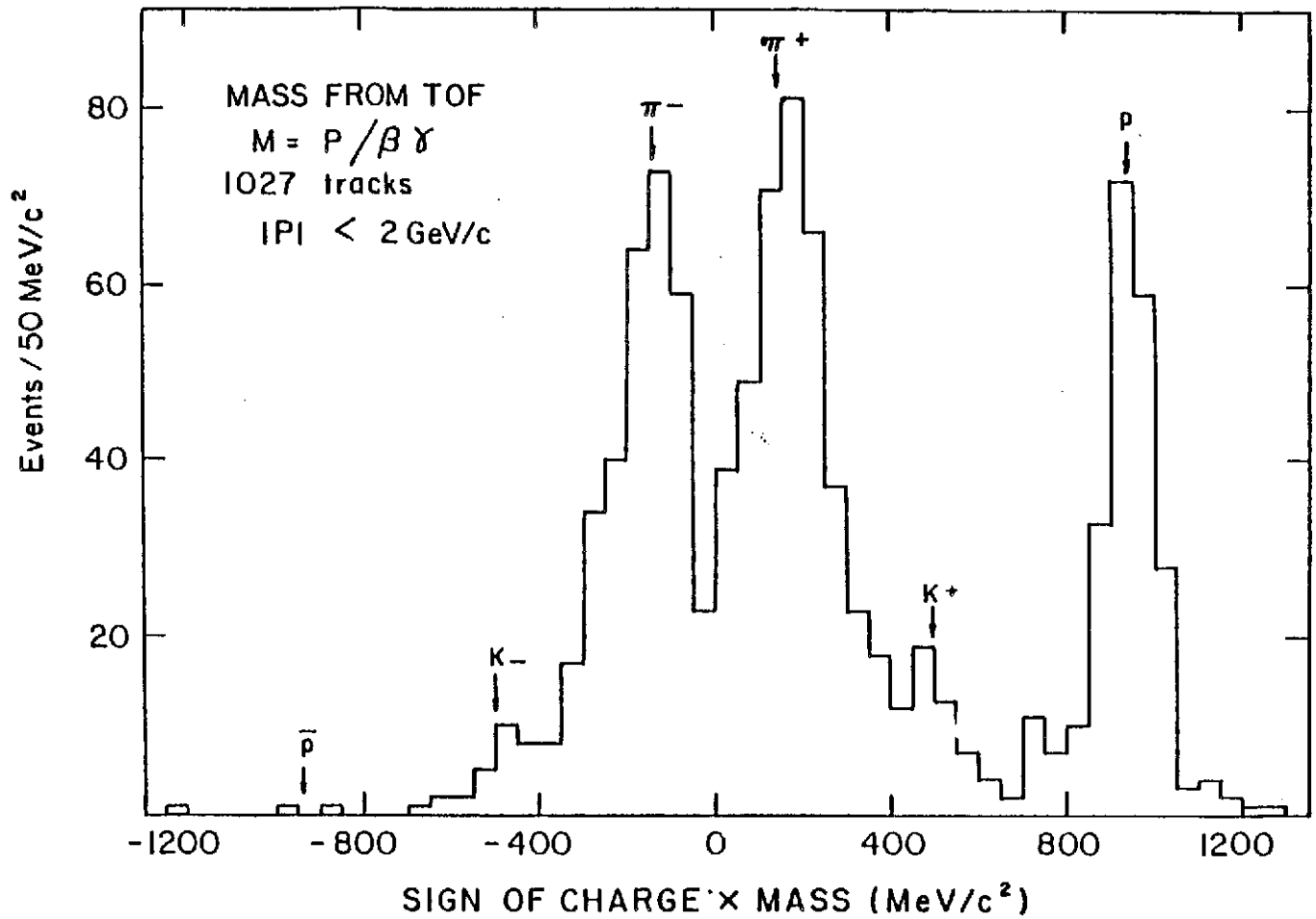

Figure 3.16. Masses Determined by Time-of-Flight

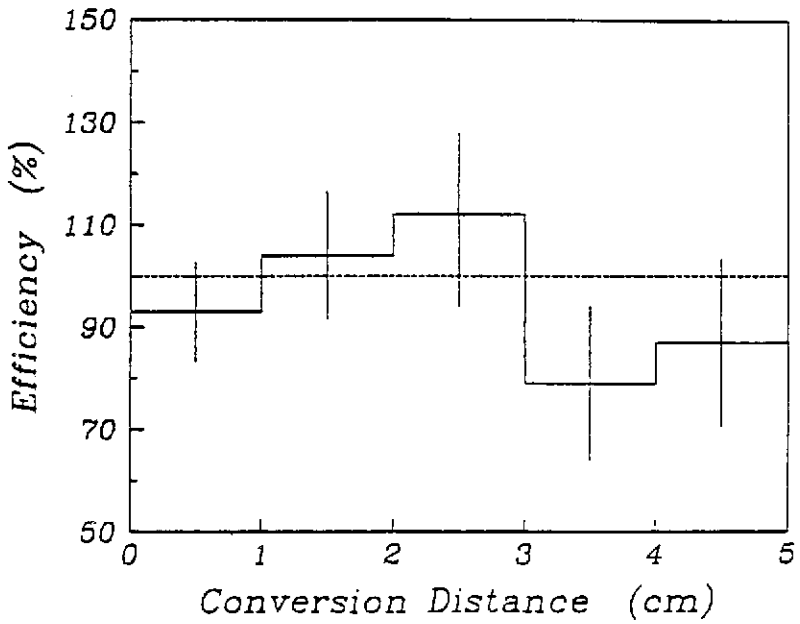

Figure 4.1. Conversion Finding Efficiency

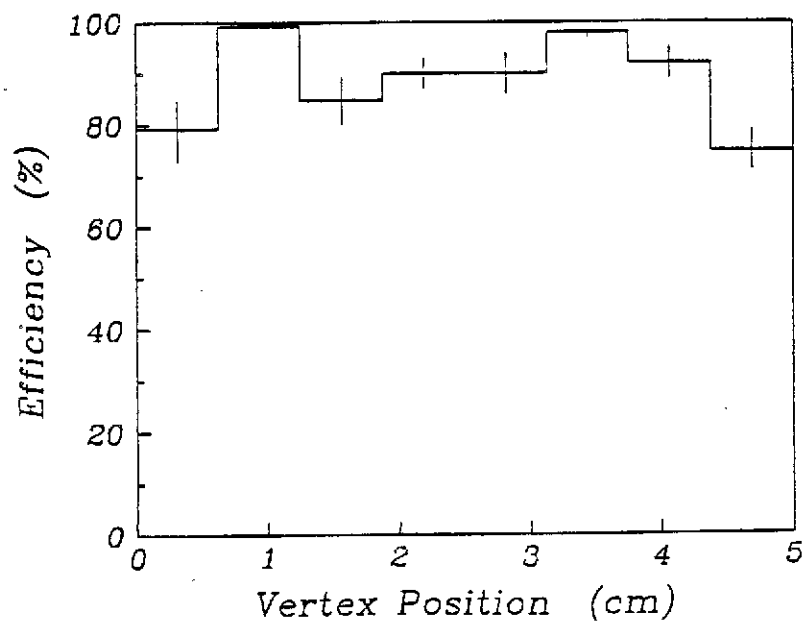

Figure 4.2. Vertex Finding Efficiency

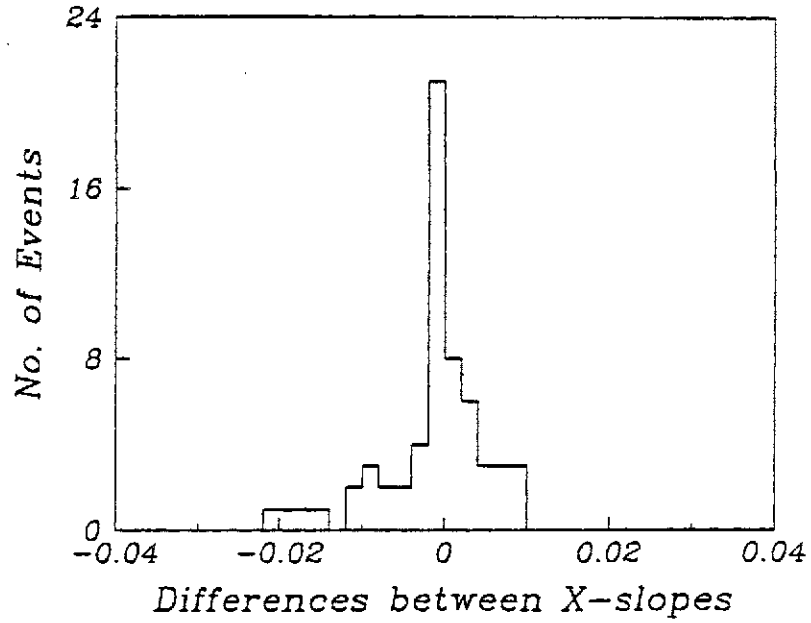

Figure 4.3a. DC Slopes − Exit Slopes; dx/dz

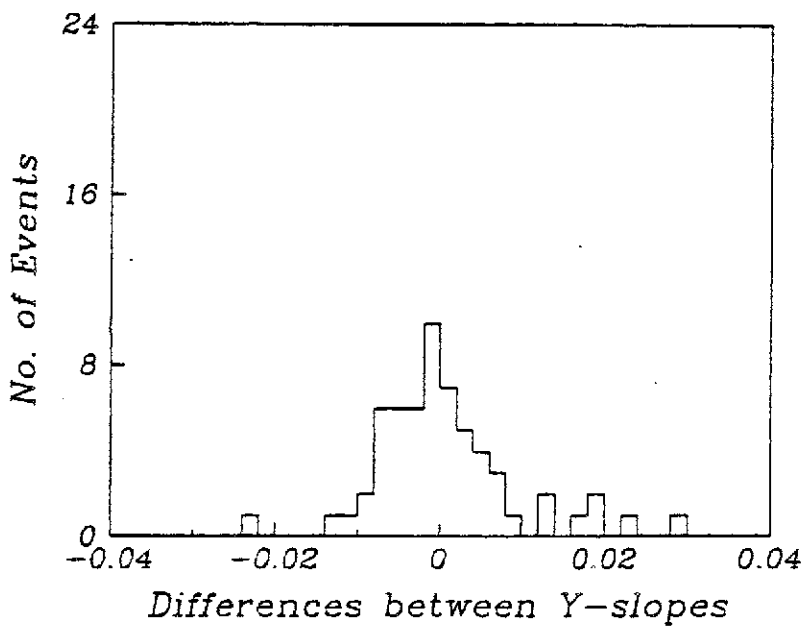

Figure 4.3b. DC Slopes − Exit Slopes; dy/dz

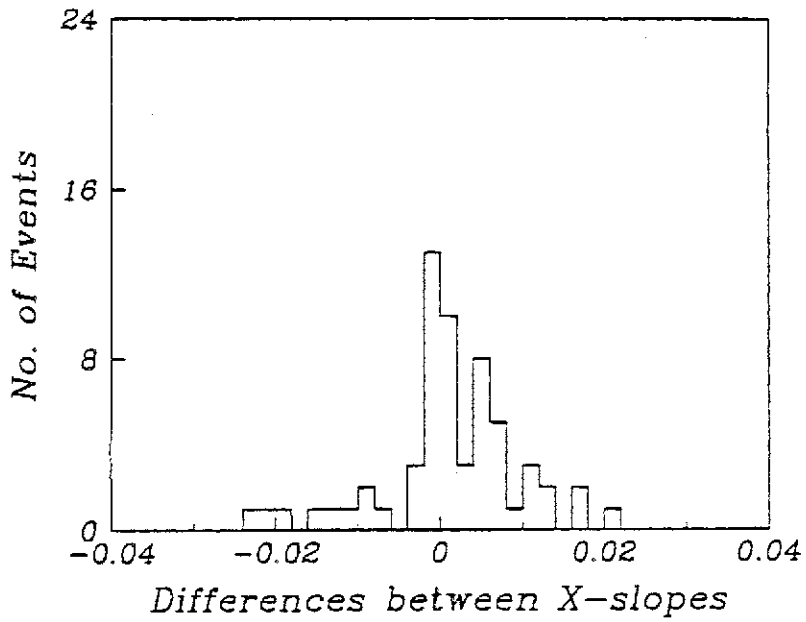

Figure 4.3c. DC Slopes − Decay Slopes; dx/dz

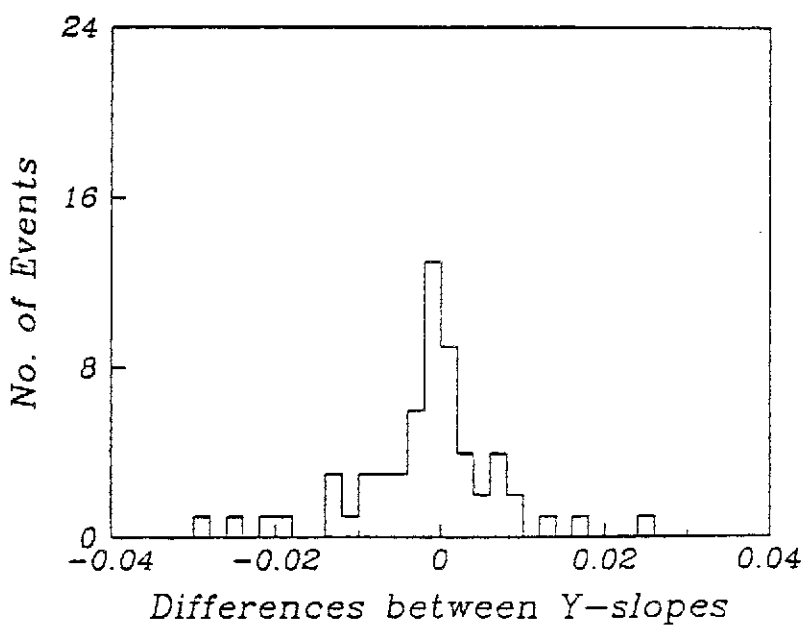

Figure 4.3d. DC Slopes − Decay Slopes; dy/dz

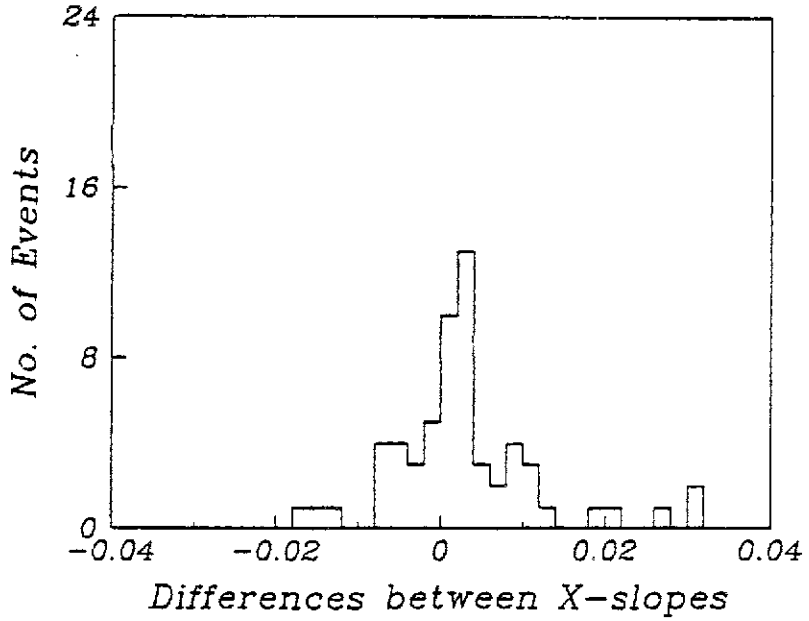

Figure 4.3e. Exit Slopes − Decay Slopes; dx/dz

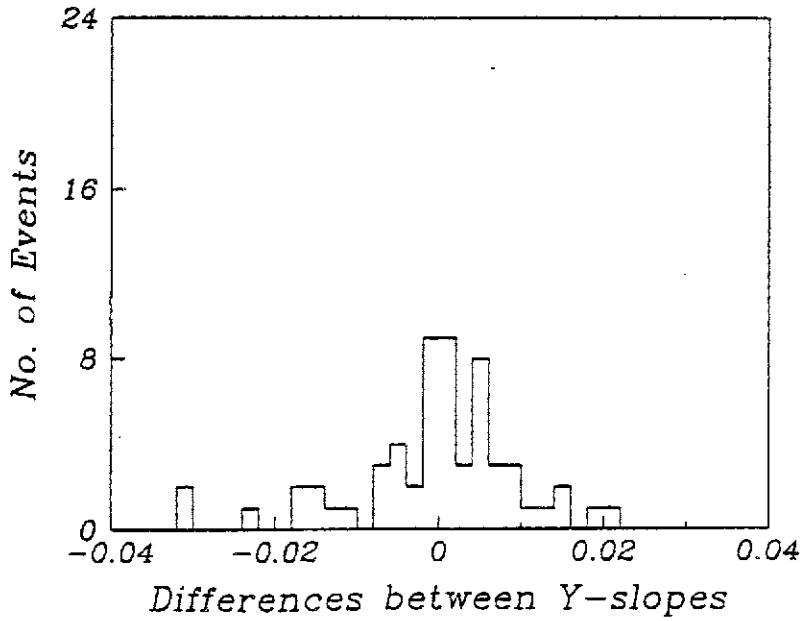

Figure 4.3f. Exit Slopes − Decay Slopes; dy/dz

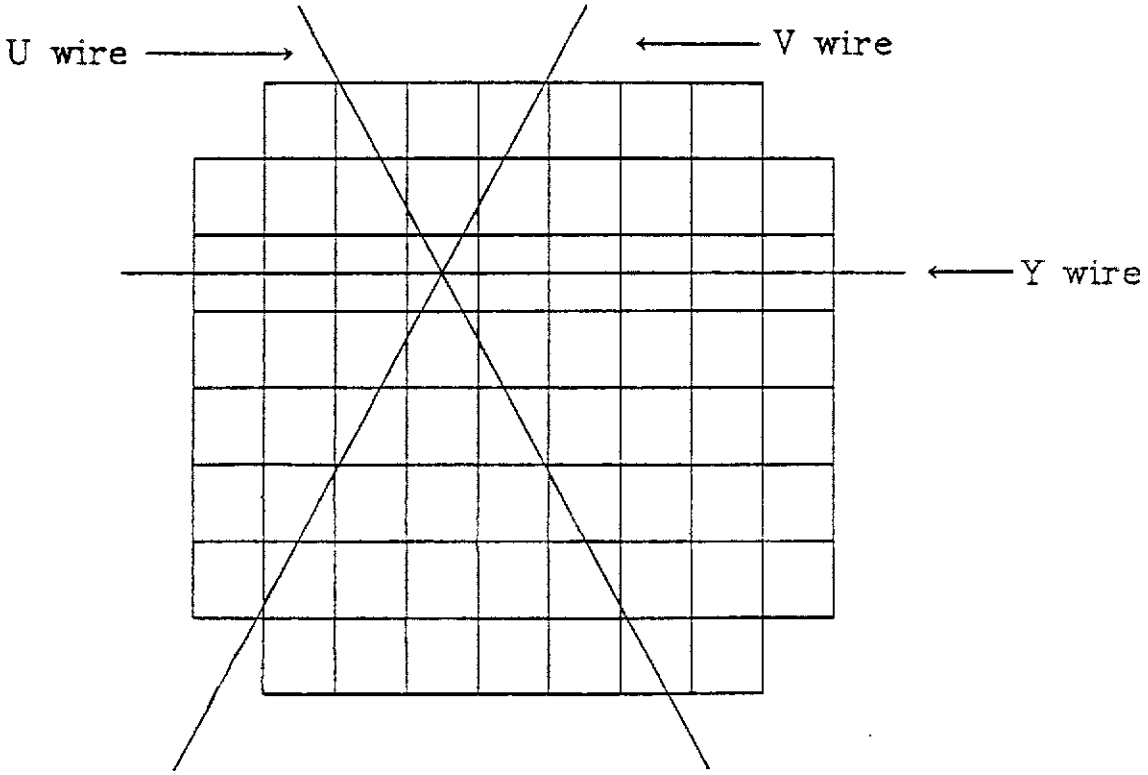

Figure 4.4. A Triple Coincidence in the EPIC's

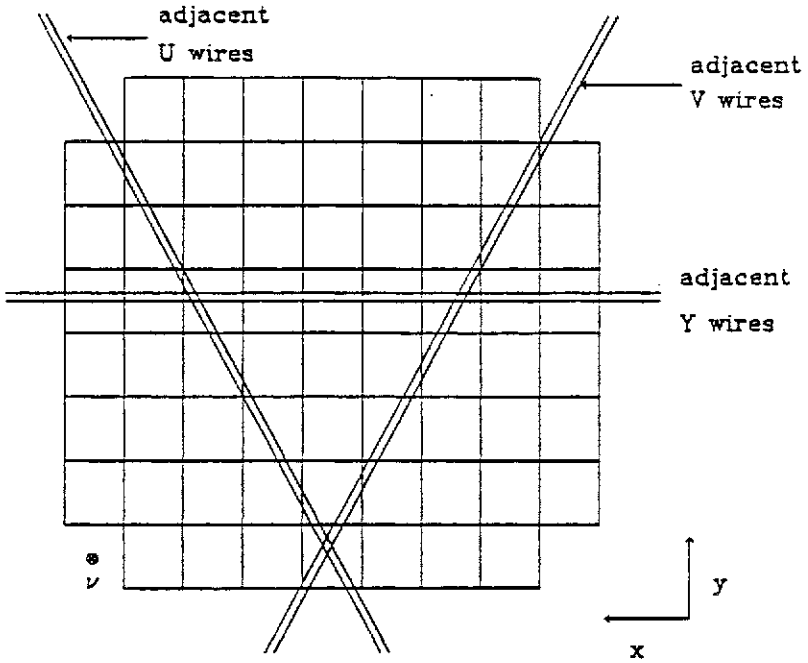

Figure 4.5. EPIC Wire Separations

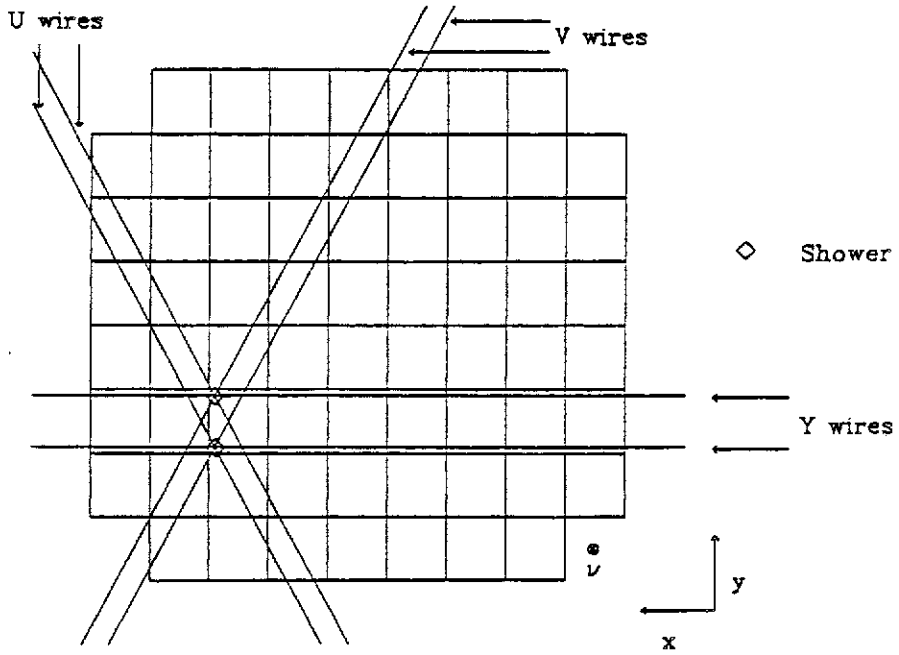

Figure 4.6. Two Spatially Separated Showers

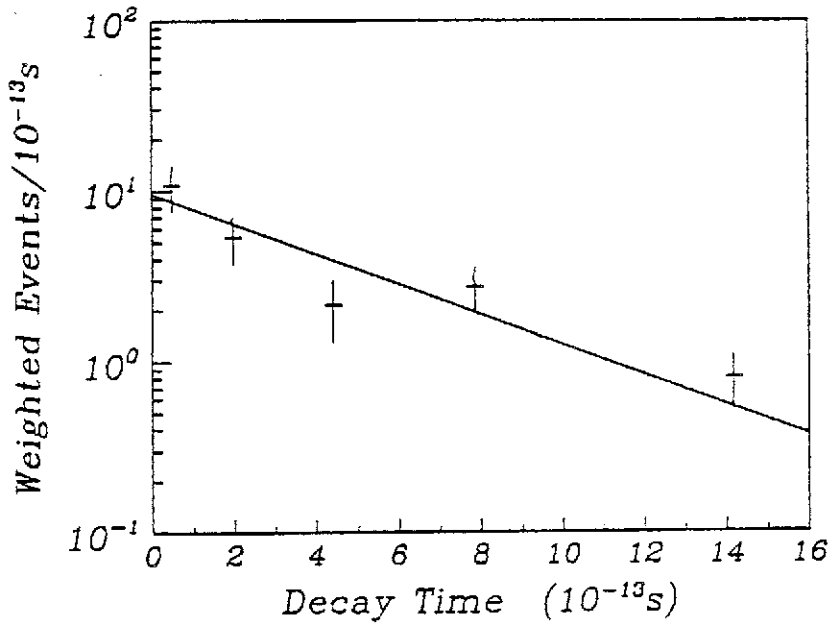

Figure 4.7a. Decay Rate *vs.* Time

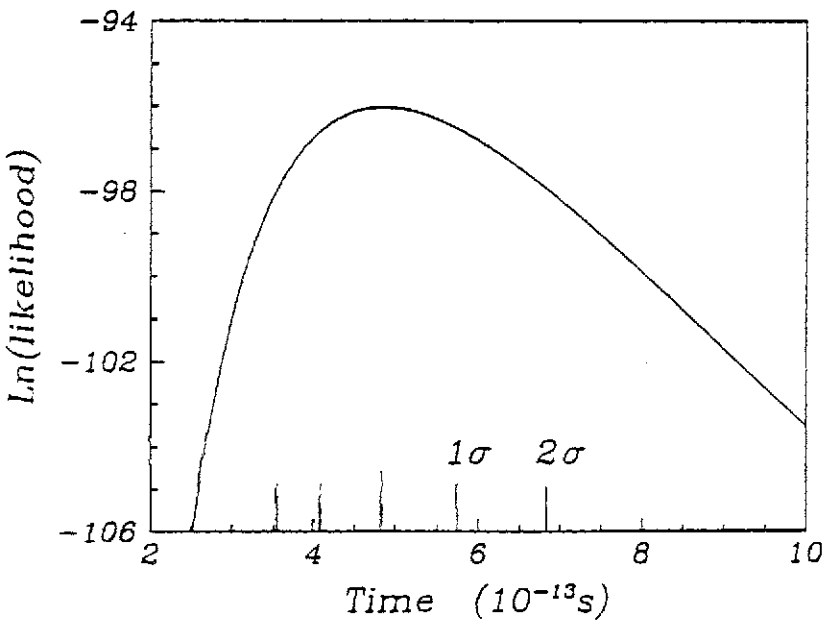

Figure 4.7b. Maximum Likelihood *vs.* Mean Decay Time

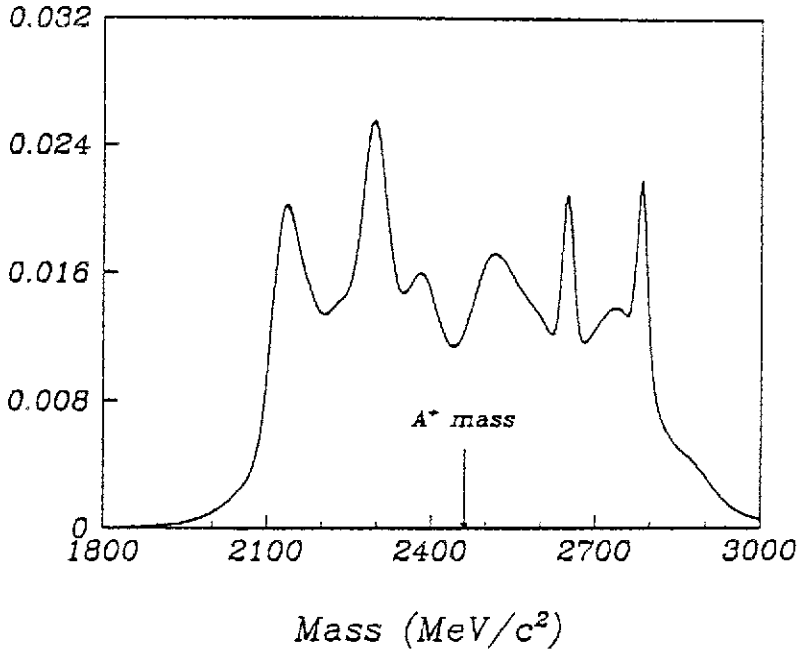

Figure 4.8. Baryon Mass Ideogram

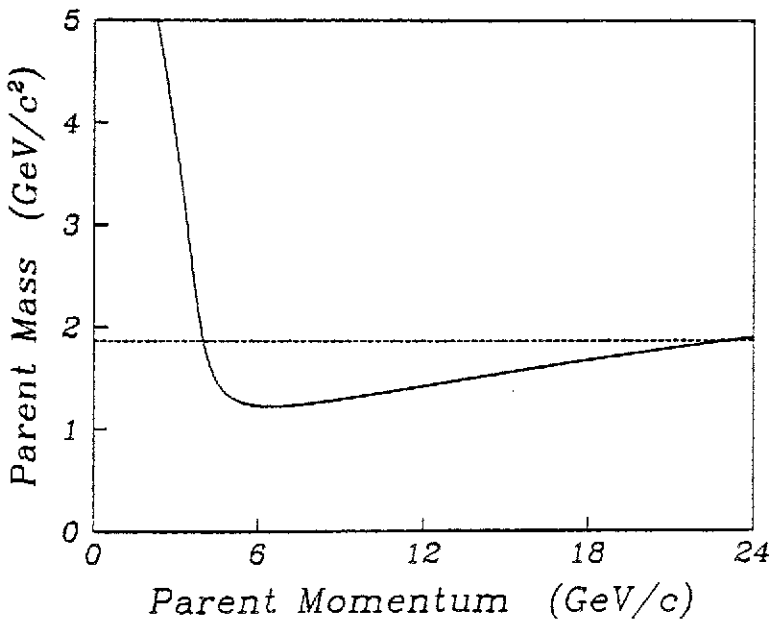

Figure 4.9. A 0–C Solution

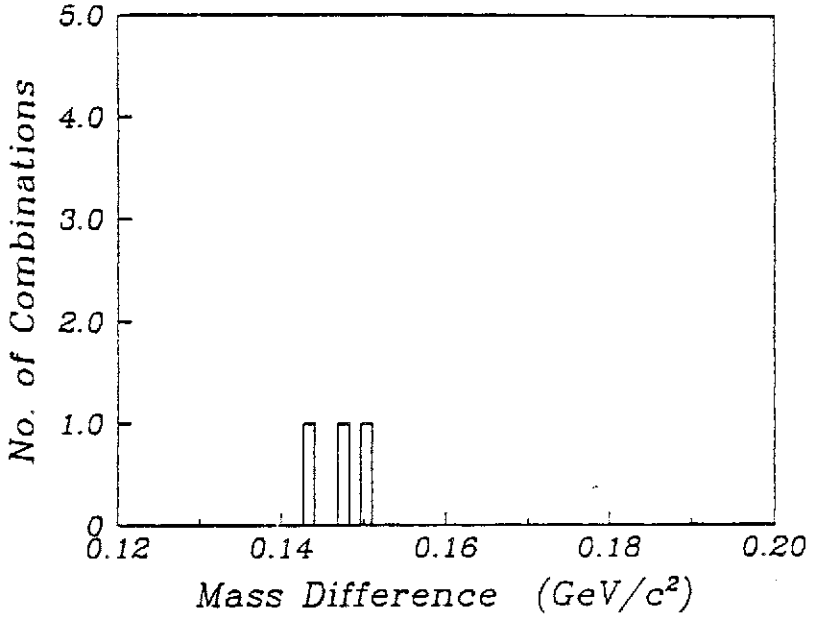

Figure 4.10a. $D^0\pi^+, D^0$ Mass Difference

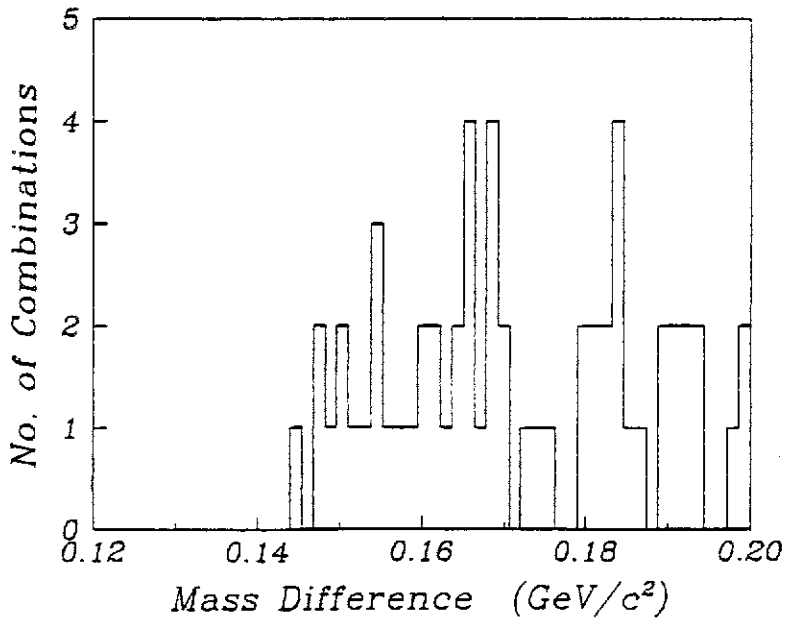

Figure 4.10b. $D^0\pi^+, D^0$ – Mixed Events

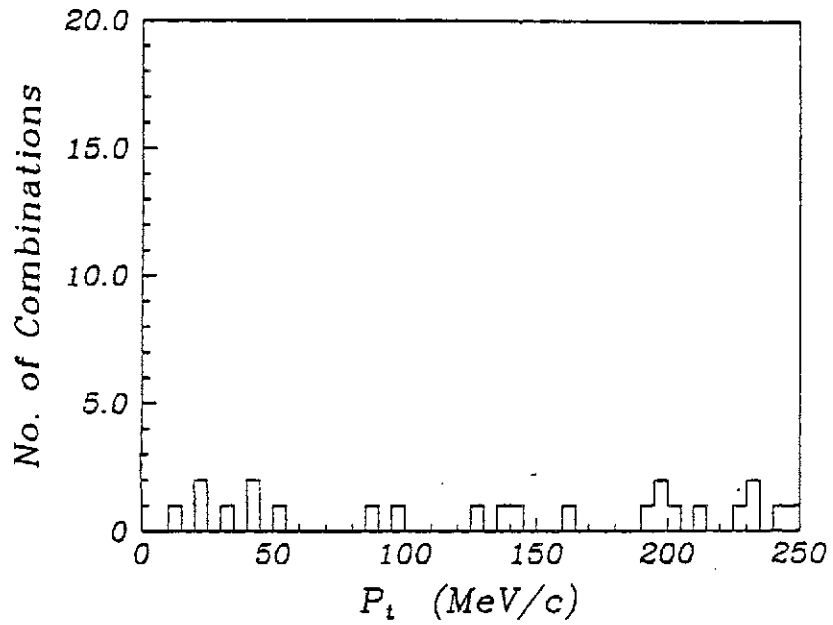

Figure 4.10c. P_t of π^+ relative to D^0

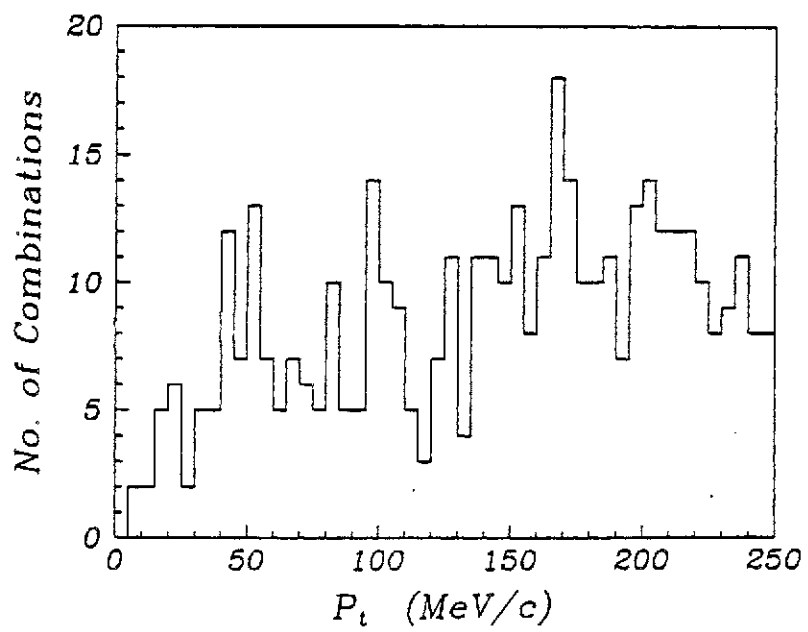

Figure 4.10d. P_t Distribution of Mixed Events

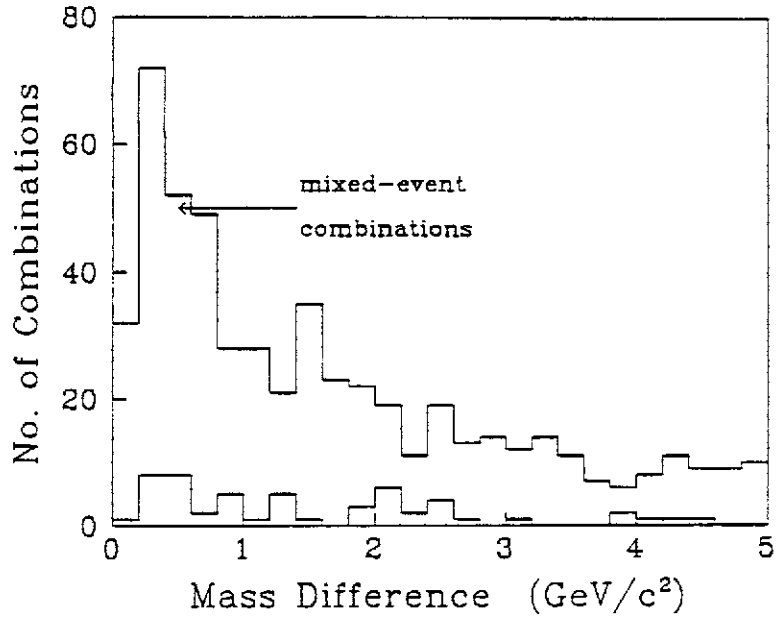

Figure 4.11a. $D^0\gamma, D^0$ Mass Difference

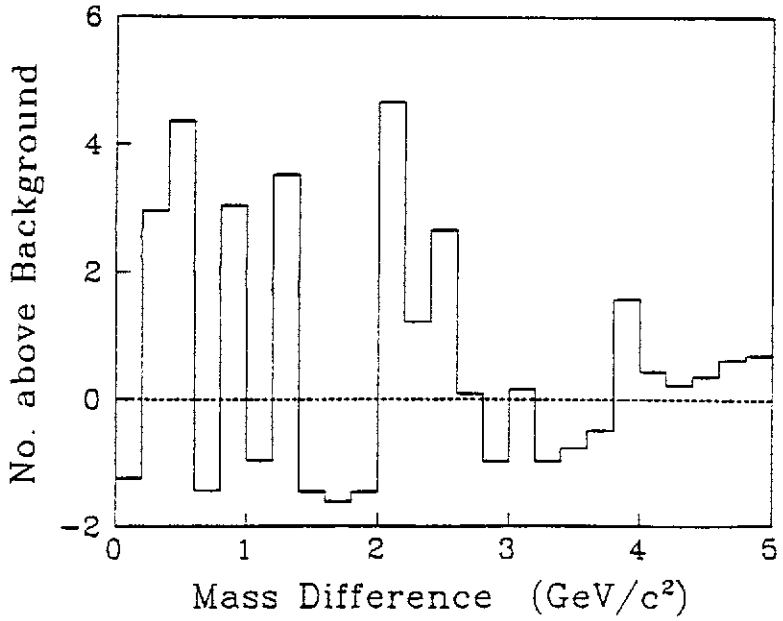

Figure 4.11b. $D^0\gamma, D^0$ less Background

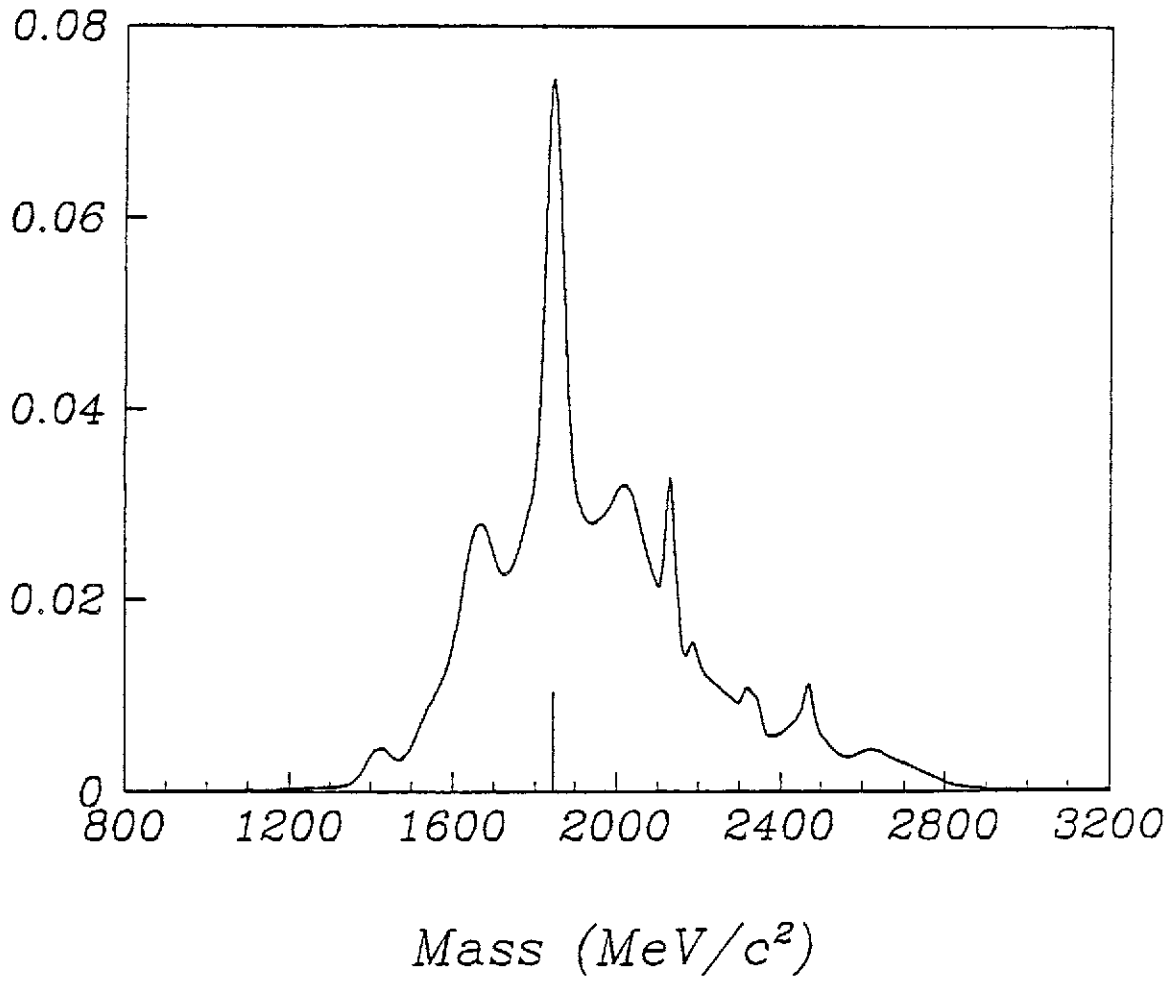

Figure 4.12. D^0 Mass Ideogram

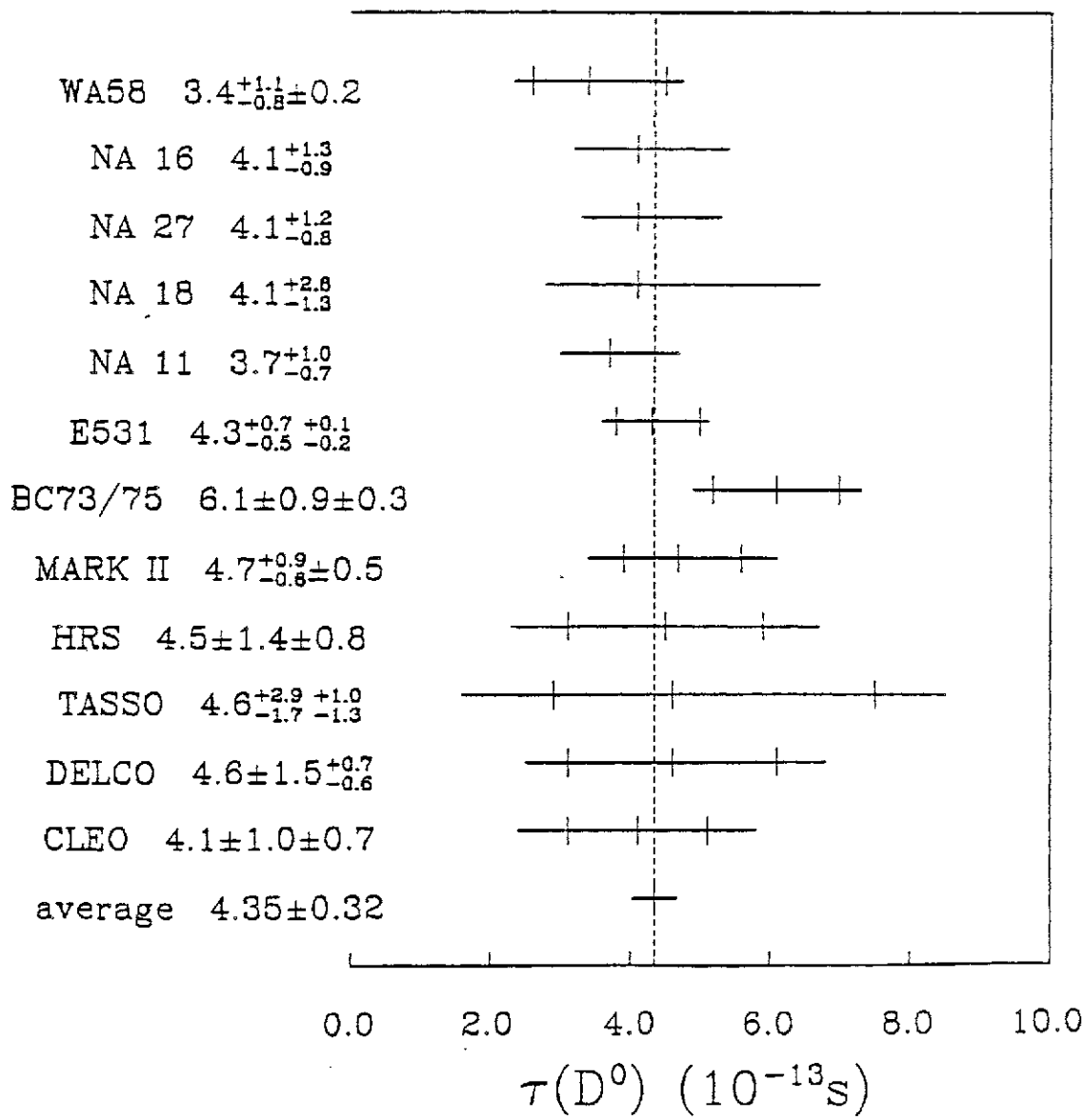

Figure 4.13. D^0 Lifetimes of Other Experiments

Appendix I

N. Ushida

Aichi University of Education, Japan

T. Kondo

Fermi National Accelerator Laboratory, USA

S. Tasaka

Gifu University, Japan

I. G. Park and J. S. Song

Gyeongsang University, Korea

T. Hara, Y. Homma and Y. Tsuzuki

College of Liberal Arts, Kobe University, Japan

G. Fujioka, H. Fukushima, Y. Takahashi, S. Tatsumi and C. Yokoyama

Department of Physics, Kobe University, Japan

K. Fujiwara and K. Taruma

Graduate School of Science and Technology, Kobe University, Japan

S. Y. Bahk, C. O. Kim and J. N. Park

Korea University, Korea

D. C. Bailey, S. Conetti, P. Mercure, J. Trischuk and M. Turcotte

McGill University, Canada

S. Aoki, K. Chiba, H. Fuchi, K. Hoshino, K. Kodama, R. Matsui, M. Miyanishi, M. Nakamura, K. Nakazawa, K. Niu, K. Niwa, M. Ohashi, H. Sasaki, Y. Tomita, N. Torii, O. Yamakawa and Y. Yanagisawa
Nagoya University, Japan

G. J. Aubrecht II, J. Dunlea, S. Errede, A. Gauthier, M. J. Gutzwiller, S. Kuramata, G. Oleynik, N. W. Reay, K. Reibel, R. A. Sidwell and N. R. Stanton
The Ohio State University, USA

K. Moriyama and H. Shibata
Okayama University, Japan

O. Kusumoto, Y. Noguchi, T. Okusawa, M. Terenaka and J. Yamato
Osaka City University, Japan

H. Okabe and J. Yokota
Science Education Institute of Osaka Prefecture, Japan

S. G. Frederiksen, C. J. D. Hébert, J. Hébert and B. McLeod
University of Ottawa, Canada

M. Kazuno and H. Shibuya
Toho University, Japan

I. A. Lovatt, J. F. Martin, D. Pitman, J. D. Prentice, B. J. Stacey and T.-S. Yoon
University of Toronto, Canada

Y. Maeda
Yokohama National University, Japan

Appendix 2.

Constrained Decays

	Decay Mode	Proper Time (10^{-13} s)	Momentum (GeV/c)	Length (μm)
1.	$(D^*)K^-\underline{\pi}^+(\pi^0)$	12.63 0.70	10.36 0.17	2106 112
2.	$K^+\pi^-\pi^0$	0.38 0.01	33.11 0.99	120 2
3.	$K^-\underline{\pi}^+\underline{\pi}^+\underline{\pi}^-\pi^0$	.79 0.14	17.00 0.29	2128 10
4.	$(D^*)\underline{\pi}^-\pi^+K^-\pi^+$	7.13 0.31	4.24 .07	486 20
5.	$K^-\pi^+\pi^0\pi^0$	0.60 0.02	13.29 0.26	128 2
6.	$\underline{K}^-\pi^+\underline{\pi}^-\underline{\pi}^+$	11.7 0.4	8.5 0.2	1589 50
7.	$(\overline{D^0})\pi^-\pi^+\pi^-\pi^+$	3.75 0.16	21.55 0.23	1301 55
8.	$\pi^+\pi^-\pi^0$	1.65 0.10	11.40 0.17	303 18
9.	$\underline{\pi}^+\pi^-K^0_L$	1.69 0.12	15.64 0.69	425 24
10.	$K^-\pi^+\pi^0$	10.0 0.5	15.6 0.4	2221 110
11.	$\pi^+K^-\pi^-\pi^+$	1.38 0.08	9.08 0.10	201 12
12.	$\pi^+\pi^+K^-\pi^-$	6.26 0.32	41.72 2.12	4199 5
13.	$\pi^-\pi^+\underline{\pi}^+\pi^-$	3.08 0.17	21.75 0.33	1077 60
14.	$(D^*)K^-\pi^+\pi^0\pi^0$	11.40 0.30	18.90 0.07	3477 100
15.	$\underline{\pi}^-\pi^+\pi^0\pi^0$	1.96 0.06	14.35 0.25	452 15

	Decay Mode	Proper Time (10^{-13} s)	Momentum (GeV/c)	Length (μm)
16.	$K^+\pi^-\pi^0\pi^0$	2.4 0.1	19.5 0.3	760 40
17.	$\underline{K}^-\pi^+\pi^0$	3.53 0.21	23.42 0.49	1332 74
18.	$(D^*)\pi^+\pi^-\pi^+K^-$	1.86 0.13	3.74 0.09	112 8
19.	$\pi^+K^-\underline{\pi}^-\pi^+$	3.72 0.26	4.56 0.03	273 19
20.	$\pi^-\pi^+K_L^0$	0.07 0.01	14.19 0.98	15 2
21.	$K^-\pi^+\underline{\pi}^-\underline{\pi}^+\pi^0$	1.90 0.02	12.38 0.14	378 2
22.	$\pi^+\pi^-K_L^0$	1.06 0.20	61.83 11.43	1058 54
23.	$\underline{\pi}^+\pi^-K^-\underline{\pi}^+$	0.74 0.08	10.9 0.1	129 14
24.	$(D^0,\overline{D^0})\pi^+\pi^-$	6.64 0.56	28.2 2.4	3006 3
25.	$K^+K^-\pi^0$	8.64 0.47	15.15 0.16	2107 112
26.	$K^-\pi^+$	0.44 0.04	22.4 1.3	157 10

Appendix 3.

Unconstrained Decays

	Decay Mode	Proper Time (10^{-13} s)	Momentum (GeV/c)	Length (μm)
1.	$K^-\underline{\mu}^+(\nu_\mu)$	4.1	30.9	2054
		9.0	14.2	2
2.	$K^-\pi^+(\pi^0)$	2.8	15.9	705
		10.8	4.0	20
	$\pi^-\pi^+(K^0)$	2.0	21.7	
		9.9	4.4	
3.	$\underline{\pi}^+K^-(\pi^0)$	0.9	25.4	383.4
		6.8	3.5	0.3
	$\underline{\pi}^+\pi^-(K^0)$	0.4	57.7	
		6.3	3.8	
4.	$K^-\underline{\pi}^-\underline{\pi}^+\underline{\pi}^+(\pi^0)$	3.6	5.83	338
		0.2		15
5.	$K^-\pi^+(\pi^0)$	0.07	30.5	34.0
		0.28	7.5	0.5
	$\pi^-\pi^+(K^0)$	0.03	67.9	
		0.26	8.0	
6.	$(\overline{D}^0)\underline{\pi}^+\underline{\pi}^-(K^0)$	2.07	19.7	654
		14.3	2.84	20
7.	$\underline{\mu}^+K^-(\nu_\mu)$	0.29	5.4	25
		0.50	3.1	2
8.	$\underline{\mu}^+K^-(\nu_\mu)$	1.1	11.7	197
		2.4	5.2	20
9.	$\pi^+K^-(\pi^0)$	1.4	20.5	459
		4.1	7.0	23
	$\pi^+\pi^-(K^0)$	0.8	37.2	
	3.8	7.6		
10.	$K^-\pi^+(\pi^0)$	1.9	14.0	437
		2.5	11.0	28
11.	$K^-\pi^+(\pi^0)$	9.2	6.8	994
		14.1	4.4	5
	$\pi^-\pi^+(K^0)$	3.5	17.9	
		14.3	4.3	

	Decay Mode	Proper Time (10^{-13} s)	Momentum (GeV/c)	Length (μm)
12.	$\pi^-\underline{\pi}^+\pi^-\pi^+(K^0)$	0.3	4.4	18.0
	$K^-\underline{\pi}^+\pi^-\pi^+(\pi^0)$	0.3	3.9	0.5
	$\pi^-\underline{\pi}^+K^-\pi^+(\pi^0)$	0.3	3.8	
13.	$K^-\underline{\pi}^+(\pi^0)$	9.8	8.3	
	$\pi^-\underline{\pi}^+(K^0)$	7.4	11.0	1306
		10.5	7.7	11

References

1. Becquerel, H., C. R. Acad. Sci. (Paris) **122**, 501 (1896).

2. Rutherford, E. and F. Soddy, Phil. Mag. **4**, 370, 569 (1902)

3. Rutherford, E., Phil. Mag. **47**, 109 (1899).

4. Rutherford, E. and E. N. da C. Andrade, Phil. Mag. **27**, 854 (1914).

5. Rutherford, E., Phil. Mag. **49**, 1 (1900).

6. Pais, A., Rev. Mod. Phys. **49**, 925 (1977).

7. Curie, P. and A. Laborde, 1903, C. R. Acad. Sci. (Paris) **136**, 673 (1903).
   Rutherford, E. and H. T. Barnes, Phil. Mag. **1**, 202 (1904).
   Ramsey, W. and F. Soddy, Proc. R. Soc. Lond. **13**, 346 (1904).

8. Lubimov, E. G., E. G. Novikz, V. Z. Nozik, E. F. Tretyakov and
   V. S. Kosik, Phys. Lett. **94B** ,266 (1980).
   Simpson, J. J., Phys. Rev. Lett **54**, 1891 (1985).

9. Christensen, J. H., J. W. Cronin, V. L. Fitch and R. Turlay,
   Phys. Rev. Lett. **13**, 138 (1964).

10. Chadwick, J., Verh. Dtsch. Phys. Ges., **16**, 383 (1914).

11. Ellis, C. D. and W. A. Wooster, Proc. R. Soc. Lond. **A 117**, 109 (1927).

12. Pauli, W., *Collected Scientific Papers* (Interscience, New York),
    Vol. 2, p. 1313 (1964).

13. Glashow, S. L., J. Illiopoulos and L. Maiani, Phys. Rev. **D2**, 1285 (1970).
Weinberg, S., Phys. Rev. Lett., **19**, 1264 (1967).
Salam, A., in *Proc. 8th Nobel Symposium, Stockholm*, (ed. N. Svartholm, Almqvist and Wiksells, Stockholm, 1968) p. 367 (1968) .

14. Gaillard, M. K., B. W. Lee and J. L. Rosner, Rev. Mod. Phys. **47**, 277 (1975).

15. Aubert, J. J. *et al.*, Phys. Rev. Lett. **33**, 1404 (1974).
Augustin, J.-E. *et al.*, Phys. Rev. Lett. **33**, 1406 (1974).

16. Goldhaber, G. *et al.*, Phys. Rev. Lett. **37**, 255 (1976).
Peruzzi, I. *et al.*, Phys. Rev. Lett. **37**, 569 (1976).

17. Bellini, G. *et al.*, Phys. Rep. **83**, 1 (1982) .

18. Angelini, C. *et al.*, Phys. Rev. Lett. **80B**, 428 (1979).
Allasia, D. *et al*, Nucl. Phys. **B176**, 13 (1980), and references 7–11 therein.
Baranov, D. S. *et al.*, Phy. Lett. **26**, 269 (1977).

19. Ushida, N. *et al.*, Phys. Rev. Lett. **45**, 1049 (1980) and **45**, 1053 (1980).
Ushida, N. *et al.*, Phys. Rev. Lett. **47**, 1694 (1981).
Ushida, N. *et al.*, Phys. Rev. Lett. **48**, 844 (1982) and **51**, 2362 (1983).
Ushida, N. *et al.*, Phys. Lett. **121B**, 287 (1983) and **121B**, (1983).
Ushida, N. *et al.*, Nucl. Instrum. Methods Phys. Res., Sect A **224**, 50 (1984).
Bahk, .S. Y., Ph.D. Thesis, Korea University, 1984 (unpiblished).
Bailey, D. C., Ph. D. Thesis, McGill University, 1983 (unpublished).
Errede, S. M., Ph.D. Thesis, The Ohio State University, 1981 (unpublished).

Gutzwiller, M. J., Ph.D. Thesis, The Ohio State University, 1981 (unpublished).
Hara, T., Ph.D. Thesis, Osaka City University, 1982 (unpublished).
Miyanishi, M., Ph.D. Thesis, Nagoya University, 1983 (unpublished).
Pitman, D., Ph.D. Thesis, University of Toronto, 1983 (unpublished).
Shibuya, H., Ph.D. Thesis, Nagoya University, 1982 (unpublished).
Takahashi, Y., Ph.D. Thesis, Kobe University, 1983 (unpublished).

20. Wohl, C. G. *et al.*, Rev. Mod. Phys. **56**, S1 (1984) .

21. Briedenbach, M. *et al.*, Phy. Rev. Lett. **23**, 935 (1969).

22. Rutherford, E., Phil. Mag. **21**, 669 (1911).

23. Gell–Mann, M., Phys. Lett. **8**, 214 (1964).
Zweig, G., CERN TH–401 (1964).

24. Herb, S. W. *et al.*, Phy. Rev. Lett. **39**, 252 (1977).
Innes, W. R. *et al.*, Phy. Rev. Lett. **39**, 1240 (1977).

25. Basilie, M., CERN–EP/83–52 (1983).

26. Greenberg, O. W., Phys. Rev. Lett. **13**, 598 (1964).

27. Williams, H. H., Talk presented at SLAC Summer Institute on Particle Physics, August, 1982.

28. deGroot, J. G. H. *et al.*, in *Proceedings of the IXth International Symposium on Lepton and Photon Interactions at High Energies, Fermilab, Batavia, Illinois, 1979*
edited by T, B. W. Kirk and H. D. I. Abarbanel (Fermilab, Batavia, Illinois, 1979).

29. Rückl, R., Habilitationsschrift submitted to the University of Munich (1983).

30. Maiani, L., in *Proceedings of the XXIst Conference on High Energy Physics*, edited by P. Petiau and M. Porneuf (Les Editions de Physique, Les Ulis, 1982), p. 631.

31. Turcotte, M. G., Ph.D. Thesis, Mcgill University (unpublished).

32. Ushida, N. *et al.*, Phys. Rev. Lett. **56**, 1767 (1986).

33. Kobayashi, M. and T. Maskawa, Prog. Theor. Phys. **49**, 652 (1973).

34. Shrock, R. E., S. B. Treiman and L.–L. Wang, Phy. Rev. Lett. **42**, 1589 (1979).

35. Rosner, J. L., Invited talk at the Workshop on Charm Production and Lifetimes, Bartol Research Foundation, University of Delaware, October 19, 1978.

36. Chanowitz, M. S., Invited Paper at the International Symposium on High Energy Interactions, Nashville, Tennessee, May 1980.

37. Vella, E. *et al.*, Phys. Rev. Lett. **48**, 1515 (1980).

38. Ushida, N. *et al.*, Phys. Rev. Lett. **56**, 1771 (1986).
Ref. 31.

39. Gilman, F. J., and M. B. Wise, Phys. Lett. **83B**, 83 (1979).

40. Biagi, S. F. *et al.*, Phys. Lett. **122B**, 455 (1983) and **150B**, 230 (1985).

41. Ref. 19, 31, 32.

42. Bailey, D. C., Ph. D. Thesis, McGill University, 1983 (unpublished) and references 123, 162–165, 174 therein.

43. Bailey, D. C. Ph.D. Thesis, McGill University, 1983 (unpublished). Ushida, N. *et al.*, Phys. Lett. **121B**, 287 (1983) and **121B**, 292 (1983).

44. Olsen, S., Invited Paper at Orbis Scientiae, Miami, 1980.

45. Bailey, D. C. Ph.D. Thesis, McGill University, 1983 (unpublished).

46. Pitman, D., Ph.D. Thesis, University of Toronto, 1983 (unpublished).

47. Errede, S. M., Ph.D. Thesis, The Ohio State University, 1981 (unpublished).

48. Lovatt, I. A., M.Sc. Thesis, University of Toronto, 1982 (unpublished).

49. Allison, W. W. M. *et al.*, Nucl. Instrum. Methods **119**, 499 (1974).

50. Bodek, A., in *Proceedings of the Calorimeter Workshop* (M. Atac, Fermilab) (1975) p. 229.

51. Ushida, N. *et al.*, Nucl. Instrum. Methods Phys. Res., Sect A **224**, 50 (1984).

52. Trilling, G. H., Phys. Rep. **75**, 57 (1981).

53. Ronne, B., in *Proceedings of the 1964 Easter School for Physicists*, Herceg–Novi, May, 1964, p. 87.

54. Frodesen, A. G., O. Skejggestad and H. Tøfte, *Probability and Statistics in Particle Physics* (Columbia University Press, New York, 1979).

55. Ushida, N. *et al.*, Phys. Rev. Lett. **56**, 1771 (1986).

56. Barish, S. J. *et al.*, Phys. Rev. **D19**. 2521 (1979) .

57. Errede, S. M., Ph.D. Thesis, The Ohio State University, 1981 (unpublished) and Ref. 131–133 therein.

58. Errede, S. M., Ph.D. Thesis, The Ohio State University, 1981 (unpublished) and Ref. 137 therein.

59. Thorndike, E. H., in *Proceedings of the 1985 International Symposium on Lepton and Photon Interactions at High Energies, Kyoto, Aug. 1985* edited by M. Konuma and K. Takahashi, Kyoto, 1986.

60. Wolf, G., DESY 80/85 (1980).

61. Aguilar–Benitez, M. *et al.*, Phys. Lett. **170B**, (1986).

62. Fisk, H. E., and F. Sciulli, Ann. Rev. Nucl. Part. Sci. **32**, 499 (1982).